UNIVERISTY OF CALIFORNIA MERCED

**Perovskite semiconductors: From high performance devices to optical characterization**

A dissertation submitted in partial satisfaction of the
requirements for the degree of
Doctor of Philosophy

in

Physics

by

Som Sarang

Committee in charge:

Professor Jay Sharping, Chair
Professor David Strubbe
Professor Sayantani Ghosh, Graduate advisor

**Perovskite semiconductors: From high performance devices to optical characterization**

The dissertation of Som Sarang, titled Perovskite semiconductors: From high performance devices to optical characterization , is approved, and it is acceptable in quality and form for publication on print and electronically:

_____ Date _____

Prof. Jay Sharping, Chair

_____ Date _____

Prof. David Strubbe

_____ Date _____

Prof. Sayantani Ghosh, Graduate advisor

University of California, Merced

To my parents, Sumi Soman and Somasekharan C G, for always believing in me, even when I didn't believe in myself

To Sagar, my awesome brother, for his constant love and encouragement

# Acknowledgments

First and foremost, I would like to extend my at-most gratitude, love and debt towards my graduate advisor, Professor Sayantani Ghosh. She has been a constant support and inspiration during my 5 years at UC Merced. I cannot imagine a better graduate advisor and this work would not have been possible without her vision, knowledge and expertise. Thank you Sai, for being a great friend and mentor, and for letting me be a member of your lab. It has been the most rewarding part of my research life.

Additionally, I would like to express my sincere appreciation to Prof. Vincent Tung and Prof Jing Zhang, who have collaborated with us on most of my thesis work. Their insights, promptness and scientific inquisitiveness aided many of the research conducted as part of this thesis. Prof. Zhang graciously spent hours with me discussing my experimental results and it was always comforting to know that he is only an email way if I needed any assistance with my research. Discussions with him were very fruitful and has guided me in widening and improving my research project. Vincent, with his expertise in fabrication and electron microscopy, was my go-to person for any perovskite synthesis related issues. He spent many late night hours at LBNL taking awesome microscopy images for us to use in our publications, for which I'll be forever thankful to him. Vincent's impressive photoshop skills helped us submit cover illustrations with our research articles, this aided in promoting our research and reaching a wider scientific audience.

I express my gratitude towards Prof. Ajay Gopinathan and Prof. Michael Sheibner, for guiding me on various occasions. Ajay has also been a good friend outside research and was a great help when I was still adjusting to Merced, having moved all the way from my homecountry, India.

Much of the work described in my thesis, was made possible only due to the perseverance, hard work and efforts of postdoctoral researchers and graduate students from the Ghosh lab, Tung lab, Scheibner Lab and Zhang lab. The establishment of the nanomaterials and energy research center, MACES, at UCM, led to a successful collaboration between these groups, bringing in experience, insights and knowledge from different research fields. I'm grateful to be an initial graduate member of MACES. MACES provided me the opportunity to work alonside graduate students, Sara, Yen Chen, Oliver and Wenjun, and postdocs, Binbin and Parveen, all of whom have shared authorship with me on my research publications. They have all invested their time and effort into the successful completion of my research. Thank you guys!

I'm also grateful to the faculty and other members of the Physics department at UC Merced. They all played their part in making UC Merced a proactive research

environment and it was motivating and encouraging to be part of such a skilled and intelligent cohort. Credit must go my labmates, Kat, Mark, Chris, Jussi, Makiko, Boe and Will. It was a pleasure working alongside them for 5 years. I will always cherish the memories of working at Ghosh lab. None of this would have been possible without their assistance and camaraderie.

I would like to thank my family and friends especially my mom and dad (Sumi and Somasekharan), and my brother, Sagar, for their unconditional love and support. They were always the driving force that encouraged me to follow my dreams and pursue my passion for physics. Love and appreciation also goes to my Merced family - Amanda, Kat, Eric, John, and Alex. You guys made Merced a home for me for the last 5 years. My sincerest appreciation to Merced Indian association, my friends - Ameed, Vishal, Milind, Himanshu, Rafay and my cricket group. You never made me feel away from India. I will always treasure our parties and celebrations.
Without doubt, my biggest strength and support over the last 5 years has been my girlfriend, Nivin. It was her patience, care and affection, that made me overcome my failures and encouraged me to strive for excellence.

I would also like to acknowledge my thesis committee, Prof. Jay Sharping, Prof. David Strubbe and Prof. Sayantani Ghosh for their constructive feedbacks during our annual review meetings and further, for help in editing this dissertation.
Last, but not the least, I would like to acknowledge my funding sources, NSF, NASA, UCM, Dan David foundation and SNRI, for their financial assistance towards the completion of my PhD.

# Contents

# List of Figures

# List of Tables

# Curriculum Vitae

## Som Sarang

LinkedIn : www.linkedin.com/in/somsarang90
Website : https://sarangsom.wixsite.com/ssarang
Email : somsarang90@gmail.com
Phone: +1 914-765-9274

### CONTACT INFORMATION

1347 Jenner Drive, Merced
California 95348 USA

### CURRENT POSITION

Graduate researcher, *School of Physics*
**University of California Merced**

### RESEARCH INTERESTS

Semiconductors, Optics, LEDs, Photovoltaics, Nanotechnology, Microscopy, Quantum dots, Ultrafast spectroscopy, Ti:Saphire Lasers, Functional 2D Materials, Energy materials, Electronics, Plasmonics

### EDUCATION

**University of California Merced** **2014-2019**
*Ph.D in Physics* (GPA 3.96/4)
Thesis : "Perovskite semiconductors: From high performance devices to optical characterization"
Advisor : Prof. Sayantani Ghosh

**Indian Institute of Science Education and Research Thiruvananthapuram** **2009-2014**
*MS in Physics* (GPA 9/10)
Minor in Mathematics
Thesis : "Metal oxide- graphene composites as anodes in Lithium batteries"

Advisor : Prof. M. M. Shaijumon

**Indian Institute of Science Education and Research Thiruvananthapuram** **2009-2014**
*BS in Physics* (GPA 9/10)
Minor in Mathematics

## PUBLICATIONS

"Nanostructured Photovoltaics", **Som Sarang**, Katerina Nikolaidou, Sayantani Ghosh. *Nano. Futures*, 3, 012002, (2019)

"Exploring morphology and composition to maximize efficiency of hybrid perovskite luminescent solar concentrators", Benaz Mendewala, Katerina Nikolaidou, **Som Sarang**, Christine Hoffman, Vincent Tung, Boaz Ilan and Sayantani Ghosh. *Solar. Energy*, 183, 392-397, 2019

"Tuning excitonic properties of pure and mixed halide perovskite thin films via interfacial engineering", Katerina Nikolaidou, **Som Sarang**, Denzal Martin, Vincent Tung, Jennifer Q. Lu, and Sayantani Ghosh. *Adv. Mater. Interfaces*, 1800209 (2018)

"Plasmon-actuated nano-assembled microshells", Makiko T. Quint, **Som Sarang**, David A. Quint, Anand B. Subramaniam, Kerwyn Casey Huang, Ajay Gopinathan, Linda. S. Hirst, and Sayantani Ghosh. *Scientific Reports*, 7:17788 (2017)

"Stabilization of Cubic Crystalline Phase in Organo-metal Halide Perovskite Quantum Dots via Surface Energy Manipulation", **Som Sarang**, Sara Bonabi, Binbin Luo, Parveen Kumar, Edwin Betady, Vincent Tung, Michael Scheibner, Jin Z. Zhang, and Sayantani Ghosh. *J. Phys. Chem. Lett* , 8, 5378-5384 (2017)

"Low temperature photoluminescence as a probe of exciton energy and dynamics in hybrid perovskite thin films", **Som Sarang**, Ishihara Hidetaka, Yen-Chang Chen, Oliver Lin, Ajay Gopinathan, Vincent C. Tung, and Sayantani Ghosh. *Phys. Chem. Chem. Phys.*, 18, 28428-28433 (2016), 1. DOI: 10.1039/C6CP02971J

"Photovoltaic and optical properties of perovskite thin films fabricated using Marangoni flow assisted electrospraying", **Som Sarang**, Hidetaka Ishihara, Yen-Chang Chen, Oliver Lin, Vincent Tung, Sayantani Ghosh. *Proc. SPIE 9745, Organic Photonic Materials and Devices XVIII,* 9745, 974519 (2016).

"Nature Inspiring processing route toward high throughput production of perovskite photovoltaics", Hidetaka Ishihara*, **Som Sarang***, Yen-Chang Chen, Oliver Lin, Pisrut Phummirat, Lai Thung, Jose Hernandez, Sayantani Ghosh and Vincent Tung. *J. Mater. Chem. A,* 4, 6989 (2016)

"Hybrid perovskite thin films as highly efficient luminescent solar concentrators", Katerina Nikolaidou, **Som Sarang**, Christine Hoffman, Benaz Mendewala, Hidetaka Ishihara, Jennifer Q. Lu, Boaz Ilan, Vincent Tung, and Sayantani Ghosh. *Adv. Opt. Mater.*, 4, 2126-2132 (2016) DOI: 10.1002/adom.201600634

"Continuous Liquid Interface Propagation of Perovskite Photovoltaics", Hidetaka Ishihara, Wenjun Chen, Yen-Chang Chen, **Som Sarang**, Nicholas De Marco, Oliver Lin, Daniel Sun, Wendy L. Queen, Sayantani Ghosh and Vincent C. Tung. *Adv. Mater. Interfaces,* 3, 15300762 (2016) 3:doi:10.1002/admi.201500762, *(cover article)*

"$Nb_2O_5$/Graphene nanocomposites for electrochemical energy storage", P. Arunkumar, A.G. Ashish, B. Babu, **Som Sarang**, Abhin Suresh, Chithra Sharma, M. Thalakulam and M. M. Shaijumon. *RSC Advances,* 5, 59997, (2015)

"$TiNb_2O_7$/Graphene hybrid material as anode for Li-ion batteries", A.G. Ashish, P. Arunkumar, B. Babu, P. Manikandan, **Som Sarang** and M. M. Shaijumon. *Electrochemical Acta,* 176, 285-292 (2015)

## SELECTED RESEARCH EXPERIENCE

**University of California Merced** **2014-present**
*Graduate Researcher*

**Indian Institute of Science Education and Research** **2012-2014**
*Graduate Researcher*

**Indian Institute of Science** **2012**
*Graduate Intern*

**Institute of Mathematical Sciences** **2011**
*Graduate Intern*

## SELECTED FELLOWSHIPS AND AWARDS

Dean's Distinguished Scholar Fellowship, *UC Merced*, 2018

MACES fellowship, *NASA*, USA, 2015-2017

Dan David Solar fellowship, *UC Merced*, 2016 2017

Southern California Edison fellowship, *SNRI*, USA, 2017

Outstanding graduate researcher in Physics, *UC Merced*, USA, 2015 2017

UC Merced Physics travel grant, *UC Merced*, USA, 2015-2018

Outstanding performance in graduate Physics exam, *UC Merced*, USA, 2014

CSIR-NET (Physics) All India Rank 7, *DST*, India, 2014

Summer research fellowship, *IMSc*, India, 2012

Indian Academy of Sciences summer fellowship, *IAS*, India, 2011

INSPIRE Fellowship, *Department of Science and Technology*, India, 2009-2014

## TECHNICAL SKILLS

**Experimental techniques :** Ultrafast spectroscopy, Time-resolved spectroscopy, Ti:Saph lasers, Laser physics, **Single photon counting techniques**, Geometric optics, **Confocal microscopy, SEM, TEM, AFM**, Raman spectroscopy, quantum optics, **Spin polarization spectroscopy (MOKE, Hanle)**

**Fabrication :** Solid state synthesis, **Electrospraying, Photolithography**, Spin coating, Hydrothermal synthesis, **CVD, PECVD**, Thermal evaporation, Sputtering

**Computation : Matlab, Python**, Fortran, FDTD, **Labview**, latex, MS - office

**Additional skills :** XRD, Li ion battery testing, cyclic voltametry, Supercapacitor testing, Cryogenics, Ultrahigh vacuum

## SELECTED TALKS

"Stabilization of Cubic Crystalline Phase in Organo-metal Halide Perovskite Quantum Dots via Surface Energy Manipulation" MRS Fall meeting, Boston, Massachusetts, 2018

"Stabilization of Cubic Crystalline Phase in Organo-metal Halide Perovskite Quantum Dots via Surface Energy Manipulation"APS March meeting, Los Angeles, California, 2018

"Low temperature Perovskite opto-electronic characterization" APS Far-west meeting, Merced, California, 2017

"Electro-hydrodynamic spray synthesis and low temperature spectroscopic characterization of Perovskite thin films" APS March meeting, New Orleans, Louisiana, 2017

"Elucidating Fast Recombination in Low Temperature Phase of $CH_3NH_3PbI_{3-x}Cl_x$ Perovskite Thin Films Synthesized Using Continuous Liquid Interface Propagation "MRS March meeting, Phoenix, Arizona, 2016

"Photovoltaic and optical properties of perovskite thin films fabricated using Marangoni flow assisted electrospraying" SPIE Photonics West, San Francisco, 2016

"Photovoltaic and optical properties of perovskite thin films fabricated using Marangoni flow assisted electrospraying"NANOS 2015, Gitam University, India

## POSTERS PRESENTED

Indo - US workshop on engineered electrodes for electrochemical energy storage, India

MACES open house, UC Merced, Merced

NanoBio Workshop, UC Boulder, Colorado

NanoBio hands-on Workshop, UIUC, Illinoi

UIUC NanBio NSF Fund review, UIUC, Illinoi

## PROFESSIONAL ASSOCIATION

| | |
|---|---|
| Member, American Physical Society | 2014-present |
| Member, Materials Research Society | 2015-present |
| Member, SPIE Photonics | 2015-2016 |

## OUTREACH

Allan Peterson elementary school 2015
Merced college 2016
*As part of MACES outreach initiative*

Golden Valley High school 2017
El Capitan high School 2017
Buhach Colony high school 2016, 2018
*Developed experiments and curriculum for promotomoting STEM in the central valley, CA*

## Abstract

Perovskite semiconductors: From high performance devices to optical characterization

by

Som Sarang

Doctor of Philosophy in Physics

University of California, Merced

Professor, Sayantani Ghosh, Graduate Advisor

In just over a decade, perovskite semiconductors have shown immense promise as candidates for next generation opto-electronic technologies, attributed to broad absorption spectra, long recombination lifetimes, ambipolar charge carrier conductivity and impressive electron mobility. Perovskite photovoltaics(PV) with power conversion efficiencies $\geq 23$ %, is challenging existing solar cell technologies and have revolutionized the field of solution processed solar cells. However, several drawbacks arising from perovskite stability and scalability have prevented them from achieving their full potential. The scope of this dissertation is to address some of these concerns, while also shedding light into the atypical physical properties of Perovskite semiconductors. The first part of the thesis deals with developing a rapid thoroughput and scalable fabrication route for perovskite thin film solar cells, utilizing an electro-hydrodynamic spraying route inspired from 'Marangoni flow' seen in nature. The fabricated perovskite solar cells had superior current-voltage characteristics and displayed an efficiency of $\geq 16$ %, which at the time (2015) was one of the highest reported power conversion efficiencies. Additionally, the developed fabrication method requires lower amounts of precursor solvents compared to other scalable approaches, thus reducing Lead wastage and mitigating environmental issues often associated with perovskite solar cells.

Following this project, a range of low temperature, ultrafast optical spectroscopy techniques were used to probe the partial phase transitions in Perovskite thin films. This revealed charge migration pathways in perovskite thin films at low temperatures that prove detrimental for their device performance. In parallel, our experiments showed that the phase transition is associated with a crossover from excitonic to free charge carrier recombination in perovskite thin films. The above results encouraged us to investigate nanocrystals of perovskite semiconductors, aiming to achieve better crystal phase stability at low temperatures. We successfully quenched partial

crystal phase transitions at low temperatures in perovskite quantum dots utilizing ligand based surface modification techniques. These findings highlighted aspects of perovskite phase stability linked to nanoscale morphology, paving way for improved perovskite devices operating at low temperatures.

Lastly, the potential of perovskite quantum dots in spintronics applications were explored. We demonstrated optical spin polarization in perovskite quantum dots and measured their spin lifetimes using Hanle effect. In addition, Manganese ion dopants in Ruddlesden-Popper perovskite quantum dots exhibited polarized photoluminescence emission attributed to strong exchange interactions

In conclusion, we successfully developed high performing perovskite PV devices and demonstrated their plausible application in other opto-electronic technologies, while also shedding light into its interesting physical properties.

# Chapter 1

# Motivation and overview

Climate change along with over dependence on non renewable sources are the most pressing issues of the $21^{st}$ century. Oil consumption rates are at all time high and have exceeded their production rates by times four. It is of paramount importance to develop alternative fuels for sustainability and drive the society away from their dependence on non-renewable sources of energy. For this very purpose, we have seen an increase in the development of renewable sources, including solar, biomass, wind, tidal and hydroelectric sources.

Out of the total energy produced in the US, only 11% comes from renewable sources, out of which only 6% of the 11% comes from solar energy. However, that is a substantial increase from the 1% in 2010, signifying recent advancements in solar energy technologies. Solar energy is readily available freely in all parts of the world and solar cells or photovoltaic (PV) systems do not produce environmentally toxic byproducts, making them more sustainable and viable alternatives in the long run.

In order to match the present day energy requirements and reach grid parity (the cost of solar electricity equaling the cost of conventionally-generated electricity), a substantial amount of research is carried out on the development of next generation solar cells. This has resulted in the development of several solar technologies, ranging from the low-cost low-efficiency (2-5%) devices (ex. organics), to mid-cost mid-efficiency (10-20%) devices (ex. silicon), and finally to the high-cost high-efficiency (30-40%) devices (III-V semiconductor materials). But the existing technologies suffer from either low efficiency, high cost or extreme fabrication requirements not available in developing countries. For solar technologies to reach third world nations where the need for such systems are the most prevalent, it is necessary for solar cells to be cheap, easy to fabricate and have high efficiencies.

The chart describing the power conversion efficiencies (PCE) of various solar

cells is released by National Renewable Energy Labs (NREL) every year -`https://www.nrel.gov/pv/cell-efficiency.html`. Among the newer technologies, single junction perovskite solar cells have shown remarkable growth in the last decade. Graph displaying improvement in average efficiencies of different types of perovskite solar cells over the last few years is shown in figure 1.1

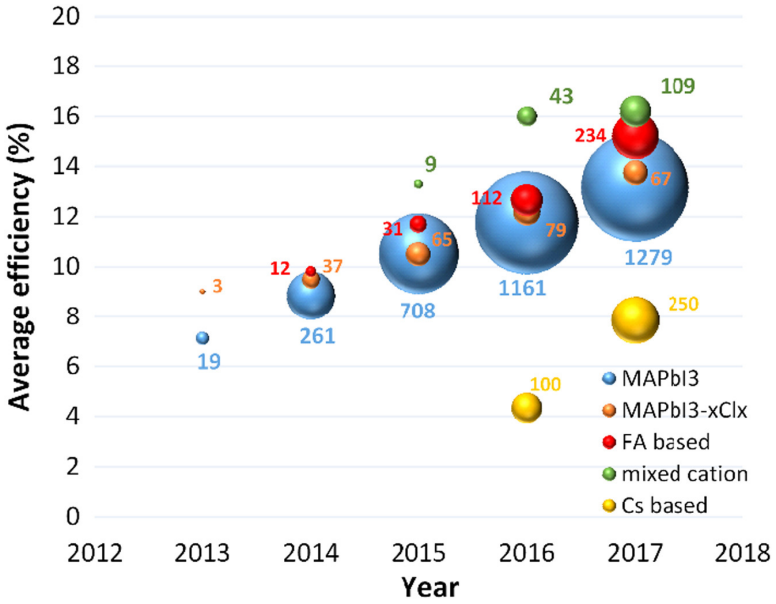


Figure 1.1: Average efficiencies of different cation dependent perovskite solar cells over the years[reproduced from ref[1]]

Perovskite solar cells are solution processed thin film devices that work similar to a polymer solar cell. It was initially believed to resemble a dye sensitized solar cell (DSSC). However in 2009, Snaith's group at university at Oxford demonstrated the charge transport properties of a stand alone perovskite thin film device, pioneering the field of thin film perovskite photovoltaics.
Their efficiencies have quite remarkably gone from 3.8% to 23.3% in the span of 10 years (2009-2019). This is a very steep increase compared to other technologies and outperform a number of existing PV technologies, for example DSSC, which has remained at $\leq$ 12% PCE even after 30 years of active research. Unfortunately, Perovskite solar cells are not without drawbacks, they suffer from low stability, high lead (Pb) content and lack of scalable synthesis methods. Hence, current research on perovskite solar cells is predominantly focused on improving its stability, reducing or replacing Pb and shedding light on their unusual physical properties. In this work we

have tried to address some of the above mentioned topics.

We discuss the development of a new facile, rapid fabrication route for perovskite thin films in chapter 3. It makes use of an electrohydrodynamic spraying technique to fabricate a perovskite solar cell with efficiency $\sim 16\%$. At the time of this work, this was one of the highest reported values, but since then efficiencies have exceeded $\sim 20\%$. The technique is easily scalable and versatile, as it can use two different spraying sources instead of one, thus eliminating the need to find a common solvent for perovskite precursors. It also further drastically reduces the amount of lead needed for fabrication.

In chapter 4, tools such as low temperature static and dynamic photoluminescence were employed to elucidate on the physical properties of perovskite thin films. It is revealed that Perovskite thin films undergo partial phase transitions (co-existence of two phases) at low temperatures, leading to a reduction in performance. A change in the charge carrier type is also observed at temperatures below $\sim 140$ K, which along with charge carrier migration between phases prove to be detrimental to device performance.

Following this result, we developed ligand based surface modification techniques to prevent partial transitions in perovskite quantum dots. By modifying the surface energy of the quantum dots, the high temperature cubic crystalline phase was stabilized at low temperatures. This result could pave way to the development high efficiency perovskite solar cells at low temperatures. Our results were verified using various low temperature spectroscopy techniques.

Finally, in chapter 6, we explored the potential of perovskite semiconductors in spintronic applications. Optical spin polarization of charge carriers was observed in perovskite quantum dots. Furthermore, Hanle effect was used to measure the spin dephasing lifetimes of these charge carriers at low temperatures. By exploiting the spin polarized excitons, we were to realize polarized emission from Manganese 2+ ions dopants in perovskite quantum dots.

Perovskite technologies have already reached astonishing heights, yet there are several limitations in its understanding and implementation. Through the research described here, we hope to contribute to its further development and throw light on its fascinating and peculiar physics.

# Chapter 2

# Review of perovskite semiconductors: Synthesis, opto-electronic properties and limitations

## 2.1 Perovskite thin films

Perovskite solar cells (PSCs) have led to the most promising advancements in photovoltaic technologies in the last decade[2–5]. Their power conversion efficiencies have surpassed 23 % and have shown a steady increase from the 9% reported in 2009, making them among the fastest growing opto-electronic technologies[6, 7]. Such remarkable high performance is attributed to its ideal band gap, long charge carrier diffusion lengths[8], excellent electron hole mobility[9], defect tolerance and high absorption coefficients[10]. Additionally, PSCs are fabricated using solution processing techniques such as spin coating, doctor blading[11, 12], spray coating[13] etc. making them optimal for large scale production at a rapid scale. These qualities make them ideal for high performance, low cost PV technology.

### Brief history

The pioneering paper on PSCs was published from Prof. Miyasaka's group at Toin university in the year 2009 and since have been cited over 6000 times[7]. The name perovskite refers to a particular crystal structure, predominantly $ABX_3$ (figure 2.1 where A refers to monovalent cation ($Cs^+$, Methyammonium$^+$), B refers to a bivalent anion ($Pb^{2+}$, $Sn^{2+}$) and X is an anion, generally halide ($Cl^-$, $Br^-$, $I^-$) or acetate.

They exist in cubic, tetragonal, orthorhombic and some mixed crystalline phases. In an typical cubic crystal structure, the B cation and A anion are surrounded by an octahedron and cuboctahedron of ions, respectively, resulting in a 6-fold and 12-fold coordination symmetry. The crystal structure of a typical perovskite is shown in figure 2.1.

History of perovskite dates back to the $19^{th}$ century, discovered by the Prussian, Gustav Rose in 1839 and named perovskite, after the renowned minerologist Count Lev A. Perovskiy. Later, a series of oxides with similar structure were discovered and were commonly classified as perovskite compounds.[4]

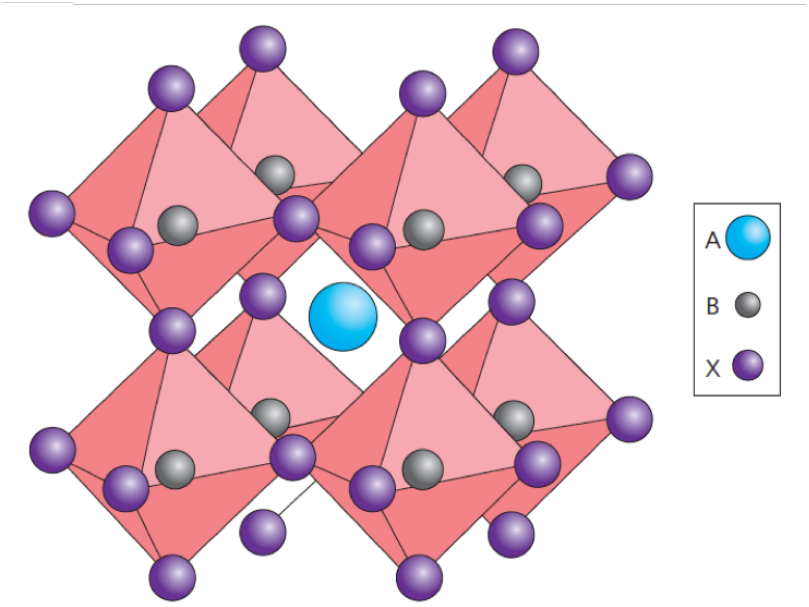


Figure 2.1: Crystal structure showing cubic phase of perovskite [reproduced with permission from ref[7] ©(2009) American Chemical Society]

These oxides showed promise as potential materials for ferroelectric, piezoelectric and pyroelectric applications. They however had inferior semiconducting properties making them unsuitable optoelectronic or photovoltiac activity. On the other hand, a new class of perovskite materials in which the oxides were replaced by halide ions showed reasonable performance in semiconductor devices. Since the early $19^{th}$ century these materials were studied extensively for multiple applications, yet, it wasn't until 2005 that they were tested as active layers in solar cells.

Due to extreme temperature requirements for fabrication of second generation silicon solar cells a lot of research and effort were put into the advancement of new solar technologies. One such breakthrough was the development of dye sensitized solar cells (DSSCs) that were relatively cheaper, solution processed and environmentally compatible. But even after two decades of research the power conversion efficiencies (PCE) of the devices still are relatively low compared to commercially available Si. The highest reported efficiencies did not exceed 12% and subsequently scientists started delving into possible alternatives for the organic dye present in the DSSC. In 2009, the Miyasaka group used a halide based perovskite material as the light absorber instead of the conventional organic dye, paving way to the next generation of PSCs.[7]

The first perovskite PV employed $CH_3NH_3PbX_3$ (X=I, Br) as the light absorbing layer in a $TiO_2$ mesoporous system with a lithium halide electrolyte[7]. It showed a PCE of 3.8%, which albeit low is very high for a new PV system. Further evidence of perovskite standalone solar cells came from testing perovskite sensitizers in an insulating $Al_2O_3$ scaffold that should have a lower performance compared to a $TiO_2$ mesoporous system. But the device showed improved performance with a PCE of 10.9%.[14] providing evidence that perovskite also have excellent charge carrier transport properties. This was a major breakthrough pioneering the field of standalone perovskite thin film solar cell research. The first half of the last decade, scientists' focused on the development of higher efficiency PSCs, while since 2017, the focus has shifted towards improved PSC stability and longevity using encapsulation and chemical modification techniques.

## 2.2 Properties of perovskite semiconductors

Advancement in computational power in parallel with theoretical modelling techniques have helped scientists get a comprehensive understanding of perovskite crystals' semiconducting properties[4]. Perovskite semiconductors are ionic in nature and their properties vary widely depending on their chemical constituents. For example, the band gap can be tuned depending on the halide present in the materials. Bromide based perovskite have the largest bandgap (2.2–2.3eV), while Iodide ones have the shortest (1.7–1.8eV)[10]. Their crystalline phases are also widely dependent on temperature and the chemical structure. In order to further elucidate on the exceptional optical properties of perovskite semiconductors different research groups have employed first-principle calculations using density functional theory (DFT). The results sometimes varies depending on the type of exchange-correlation functionals used in the simulations. Some of the important properties of perovskite semiconductors that gives rise to its unique opto-electronic properties are described below:

## Crystal structure

As described earlier, the common crystal structure of perovskites is $ABX_3$ shown in figure 2.2 a. The crystal stability of perovskite structure can be quantified using the tolerance factor t given by:

$$t = \frac{R_A + R_X}{\sqrt{2}R_B + R_X} \tag{2.1}$$

where $R_A$ $R_B$ and $R_X$ are the ionic radius of A, B and X respectively. A high cubic symmetry implies a value of t close to 1. Since B is mostly Pb or Sn and X being a halide, t$\sim$1 requires A to be a very large molecule, that is tough to be satisfied using an inorganic cation. Hence, most commonly studied perovskites have an organic cation such as methylammonium (MA) [14–16]or formamidinium (FA)[17, 18] at the A site, while some have also fabricated perovskite crystals with Cs cation[19, 20] even though it leads to a highly strained crystal structure. Recently in 2016, Snaith's group from University of Oxford and Gretzel's group at EPFL, simultaneously demonstrated that it is possible to have a mixed cation systems with superior stability and PV characteristics compared to pure cation based perovskite devices [21–23].

The tolerance factor t along with temperature determines the crystal phase of a particular perovskite film. At room temperature a value of t between 1 and 0.89 leads to cubic symmetry and lower values lead to tetragonal and orthorhombic structures. In addition, a value greater than 1 results in layered perovskite structures with abnormal optoelectronic properties, such as broadband white light emission[24–26]. It is regardless possible to have a dynamic transition between phases with changing temperature. For example, the model $CH_3NH_3PbI_{3-x}Cl_x$ perovskite undergoes a phase transition to tetragonal phase on lowering temperature below 330 K and to orthorhombic phase at a temperature below 140K. Crystal phase transitions and tolerance factor plays a pivotal role on perovskite stability. Detailed discussion on this topic is presented in chapter 4 and 5.

## Electronic structure

Researchers have calculated the electronic band structure, density of states and valence band and conduction band extremums of perovskite semiconductors using DFT. Owing to its crystal symmetry, perovskites are direct band gap semiconductors. The conduction band minimum is formed from Pb 6p orbitals and the valence band maximum is formed through strong coupling of the Pb 6s and I 5p orbitals (figure 2.2 b)[10, 28]. The above description is for the archetypal perovskite crystal, $CH_3NH_3PbI_3$. This is in stark contrast to the well studied GaAs semiconductor, where the valence band has p and conduction band has s symmetry. This inverted

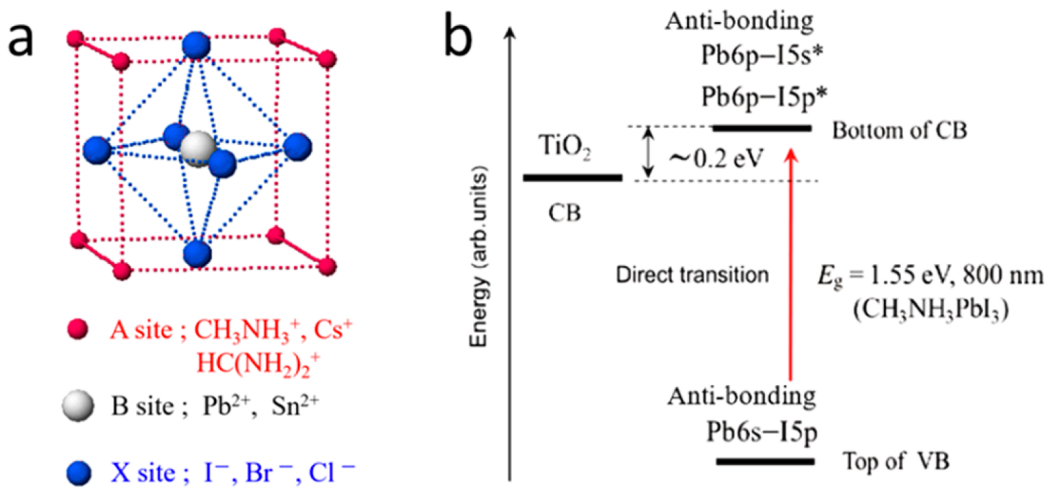


Figure 2.2: Schematic diagram of cubic perovskite crystal showing the positions of A, B and X ions (a). Schematic diagram showing the valence band and conduction band hybridized energy levels of $CH_3NH_3PbI_3$ perovskite crystal (b) [reproduced with permission from ref[4] ©(2019) American Chemical Society]

band structure gives perovskite semiconductors unusual properties leading to unconventional temperature and strain dependent optical behavior (further details in chapter 5). The 6p lone pairs play an important role in the optical and transport properties of perovskite crystals[10]. It is interesting to note that the large A cation does not contribute to the band edges but does play an important part in stabilizing the crystal structure.

Heavy atoms like Pb shows large spin orbit coupling effects, and recently there has been advances suggesting spin orbit coupling induced Rashba like splitting in perovskite crystals[29–32]. These effects are still a matter of debate and lack experimentally validation. An example of a DFT calculated band structure is shown in figure 2.3, indicating the direct band gap at R point in the Brillouin zone.

## Optical absorption

The high optical absorption coefficient ($\sim 10^5/cm$) is an important factor abetting the high PCEs recorded in PSCs[5, 33]. The optical absorption of a photon of energy

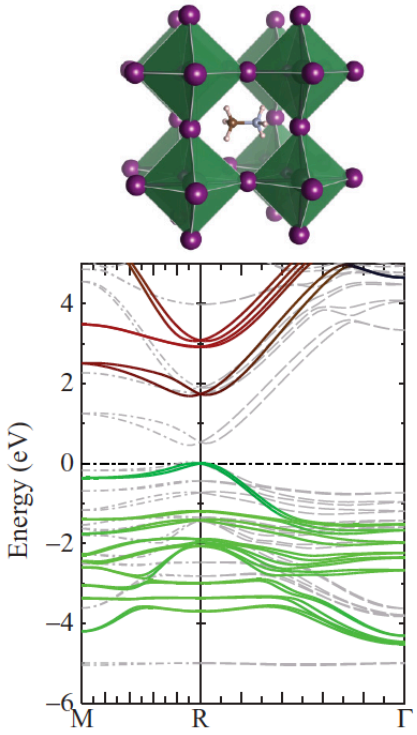


Figure 2.3: Energy bands in halide perovskites calculated using DFT. As shown the direct band gap exists at the R point in the k-space. green depicts I 5p, red depicts Pb 6p, and blue depicts Pb 6s.[reproduced with permission from ref[27] ©(2014) American Physical Society]

$\hbar\omega$ by a semiconductor (no excitons approximation) is given by[10]

$$\frac{2\pi}{\hbar}\int |<v|\hat{H}|c>|^2 \frac{2}{8\pi^3}(\delta E_c(\vec{k}) - \delta E_v(\vec{k}) - \hbar\omega)d^3k \tag{2.2}$$

where the first factor $|<v|\hat{H}|c>|^2$ represents the transition matrix between the valence and conduction bands over the k-space and the second term is the joint density of states (JDOS) between them. Ideally, you want both of them to be high for high optical absorption. The best way to understand this is using the example of Si and GaAs as shown in figure 2.4. From the point of view of JDOS, Si is preferred over GaAs as GaAs valence band is formed from s bands which are more dispersive leading to lower density of states, while Si's valence band is formed from both the p and s bands. However, Si is an indirect bandgap material leading to a lower probability of optical transition as the absorption process requires the assistance of a phonon of

matching angular momentum. Perovskite semiconductors combine both these properties, it has a higher JDOS than GaAs and is a direct band gap materials with a high value of p – p transition matrix, owing to the pair of Pb 6s electrons.[10]

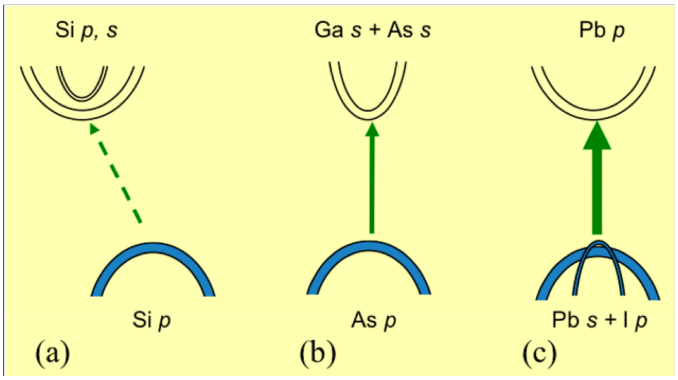


Figure 2.4: Schematic diagram of optical absorption, band orientation and hybridization of (a) Si (first generation) (b)GaAs (second generation) and (c) halide perovskite solar cell absorber [reproduced with permission from ref[10] ©(2015) Royal Society of Chemistry]

Even though, high optical absorption is pivotal for high efficiencies in solar cells with thin absorbing layers, the well-known Shockley-Queisser limit does not factor in this and was later modified by Yu et. al to include absorption dependent terms[34, 35]. Using the modified Shockley-Queisser limit, Yin et. al. calculated that the perovskite thin film of 0.3$\mu$m thickness had a theoretical efficiency of 21% due to its exceptional optical absorption properties, while a similar thickness only resulted in a PCE of 13% in GaAs films[34, 35].

## Charge carrier diffusion

Another important factor leading to high performance of PSCs is its ambipolar conduction of charge carriers. The effective mass m* of a charge carrier in a electronic band is given

$$m^{\star} = \hbar^2 [\frac{d^2(\epsilon(k))}{d^2(k)}]^{-1} \tag{2.3}$$

where $\epsilon(k)$ is the energy dispersion in k-space and is represented by the band diagrams. Intuitively, it is easy to see that more dispersive the band is, the lighter the effective mass will be leading to faster diffusion of charge carriers. In most conventional semiconductors such as GaAs, the conduction band is quite dispersive while the valence band is not, leading to small electron effective masses and large hole effective

masses. For this reason we need p type absorbers in DSSCs.
Intriguingly, the effective masses of both holes and electrons are comparable in perovskite semiconductors, with holes' effective mass actually being lower leading to ambipolar conductivity of charge carriers.[36] This property is attributed to the dispersive nature of p-bands in heavy cations (Pb) as well as as the large dispersion in s-p hybridized bands. This facilitates the p–i–n type PSCs.[10]

## Defect Tolerance

Defect tolerance is crucial for solar cell performance. Most first and second generation solar cells (except GaAs) suffer from low $V_{oc}$ compared to their band gap due to intrinsic defects present in the material. Si solar cells have a band gap of 1.1 eV, while only a $V_{oc} \sim 0.7$eV. PSCs have a $V_{oc} \sim 1.2$eV (bandgap = 1.6–1.7eV), hence the pristinity of the thin films used for device fabrication play an important role in the performance of the solar cell. Trap densities in perovskite have been estimated to be in the range of $10^{10}/cm^3 - 10^{16}/cm^3$ [37–39]. It must also be considered that intrinsic defects can sometimes improve PCE by acting as doping centers that enhance the charge carrier density in semiconductors.

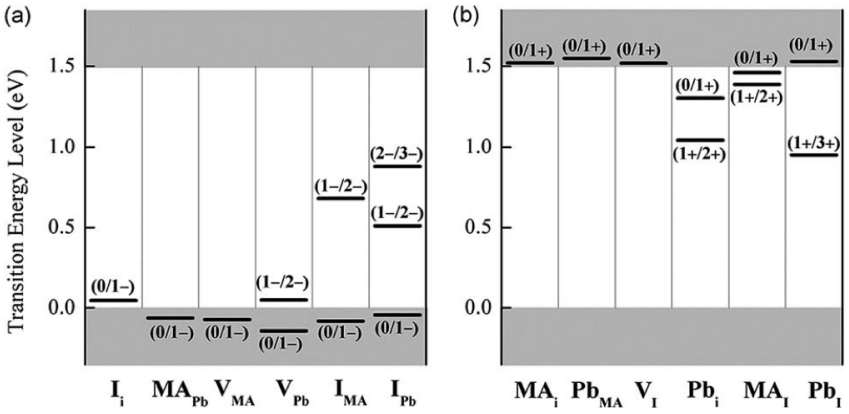


Figure 2.5: Schematic showing the formation energies of different types of defects in PSCs [reproduced with permission from ref[40] ©(2014) American Institute of Physics]

These dopant states can be either donor-like or acceptor like. Their formation energies control the type of dopants present in the material, ergo determining the type (p or n) of charge carrier conduction in them. Their formation energies are decided by the semiconductor growth conditions, such as temperature, precursors, pressure etc. This implies that by carefully controlling the growth one should be able to control

the polar conductivity in the material.

The positioning of the energy level of defect states dictate whether a state act a dopant or a non radiative recombination center. Shallow states where the energy levels lie close to the band edges results in dopant states, i.e. it can lose or gain electrons, while deep defect states, where the energy levels lie near the middle of the band gap acts as traps and will have detrimental effects on the PCE of the solar cell.

Some of the defect state formation energies are depicted in figure 2.5. where $X_i$ represent a interstitial occupancy of an ion, $V_x$ represents a vacancy defect and $X_x$ denotes a substitution type defect. (X = Pb, MA, I)[40]. Most defect forms shallow dopant energy states, while some defect states – $\mathrm{I_{MA}}, \mathrm{I_{Pb}}, \mathrm{Pb_I}$ results in deep trap states and should be prevented.[40]

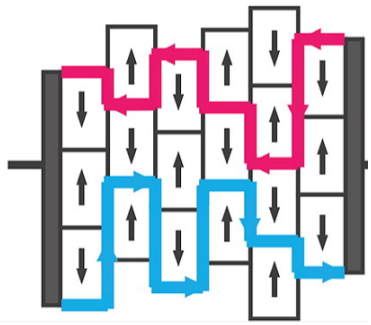

Figure 2.6: In the multidomain ferroelectric electrons will move along minima in the potential, while holes will move along maxima[reproduced with permission from ref[41] ©(2014) American Chemical Society `https://pubs.acs.org/doi/10.1021/nl500390f`]

### Passive grain boundaries

Another type of trap states that result in non-radiative recombination loss are grain boundaries within a thin film. Perovskite thin films used in devices are poly-crystalline in nature, resulting in a large number of grain boundaries. They act as defect centers and have shown to reduce charge carrier lifetime and diffusion lengths, thus reducing the overall efficiencies of the solar cell (eg, CdTe, CIGZ)[10, 42, 43]. Researchers have developed post processing passivation techniques to counter these deep defect states[44]. Yin et. al. in parallel used first principle calculations to show that grain boundaries in halide perovskite are benign and lie deep within the valence band and do not contribute to reduction in device performance. [10] This

demonstrates halide perovskites' robustness and explains why they have high PCE irrespective of fabrication technique.

## Interesting new physics

### Ferroelectric properties

The dipole moment of the non-centrosymmetric organic cation present in halide perovskite results in spontaneous electric polarization in perovskite crystals. These may act as randomly spread ferrolectric domains that aid the separation of excitons to free charge carriers[45]. Another process that can lead to such ferroelectric behaviour is lattice distortions, resulting in asymterric structures with non-zero dipole moments. Frost. et al. calculated that $CH_3NH_3PbI_3$ have a dipole moment similar to ferroelectric oxide $KNbO_3$[41]. A schematic showing the polarization assisted transport is shown in figure2.6

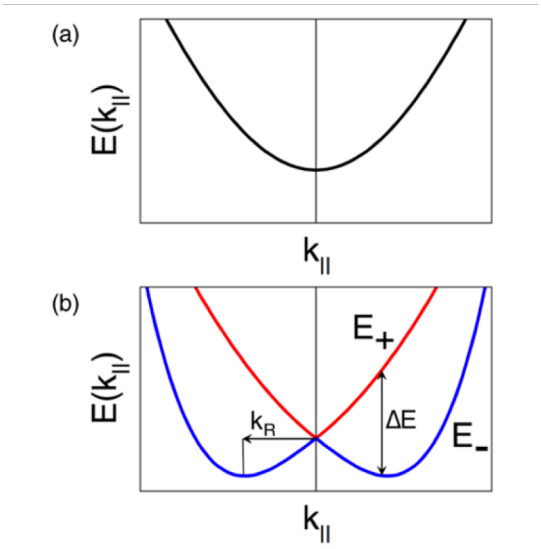


Figure 2.7: Schematic showing the conduction band a) without Rashba splitting, b) with Rashba splitting[reproduced with permission from ref[32] ©(2017) American Chemical Society]

### Rashba splitting

Spin orbit coupling in crystals which lack inversion symmetry result in energy band splitting due to Rashba/ Dresselhaus effect. These effects have been observed in $MoS_2$, GeTe, CdSe etc[46–48]. However, existence of such effects in perovskite crystals

has been controversial, as they do infact have inversion symmetry[49]. Nonetheless, Zheng et. al. argued that structural fluctuations due to thermal energy may lead to local distortion upto a few nanometers, leading to Rashba splitting without requiring the whole crystals to be non-centrosymmetric[50].

Rashba splitting results in a spin dependent splitting of the conduction band. The spin degeneracy (in k-space) is lifted and the bands are split into two separate bands separated by $\Delta k$. A schematic representing this splitting is shown in figure 2.7. It is easy to see the effects of Rashba splitting on the recombination rates of the charge carriers. After direct excitation the electrons thermalize to the valley of the conduction band which is shifted by $\Delta k$ from the valence band minimum, hence requiring a phonon assisted recombination process which has a slower probability and a slower rate. Researchers have suggested this to be a reason for the observation of long lifetimes in perovskite crystals, but experimental evidence of any dynamic Rashba effect in is still lacking.[49]. If indeed Rashba effect exists in perovskite crystals, it can be tactically engineered and exploited for improving device performance. At present, these studies are still in its initial stages and will require further experimental and theoretical studies for validation.

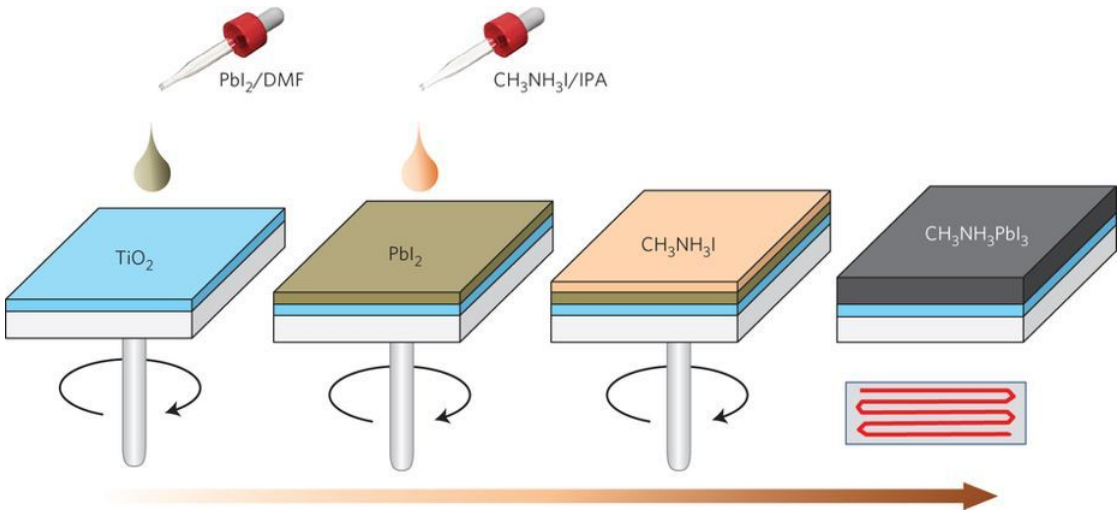


Figure 2.8: Schematic showing two step spincoating of perovskite thin films [reproduced with permission from ref[51] ©(2014) Nature Publishing Group]

## 2.3 Fabrication techniques

Over the years, a large number of fabrication techniques have been developed for the synthesis of perovskite thin film devices. It is difficult to mention all of them in this article, nonetheless, we will briefly discuss some of the main scalable approaches developed. A major portion of the remaining techniques are slight variation of these fabrication routes.

Despite earlier challenges, materials scientists' have successfully fabricated PSCs with high crystallinity, uniformity and purity, In addition, large scale perovskite modules with an area $\geq$ 16cm$^2$ have demonstrated efficiencies upto 16% [52], which is very impressive considering the timescale of PSCs. Solution processability makes perovskite thin film fabrication versatile, cheap and fast.

### Spin coating

Spin coating is the most widely used technique for fabrication of perovskite thin films. It probably is the easiest among all fabrication routes and consists of depositing the precursor solution onto the substrate followed by spinning it at a high speed (2000-5000 rpm) along with subsequent annealing. The most commonly used solvents are di-methyl sulphoxide (DMSO), N-N di-methylformamide (DMP), N-Methyl-2-Pyrrolidone (NMP) etc. The rotational speed along with the viscosity of the solution determines the thickness of the film. This method is preferred for prototyping or lab scale studies of perovskite films and falls short when it comes to scaling or commercializing. One major disadvantage of spin coating is that approximately 90% of the precursor is wasted. Since thin film formation is driven by wetting and thinning of the solution aided by centrifugal forces arising from the fast spinning, it becomes difficult to achieve uniformity with large area films.

The solution chemistry and growth conditions used in spin coating can be transferred to other scalable solution processing techniques and thus helped in developing several existing fabrication routes. Figure 2.8 shows a schematic of a spin coating technique.

### Doctor blading

Perovskite thin films have one of the highest reported PCE ($\geq$ 19% when fabricated using blade coating techniques.[53, 54] Blade coating involves the use of a blade that is used to spread the precursor onto the substrate. The solution used, the speed and distance of the blade from the surface are major control parameters that help in achieving different thickness and morphologies. This techniques is scalable and can be use for roll to roll production of PSCs. Though blade coating technique was

previously used in polymer solar cells, it was Kim et. al who first demonstrated its use in PSCs[55]. Figure 2.9 shows the schematic of blade coating.

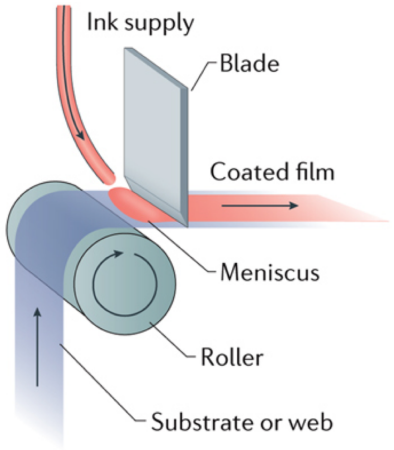


Figure 2.9: Schematic showing blade coating of perovskite thin films [reproduced with permission from ref[56] ©(2018) Nature Publishing Group]

## Slot die coating

Slot die coating is similar to blade coating as shown in figure 2.10. The main difference lies in the fact that the precursor solution is not directly deposited onto the substrate, the blade itself has a small slot which is connected to a precursor (ink) reservoir. Ink flows from the slot onto the substrate as the blade moves across the substrate. Ink flow rate and blade speed can be controlled with high precision enabling fine control over the thin film morphology. PSCs fabricated using this method have however shown to have lower PCE, but higher reproducibility.[57] Further development in ink chemistry is one future direction that researchers expect to see improved efficiencies.

## Spray coating

As the name suggests spray coating involves spraying the precursor solutions onto the substrate before annealing. In terms of scalability and versatility, it is one of the most preferred methods. It is also the preferred route for the fabrication of flexible solar cells. Initial spraying methods showed lower PCE% values and it wasn't until the development of electrohydrodyamic (EHD) spraying by our group(details in chapter 4) that PCEs exceeded 16%[13]. Spraying can done using gas flow, applying an electric

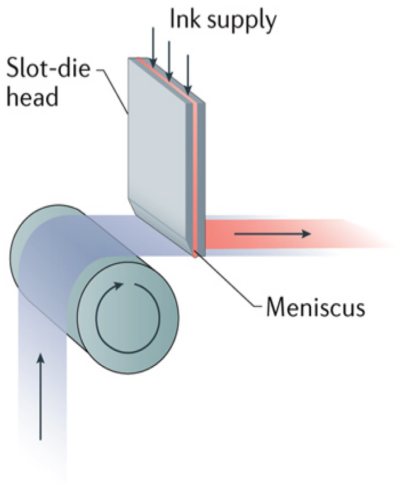


Figure 2.10: Schematic showing slot-die coating of perovskite thin films [reproduced with permission from ref[56] ©(2018) Nature Publishing Group]

field or mechanically. Two major concerns with spray coating is 1)droplets fall at random places leading to non uniform coverage 2)new incoming droplets dissolves already deposited materials, hence requiring rapid annealing. Figure 2.11 shows the schematic of a spraying technique.

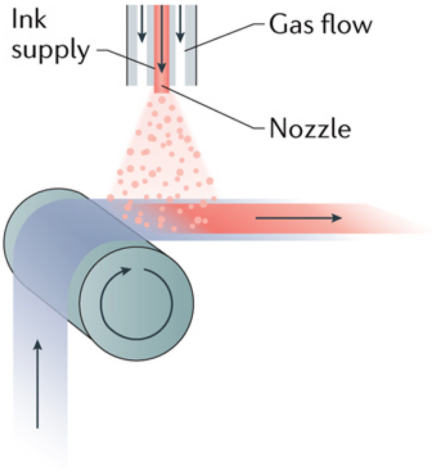


Figure 2.11: Schematic showing spraycoating of perovskite thin films [reproduced with permission from ref[56] ©(2018) Nature Publishing Group]

## Inkjet coating

Inkjet coating uses multiple nozzles for precise deposition of precursors onto the substrate (figure 2.12). Though inkjet coating offers sensitive control over droplet size, lateral resolution etc, further experimentation is still needed regarding its scalability. Initial testing indicated low performances in devices fabricated using inkjet printing. To address this Liang et. al used inkjet printing in parallel with vacuum assisted thermal annealing bringing the PCE to above 17%.[58]

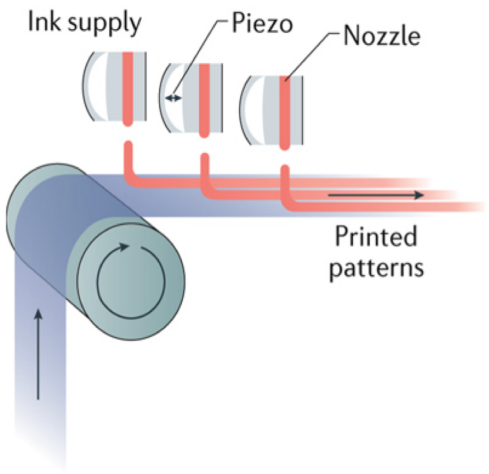


Figure 2.12: Schematic showing inkjet printing of perovskite thin films[reproduced with permission from ref[56] ©(2018) Nature Publishing Group]

## Other fabrication routes

Several variations of the above mentioned techniques were developed by different groups to improve PCE and uniformity of PSCs. A patterned mesh was employed to transfer precursors onto a substrate in a roll to roll manner in a technique called **screen printing**[59]. Some other deposition techniques explored for high performance perovskite solar cells are **electrodeposition**[60, 61], **dip coating**[62], **brush coating**[63] etc. All the above mentioned techniques have their own merits and drawbacks and it will interesting to see which one of them leads the path to commercialization of PSCs.

## 2.4 Working principle

Scientists initially believed that PSCs worked very similar to DSSC, i.e. the perovskite thin film simply acted as an absorber layer.[7] The excited photon results in the formation of electron hole pairs, the electron from the conduction band jumps to the conduction band of the mesoporous $TiO_2$ and then into the counter electrode from where they move to the external circuitry. However, Snaith et.al. showed that PSCs do not need a mesoporous semiconductor scaffold layer, as charge carriers can be conducted through the perovskite layer itself[14]. Therefore it is now accepted that the perovskite solar cells can work in thin film p–i–n configuration, where perovskite thin films form the intrinsic layer sandwiched between hole and electron transport layers.

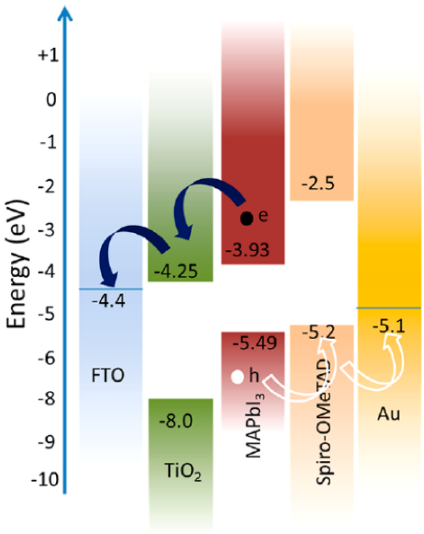


Figure 2.13: Energy band diagram of PSC with $CH_3NH_3PbI_x$ as the absorber layer, $TiO_2$ as the electron transport material and spiro-OMeTAd as the hole transport material. FTP and Au are used as contacts[reproduced with permission from ref[4] ©(2019) American Chemical Society]

The most common architecture for PSC are p–i–n and n–i–p. In the n–i–p structure, $TiO_2$ is the most widely used n type layer placed on the bottom and p type layer is often an organic layer such as spiro-OMeTAD, coated on top of the perovskite layer. The p–i–n structure on the other is termed inverted and has the p-type layer on the bottom, eg Glass/PEDOT:PSS/Perovskite/PCBM[56]. A number of modification to these architectures can be found in literature, such as electron (ETM) or hole transport material (HTM) free, architectures with added scaffolds for charge separation or

with carbon based contacts, etc. A schematic of the commonly found architectures is shown in figure 2.14

## 2.5 Efficiency timeline

As previously described, the first working stand alone PSC by Miyasaka et. al. in 2009 had an efficiency of 3.8%, but since then with improved growth techniques, high crystalline grains and improved ETL and HTL, the efficiency has reached 23.3% (reported by the Chinese Academy of Sciences).[6, 7]

N. G. Park et. al increased the PCE from 3.8% to 6% using perovskite quantum dots sensitized solar cells, which was further improved to above 9% by Kim et.al. by replacing the liquid electrolyte and developing an all solid state solar cell, with spiro-OMeTAD as the ETL[64, 65]. This was a major breakthrough in perovskite's efficiency timeline. Another important landmark in PSCs was the introduction of

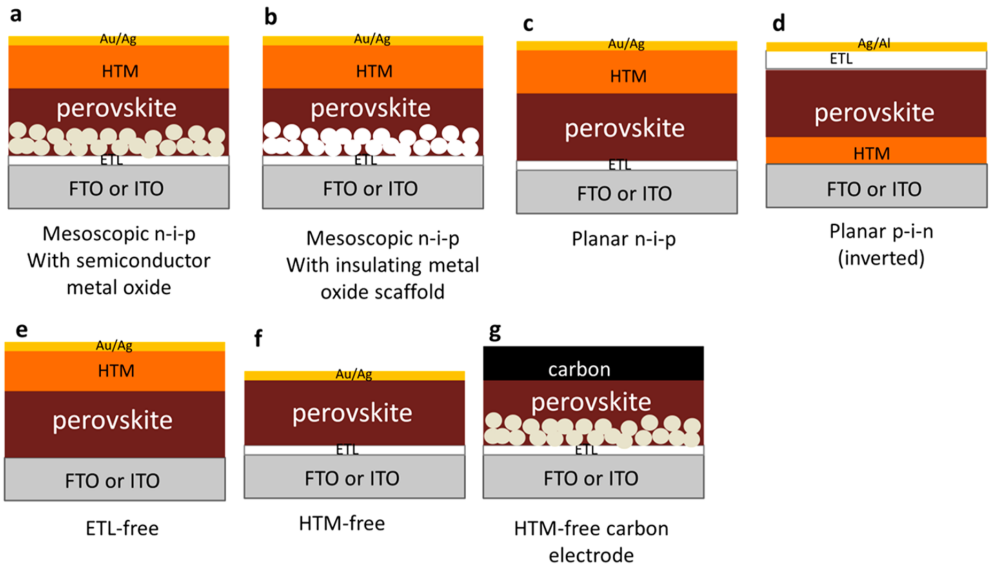


Figure 2.14: Schematic representation of various architectures of PSCs [reproduced with permission from ref[4] ©(2019) American Chemical Society]

mixed halide PSCs. They drastically improved PCE over single halide (Iodide) solar cells. The common mixed halides used were iodide ion with chloride or bromide ions as dopants ($CH_3NH_3PbI_{3-x}Cl/Br_x$). Iodide provided the ideal bandgap for solar cells and chlorine as a dopant is believed to improve charge transport within the thin films. Substitution of iodide ions with chloride or bromide also results in a change

in lattice parameters that can aid in improving stability as well as help in bandgap engineering. Groups have used this to modify the conduction band minimum and valence maximum positions to achieve maximum charge transport in devices.

In 2013, Noh et al. demonstrated that by addition of Br ion in $CH_3NH_3PbI_3$, they can improve the PCE of PSCs to 12.3%[66]. The addition of Br increased the $V_{oc}$ (open circuit voltage) owing to an increase in the bandgap of PSC. But this increase was offset by an decrease in $J_{sc}$ (open circuit current). For initial doping concentrations it was observed that the increase in $V_{oc}$ outperformed a decrease in $J_{sc}$ upto a value of x = 0.29, upon which, further addition of Br led to a decrease in PCE. In parallel, Cao et. al. observed an increase in PCE by 33% (11.03% vs. 10.51%) in PSCs attributed to improved light absorption and enhanced charge carrier lifetime.[67]
Earlier the same year, Snaith et. al. reported a record efficiency of 12.3% by substituting a fraction of iodide with chloride ions[68]. This work additionally employed low temperature processing routes and utilized the ambipolar nature of perovskite films, paving way towards new rapid processing techniques. Mixed halide perovskites with both Cl and Br incorporation were also tested, but their performance was only at par with double halide mixtures.

The next one year from 2013–2014, saw a substantial improvement in PSC performance with PCEs reaching 19% from 12.3% owing to improved fabrication routes with uniform coverage, low defects and large grains.[69] Burshka et. al. used sequential deposition to improve the efficiency to above 15%.[16] A few months later Liu et. al. used ZnO nanoparticles instead of the conventional $TiO_2$ and brought the PCE close to 16%.[70] In Aug 2014, Zhou et. al. reported a major leap in PCE of perovskite solar, by developing a humidity controlled low temperature processing technique enabling the use of high performing charge extraction layers (ITO instead of the conventional FTO) while also substantially reducing interfacial recombination. They reported PCEs of 19.3% in their best performing device with an anti-reflective coating.[69] Formadinium (FA) based PSCs grown with crystallographic orientation further improved the PCE to above 20%.[71] Following fabrication of mixed halide perovskites, scientists forayed into multi-cation perovskite thin films that showed enhanced stability and improved performance. One such result was reported by Saliba et. al using a triple cation based on FA, MA and Cs in PSCs that displayed excellent device stability under illumination with PCE of 21.1% dropping only by 3% ($\sim$ 18%) after 250 hours.[21]

The last few years has seen the focus of PSC research shift from improving efficiencies to increased stability and developing scalable fabrication methods, a prerequisite

for commercialization. Nonetheless, during the same period PCE of PSCs have also gone upto 23.3%[6]. This was achieved using a combination of band engineering and interfacial modifications. In 2017, a PCE of 22.7% was reported by Jung et. al. using P3HT as the hole transport layer.[72] They exhibited high stability (retention of 95% after 1350 h at room temperature) and scalability (24cm$^2$ devices). Jeon et. al. developed fullerene terminated hole transport layer with optimized band orientation and reported a PCE of 23.2% in large area perovskite solar cells.[73] At present, PSCs have reached acceptable efficiencies, while long term stability still needs to addressed before commercialization. Regardless, the future of PSCs looks encouraging and is expected to hit the solar market by 2020. A table with some of the reported PCEs of PSCs is shown below

| PCE | Year | Perovskite compositition | Ref |
|---|---|---|---|
| 3.8% | 2009 | $CH_3NH_3PbI_x$ | [7] |
| 6.5% | 2011 | $CH_3NH_3PbI_x$ | [64] |
| 9% | 2012 | $CH_3NH_3PbI_x$ | [65] |
| 12.3% | 2013 | $CH_3NH_3PbI_{3-x}Cl_x$ | [66] |
| 15% | 2013 | $(CH_3NH_3PbI_x)$ | [16] |
| 19.3% | 2014 | $CH_3NH_3PbI_{3-x}Cl_x$ | [69] |
| 20.1% | 2015 | $(FA_3NH_3PbI_x)_{3-x}(MA_3NH_3PbBr_x)_x$ | [71] |
| 21.6% | 2016 | $(RbCsMAFA)_3NH_3PbI_{3-x}Cl_x$ | [21] |
| 21.6% | 2018 | $CH_3NH_3PbI_x$ | [74] |
| 22.1% | 2017 | NA | [6] |
| 23.3% | 2018 | NA | [6] |

Table 2.1: Summary of some reported PCE in PSCs

## 2.6 Perovskite quantum dots

With progress made into perovskite thin films, researchers started delving into nanocrystals (5–100nm) made of halide perovskites – perovskite quantum dots (PQDs). PQDs have significant advantages over conventional semiconductor quantum dots, due to their ease of synthesis, bandgap tunability, long charge carrier diffusion lengths, improved absorption and high photoluminescence quantum yield. They have found use in photodiodes, quantum dot solar cells, laser gain mediums and LEDs. PQDs have similar crystal structure $ABX_3$ and identical charge carrier properties to their thin film counterpart. Their band gap however can be modified with size, attributed

to their quantum confinement nature.

Most light emission sources require narrow emission linewidth for color sensitivity. Along with narrow linewidths, photoluminescence (PL) characteristic of PQDs exhibit color tunability and high quantum yields, satisfying the important characteristics needed for device applications. Properties of PQDs are identical to perovskite thin films, such as high spin orbit coupling, defect tolerance and inverse band ordering. Some of these properties in a quantum confined system offers additional advantages, for example high spin orbit coupling in a nanocrystal has applications in spintronic devices.

Another important advantage of PQDs is the ease of compositional engineering,

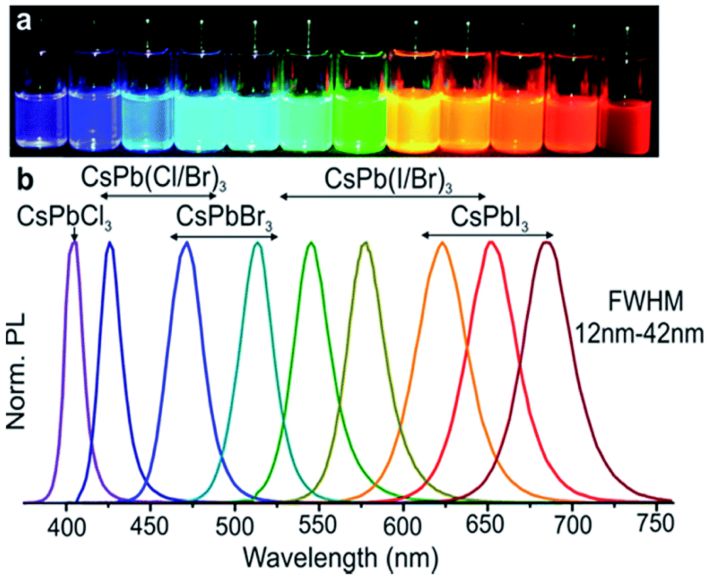


Figure 2.15: PQDs emitting throughout the visible spectrum under UV excitation(a) Their corresponding PL spectra(b) [reproduced with permission from ref[75] ©(2015) American Chemical Society]

providing great flexibility in synthesizing mixed halide nanocrystals. This presents opportunity for modifying the bandgap with composition rather than size, offering better control over the conduction and valence band positions. Due to these reasons, PQD research has made rapid progress in just a few years.

## Fabrication

PQDs are synthesized mainly using 2 solution processed techniques – Hot injection method and ligand assisted reprecipitation

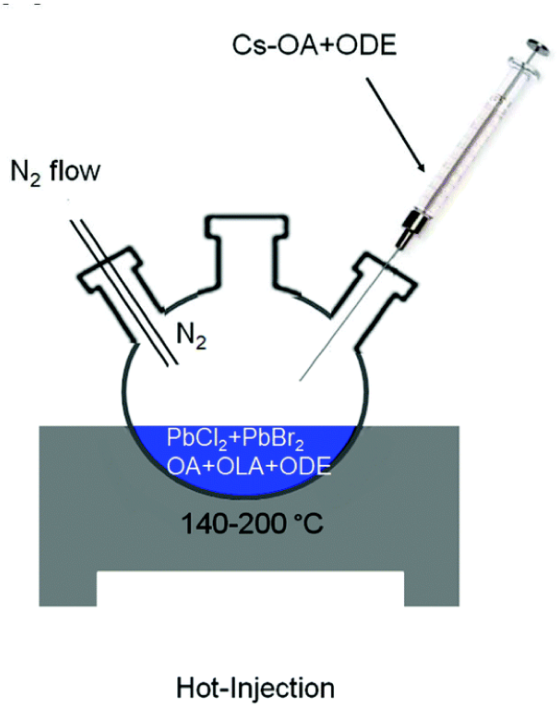


Figure 2.16: Hot Injection Method for growing perovskite quantum dots [reproduced with permission from ref[76] ©(2019) Royal Society of Chemistry]

### Hot Injection Method

Hot injection synthesis is a common method first introduced for the synthesis of CdSe quantum dots, later on adopted for a number of other nanocrystal systems.[77] The procedure involves fast injection (commonly using a syringe) of the precursor solutions into a supersaturated solution kept at an elevated temperature.[75, 78] Schmith et. al. pioneering the synthesis of colloidal $CH_3NH_3PbBr_3$ nanoparticles by mixing $CH_3(CH_2)_{17}NH_3Br/CH_3NH_3Br_3$ with $PbBr_2$ at 80 $^o$C.[79] Initial synthesis showed low PL quantum yield (PLQY) which was significantly improved to 87% by optimizing

the growth conditions. In the following year, Kovalenko et. al. used the same technique to grown inorganic Cs based PQD with very high PLQY of 90%.[75] PQDs did suffer from stability in solution and would precipitate out. This was later overcome with the help of capping ligands, commonly OA (octylamine).[80] Likewise, scientists have also explored other capping (APTES, ODA) ligands for improved stability and PLQY.[81]

#### Ligand assisted reprecipitation

This technique is mostly used for inorganic halide perovskite quantum dot synthesis. It involves reprecipitation through solvent mixing. Halide perovskites are soluble in a large number of polar solvents, but not in non-polar ones. A reprecipitation technique involves saturating the polar solvent followed by quick injection into a non polar solvent.[82] The change in solubility induces the formation of highly luminescent colloidal QDs. A number of polar – non polar solvent pairs were tested. Some of the common ones are DMF – chloroform, DMF – toluene etc. The resultant PQDs were uniform and showed good stability.[83, 84]

## Surface passivation

Quantum dot stability, quantum yield and morphology are strongly dependent on surface passivation. Surfaces of nanocrystals or quantum dots suffer from a large number of dangling bonds, that may act as deep energy defect states. This leads to non radiative recombination and a reduction in PLQY.[80] Hence it is of paramount importance to passivate these surfaces to enhance emission as well as for stability of PQDs in colloidal solutions. A common strategy involves using organic cation such as ammonium ions and organic anions, such as carboxylate ions to terminate the dangling bonds on the surface of PQDs. (3-aminopropyl)triethoxysilane (APTES) and oleylamine are primarily used for amine termination, whereas organic carboxylic acids (CAs), such as oleic acid are used for carboxylate ions.[80, 81] The physical morphologies of the quantum dots also dependent on the steric hindrance or bulkiness of the ligands, for instance a linear ligand leads to less uniformity compared to a branched ligand. Additional details can be found in chapter 6.

## Size insensitivity

Owing to the large Bohr radius of 2.5nm, emission from PQDs are less sensitive to change in size, compared to conventional CdSe quantum dots.[85] This enables researchers to synthesize quantum dots of sizes larger than 10 nm while maintaining the narrow emission spectra. Further, PQDs are also relatively tolerant to slight variations in size and morphology attributed to this size insensitivity.[81] Thus it is

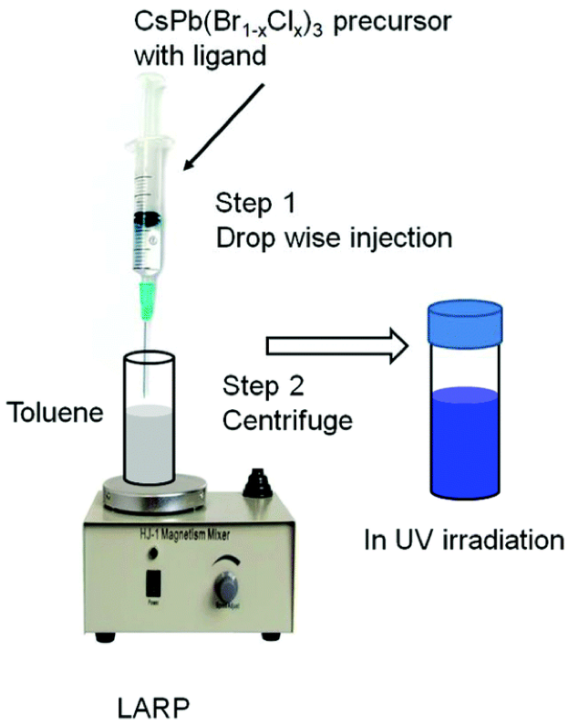


Figure 2.17: Ligand assisted reprecipitation method for growing perovskite quantum dots [reproduced with permission from ref[76] ©(2009) Royal Society of Chemistry]

possible to tune band gaps in PQDs (sizes $\leq$ 10nm) throughout the visible spectrum, solely based on its halide composition. These properties make PQDs an attractive new material for optical and electronic devices.

## PQD devices

PQDs have found multiple uses in devices due to their solution processibility and high PLQY. Some of these applications include solar cells, LEDs, Lasers and single photon sources. Among them, PQD solar cells have shown great promise, as it achieved the highest reported PCE in quantum dot solar cells (13.4%).[86] A brief overview of PQD device technologies is given below:

### Solar cells

Reports on PQD solar cells are limited compared to their thin film or 3D counter part, partly due to their recent development and partly due to low efficiencies reported in other conventional quantum dot solar cells. However, in the relatively small time scale they have shown promising performance as PV materials.

Iodide based PQDs in cubic crystalline phase are ideal band gap solar cell absorber materials, even so, they suffer from conversion to the less suitable orthorhombic phase over a few days in ambient conditions. Swarnkar et. al. showed that methyl acetate stabilizes the cubic structure of $CsPbI_3$ quantum dot films and prevents the undesired phase transition. The resultant PQD solar cell was reported to be highly stable in ambient conditions and had a PCE $\geq 10\%$[87]

Further coating of these films with FA, MA or Cs cation brought up the PCE to 13.4%, which remains the record for the highest efficiency in quantum dot solar cells.[86]

### LEDs

Color tunability, purity and ease of fabrication makes PQDs ideal for light emitting diodes. Nonetheless, charge carrier injection and transport properties needs to optimized to reach high efficiencies. The first reported PQD device with fine narrow line widths were demonstrated using $CsPbX_3$. By varying X, LEDs with all three primary color emissions were displayed. But the devices suffered from low brightness and quantum efficiencies ($\leq 0.12\%$)[88]

An important step that led to higher quantum efficiencies was through improved surface passivation techniques. Li et. al. were able to improve on the initial quantum efficiencies by 50 times (6.27%) through improved passivation.[89] It is to be noted that though surface passivation reduces non-radiative recombination losses, excess amount of ligands can act as insulators in devices.

### Lasers

PQD films have shown amplified spontaneous and stimulated emissions with low threshold pump energy (low as 5 $\mu Jcm^2$).[90] The emissions are stable at ambient conditions and are comparable if not better than existing colloidal quantum dots systems. Amplification in spontaneous emission is understood to be a result of bi-excitonic recombination. Similar to LED devices, the emission wavelength could be tuned throughout the entire visible spectrum by varying the halide composition.

Stimulated emission was observed in $CsPbBr_3$ nanocrystal films in a whispering gallery mode configuration, attributed to a non linear two photon absorption process.[91] The pump threshold was an order of magnitude lower than CdSe quantum dots due to the large absorption cross section area of PQDs. Recently, green light stimulated emission was also reported in PQDs as a result of 3 photon absorption.[92] With impressive performance in just a few years, PQDs show promise as next-generation lasers.

**Single photon sources**

Single photon sources are emitters that exhibit quantum (particle) nature of light. They have different photon statistics and exhibit quantum mechnical properties such as photon antibunching.[93] They are predicted to be used in quantum information technology devices. PL studies of inorganic PQDs revealed photon antibunching (g(2) value $\sim$ 6) and blinking, both characteristic of a single photon emitter.[94] Further studies are needed to explore explore the full potential of PQDs as single photon source.

PQDs albeit relatively new, have exceeded expectations and encourages to show better performance than conventional semiconducting quantum dots. With improved passivation techniques, controlled growth and compositional engineering, PQDs are definite candidates for next generation opto-electronic devices.

## 2.7 Lead-Free perovskites

Lead in perovskites has been a profound concern for its commercialization. Lead being toxic has serious effects on the human body when exposed to unreasonable amounts. They primarily effect the central nervous system and can even prove fatal. It is also rated among the top 10 toxic elements by World health Organization, and its amount is regulated in commercial products. But substituting Pb in perovskite is indeed challenging as PSCs owe their high performance to its high optical absorption and ambipolar charge conduction, two traits attributed to PSCs energy bands that is highly influenced by the Pb ion. Nevertheless, recent efforts have attempted to substitute Pb in PSCs. Tin (Sn) and Germanium (Ge) are the most obvious choices based on ionic size, oxidation and structural stability, although a wide number of alkaline earth metals and transition metals were also considered.

## Tin based perovskites

Due to similar ionic radii (1.35 $\AA$) compared to $Pb^{2+}$ ion, Tin was initially considered as the substitute for Pb in PSCs. Initial characterization of Sn based perovskites, showed encouraging results as it has a lower band gap and higher charge carrier mobility than Pb based perovskite.[95]
Among Sn based devices, a PCE of 0.9% was reported in PSCs using $CsSnI_3$.[96] Further, in 2014 a much higher PCE of $\sim 6\%$ was demonstrated in $MASnI_3$ in mesoporous $TiO_2$ architecture.[97, 98] In this device, Br doping was used to increase the bandgap thus improving the $V_{oc}$ . This result was considered a breakthrough in Pb free PSCs, following which considerable amount of work was carried out on Sn based PSCs

Regardless of Sn based PSCs showing decent performance as PSCs, they suffer from oxidation of $Sn^{2+}$ to $Sn^{4+}$, resulting in self p-type doping that restricts the overall PCE.[99] Another major concern comes from the limited coverage and rapid crystallization in Sn based PSCs. Loi et. al. were able to increase the PCE to 9% (highest in Sn based PSCs) by incorporating phenylethylammonium (PEA) facilitating improved crystalline growth and reducing grain defects.[100] Adding $SnF_2$, and $SnCl_2$ to PSCs, helps in replenishing oxidized $Sn^{2+}$, while using reducing agents aids in preventing $Sn^{2+}$ oxidation.[101, 102] Sn based PSCs show good results for a new developing technology but they fall far behind Pb based PSCs in terms of PCE.

## Germanium based perovskites

After Sn, Ge (Germanium) was the most studied replacement for Pb in PSCs. Though they have a lower ionic radii, Ge exhibited good optical and transport properties owing to the outer most $4s^2$ electrons. Contrary to Pb based perovskite where the band gap predominantly depended on the halide ion composition, band gap in Ge based perovskites showed strong dependence on the cation present. Incorporating bulkier cations can increase the bandgap in Ge based PSCs but their optical absorption yet gets lowered due to a shift from direct to indirect band gap material.[103–105]

Ge based PSCs are still new and initial results have been discouraging as PCEs reported were lower than 1%.[104] One major reason for this low performance is instability at room temperature owing to their low exciton binding energies. Dee this Miyasaka et. al. recently proposed the use for Ge based PSCs as an absorber layer in tandem cells.[4]

Developing Pb free perovskites will resolve toxicity issues of current PSCs. Present results of Pb free PSCs are promising but are still restricted by moderate PCEs and low stability hindering them from replacing Pb based PSCs.

## 2.8 Spectroscopic studies of perovskite semiconductors

In order to better understand PSCs, one of the most powerful tools used is optical spectroscopy. There are multiple spectroscopy techniques that sheds light into the physical properties of PSCs. Optical spectroscopy techniques are contactless, nondestructive methods aiding in the understanding of the electronic structure of materials. Some of the commonly used techniques are dynamic and static Photoluminesence, pump probe optical spectroscopy, (example, transient absorption spectroscopy, transition reflectivity, photon conductivity etc.) Raman and optical absorption spectroscopy etc. Details of some of the techniques we employed are explained in chapter 3. The biggest advantage of optical spectroscopy techniques lies in the fact that they reveal multiple information about PSCs without having any negative impact on its performance. They also help in identifying perovskite materials with superior opto-electronic properties without having to test a full working device. Some of the properties studied using optical spectroscopy are briefly described below:

### Bandgap determination

By studying photon emission or absorption from perovskite semiconductors, it is possible to determine its bandgap, which additionally provides a mean to quantify elemental composition in semiconductor compounds.

### Impurity levels and defect detection

Impurities in semiconductors might result in PL emissions due to deep levels in the band gap. However, these emissions may not occur at room temperature and might require cryogenic temperatures. Temperature dependent PL is a highly sensitive spectroscopy technique and has the potential to identify extremely low concentrations of intentional and unintentional impurities that have detrimental effects on the performance of PSCs or other opto-electronic materials.

### Recombination rates and mechanisms

Using a pulsed laser or by using pump probe techniques, it is possible to understand recombination mechanisms occurring at fast time scales in the order of nano to pico seconds. By understanding the PL decay, relative amounts of radiative and nonradiative recombination rates can also be determined. Other important physical properties determining performance of PSCs are charge carrier lifetime , diffusion lengths and extraction rates, all of which can be quantified using optical spectroscopy techniques.

Optical spectroscopy tools are central for determining and characterizing physical properties of PSCs, abetting the development of new structural compositions and device designs needed for next generation PSCs.

## 2.9 New directions: From spintronics to water-splitting

With perovskite semiconductors revolutionizing opto-electronics research, researchers have recently explored its application in newer technologies. Two such major fields studied were perovskite spintronics and water splitting.

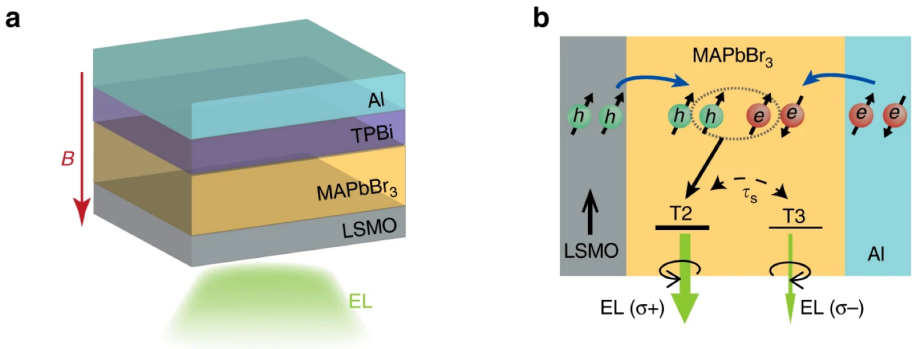


Figure 2.18: Schematic showing a spin injection device (a) and the spin transport in the device(b) [reproduced with permission from ref[106] ©(2019) Nature Publishing Group]

### Spintronics

A spintronic device manipulates electron-hole spins for information storage as well as for charge transport devices, example spin transistors. Though the field of spintronics have been extensively studied theoretically, new materials are constantly investigated for spintronic device implementation.

For a potential use in spintronic device, a material must possess simultaneously both high spin-orbit coupling (a prerequisite for spin manipulation) and high PLQY, needed for opto-electronic devices. Perovskite semiconductors with their recently observed Rashba-splitting, large spin orbit coupling and excellent PLQY are ideal candidates for spintronics.[106]

Since perovskite spintronics is a rather recent research topic, very few experimental validation of their potential use is available. Researchers from University of Utah (Prof. Vardeny and Prof. Li) pioneered the field. They experimentally demonstrated spin injection and Hanle effect in perovskite semiconductors.[106, 107]

Following this, 2 working spintronic devices were demonstrated, a spin LED and a spin valve both based on the archetypal $CH_3NH_3PbI_3$[106]. The device architectures and the working principle of a spin injection device is shown in figure 2.18. Nonetheless, more studies are required to fully understand and implement perovskite spintronic devices.

### Perovskite water splitting

With superior light absorption properties of perovskite thin films, it only seems apparent for it be tested for solar water splitting applications. At standard temperature pressure conditions, a Gibbs free energy of $\Delta G = +237.3$ kJ/mol (non spontaneous) is required for splitting water into hydrogen and oxygen.[108] A working water splitting device thus absorbs photons and utilizes solar energy to overcome this thermodynamic limit. In order to split water, a photocatalyst must exhibit certain properties, it must absorb light about 1.23 eV (1100 nm) and its conduction band extremum must lie below the redox potential of $H^+/H_2$, and the valence band (VB) potential needs be be more positive than the redox potential of $O_2/H_2O$.[108]

It only seems reasonable that perovskite semiconductors with its band engineering properties are an ideal bet for high performance water splitting devices. This was further corroborated by Luo et. al. who showed that an efficiency of 12.3% could be achieved by using $CH_3NH_3PbI_{3-x}Cl_x$ in tandem with NiFe.[109] This was a major breakthrough as current water splitting devices ($Fe_2O_3$, $BiVO_3$ etc) had efficiencies in the range of $\sim$ 2–3%.[110] Regardless of this achievement perovskite based water splitting devices remain a challenge, largely due to electrical and chemical decomposition of perovskite active layer.

## 2.10 Conclusion

We have briefly reviewed the tremendous progress PSCs have made in the last decade owing to their exceptional charge carrier properties, ideal bandgap and solution processibility. Although PSCs have fast tracked their way to commercialization, a number of drawbacks such as absence of a scalable fabrication route, instability and lack of understanding of their atypical physical properties impede them from reaching their full capability. Underpinning the properties leading to high performance

in PSCs could help in designing better device architectures and exploration of new materials with improved performance.

A detailed description of recent progress on perovskite semiconductor research carried out as part of my doctoral thesis is communicated in the following chapters. From developing a rapid fabrication route to studying the physical properties of perovskite semiconductors, we were able to improve on device performance of PSCs, whilst also shedding light into its underlying opto-electronic characteristics.

# Chapter 3

# Experimental techniques

## 3.1 Spectroscopy Methods

Spectroscopy deals with studying the interaction of a medium with electromagnetic radiation (light). This experimental technique primarily deals with the emission, absorption and scattering of photons from a medium and provide insights into the their physical properties. Light is often considered an important experimental tool for elucidating different phenomena in complex systems, ranging from large astrophysical objects to angstrom scale atoms . For almost nearly 400 years, scientists have used light to understand fundamental physics of materials. Materials broadly can be categorized into metallic, semiconducting or insulating and their interactions with electromagnetic radiation could be understood using Maxwell's equations. Spectroscopic studies were key tools for the development of field from quantum mechanics to unravelling the mystery of the atom. They also played a central part in developing new design architectures for opto-eletronic devices.

Here, we will briefly describe optical spectroscopy techniques used as part of this thesis, predominantly in the study of perovskite semiconductors. We used techniques from spatially resolved PL to a combination of dynamic and static photoluminescence, to explore device stability, phase transitions, optical spin injection and charge carrier dynamics in perovskite semiconductors.

### Fluorescence or Photoluminescence spectroscopy

Luminescence is described as spontaneous emission of light from a medium. There are different physical processes that can lead to luminescence, such as chemiluminescence, photoluminescence, electroluminescence etc. In each of these processes, emission of light is achieved via a different physical phenomenon. In chemiluminescence, the product of a chemical reaction exists in an excited state, that decays to the lowest

ground state with the emission of light. While, in PL, charge carriers in the semiconducting material absorb light, resulting in excitation to a higher energy level, followed by decaying to the ground state with simultaneous emission of photons. The luminescence in perovskite semiconductors is a result of PL, i.e. the exciton or electrons are photo excited to a higher energy level.[111]
Using a charge coupled device (CCD), we can acquire an optical image corresponding to the emission of the material. In parallel by analyzing the fluorescence spectra (wavelength/energy vs intensity) we can shed light into the materials' crystal phases, impurity or defect levels and its stability.

A simple fluorescence setup, consists of a tunable light source and a light detector. The light source is typically, a tunable laser (such as the Ti:sapphire laser system), which is preferred over lamps or other sources due to their narrow linewidths that aids precise and controlled excitations. The laser can be tuned to an energy greater than or equal to the energy difference between the energy levels of the material to be photoexcited. The specific wavelength or frequency of the excitation source, is chosen by studying the absorption spectra of the material. Care must also be taken not to excite the sample with energies much higher than the band gap or with very high intensity. The former results in exciting the sample to multiple higher energy states resulting in a number of emission spectra while the latter results in multi exciton/electron processes and large heating that can damage the sample.

An example would be for measuring the PL of perovskite thin films with a band gap of 1.6 eV ( 775nm), we use a laser of frequency 1.8 eV with a power of $\sim 10\mu$W. A spectrometer (Princeton instruments Acton 2500, for most of our measurements)is used to collect light. The light entering the spectrometer is dispersed and focused onto a Charge coupled device (CCD).[112] The CCD is previously calibrated using a known light source (Hg or neon lamp) such that, a photon hitting a particular pixel corresponds to particular wavelength. This way the entire PL spectra (wavelength/energy vs intensity) or map can be acquired. The most widely used method for dispersing light into its constituent wavelengths/colors is using a diffraction grating or a prism.
A fluorescence microscope consists of laser focused down by a lens onto the sample, followed by collecting the emitted light either in back reflection, oblique or in transmission mode. Specific filters must used in the collection path to prevent excitation laser light from entering the spectrometer.

In any optical microscopy technique, the smallest resolvable feature is given by Abbe's diffraction limit.

$$d = \frac{\lambda}{nsin(\theta)} \tag{3.1}$$

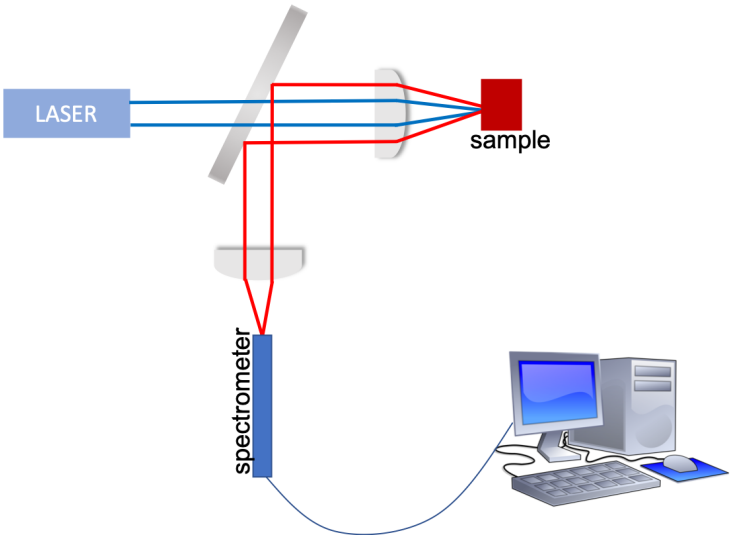


Figure 3.1: Fluorescence microscope in reflection geometry.

where d is the smallest resolvable feature, $\lambda$ corresponds to the wavelength of excitation light and nsin($\theta$) denotes the numerical aperture (NA)given by

$$NA = nsin(\theta) = nsin(arctan(\frac{D}{2f})) \sim \frac{nD}{2f} \tag{3.2}$$

f and D are the focal length and the diameter of the lens, respectively. Hence, for better resolution a small focal length lens, with a large diameter is preferred. A schematic of a fluorescence microscope is shown in figure3.1. In perovskite semiconductors, fluorescence spectroscopy is used to probe crystal phase transitions and defect state emission. The PL is measured as a function of temperature. A phase transition results in a change in the band gap, that translates to a shift in PL spectra. For that reason studying PL as a function of temperature is a useful tool to understand physical properties of perovskite semiconductors. Details can be found in chapter 4 and 5.

For our experiments, we used 3 different laser system, tunable pulsed Ti: Sapphire laser (MIRA laser system, Coherant), Supercontimuum laser system with an AOTF filter (NKT Photonics) and a 409nm diode laser (Cube laser system, Coherant). Princeton instruments' SpectroPro spectrometers in parallel with thermoelectrically cooled PIXIS camera (sensitivity 120-1000nm) setup were used to image the PL. The spectrometer-camera setup has a maximum resolution of 0.4nm (with 1200 g/mm grating @ 435.8 nm).

## Time-resolved fluorescence spectroscopy

Time-resolved single photon counting (TRSPC) or time resolved PL (TRPL) is a powerful tool used in optical spectroscopy to investigate extremely fast dynamics occurring in materials[113]. It involves recording the PL emission as a function of time. This is implemented using a laser pulse, that is used to excite the electrons/excitons in a material to a higher energy state, followed by recording the emitted light using a fast response photodiode. Theoretically, this could be done with just one pulse of laser excitation, albeit this suffers from a number of experimental restrictions.

One of the major restrictions arises from the decay being too fast, hence, getting a full TRPL spectra is difficult. Secondly, TRPL uses low power excitation to prevent multiple excitonic recombinations. Even with high efficiency photodiodes, it might prove difficult to record every emitted photon. Thus, for achieving a full spectrum, averaging over multiple excitations is employed. A common TRPL setup uses

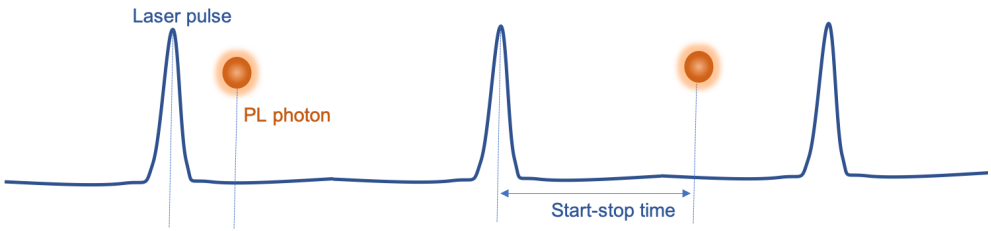


Figure 3.2: Measurement method showing start stop times used to built the probability histogram in a Time-resolved fluorescence measurement

a pulsed laser, that excites the sample and an avalanche photodiode, used to record the emitted photon. Sometimes, a photomultiplier tube (PMT) in used in series with the photodiode for enhancing the signal. The time between the pulse and emission is detected using high resolution ($4 \sim 8ps$) timing electronics (the measurement method is shown in figure3.2). After averaging the time stamped emission signal, a histogram is created to generate Intensity vs time spectra. Within the approximation that photons are emitted from identical emitters, the time resolved spectra corresponds to the excited state probability distribution.

TRSPC comes under the umbrella of ultrafast spectroscopy techniques. The optical setup is similar to a PL or fluorescence setup by replacing the spectrometer with a avalanche photodiode. In order to resolve TRPL of different emission wavelengths, it is possible to use a monochromator and tune it within a range of wavelengths. This can also be done using a much more advanced instrument called a streak camera.

Photon arrival times of different wavelengths are then simultaneously recorded by the camera from which a TRPL spectra of each wavelength can be generated. Streak cameras are however much more expensive compared to a simple avalanche photodiode. For perovskite semiconductors, TRPL is useful to quantify average recombina-

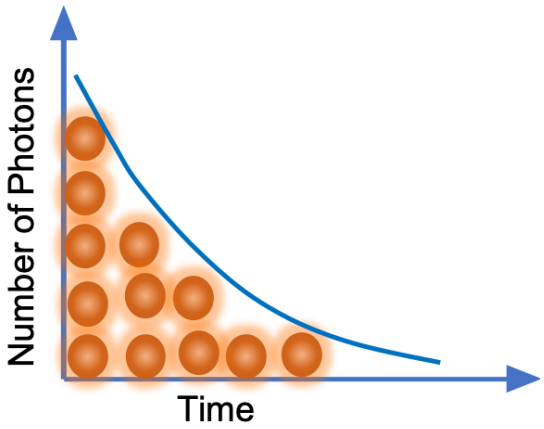


Figure 3.3: Histogram constructed of the emitted photon's start stop times, measured in a TRPL setup

tion lifetimes of excited charge carriers. Studying average recombination lifetimes is found to be a good indicator of solar cell performance and it further assists in probing defect assisted recombination processes and understanding perovskite instability.

In our measurements we used a Silicon single photon photodiode manufactured by Micro Photon Devices (MPD). This was used in series with a PicoHarp 300 TCSPC system that converted the photodiode's response to a digital signal. The measurements were carried out in reflection or oblique geometry similar to fluorescence measurements. TCSPC requires a trigger to start measurements once the perovskite semiconductor is excited using a pulsed laser. This can either be achieved by splitting the excitation path into two, and redirect one into a trigger photodiode, that is connected to the PicoHarp 300 TCSPC system or by using inbuilt electric trigger within the laser system, as in the case of pulsed NKT supercontinuum laser. By varying the length of the electric connection between the trigger and the PicoHarp 300 TCSPC system, the timed separation between the laser pulse and signal curve can be adjusted.

## UV-Visible absorption spectroscopy

Ultraviolet-Visible (UV/Visible) spectroscopy is a technique used to understand light absorption in materials, specifically extinction coefficient of light. Extinction of light is defined as the sum of absorbed and scattered light. A broadband white light source is passed through a sample, and the transmitted light is collected to measure the UV/Vis spectra. The incident light spectra is also acquired by removing the sample from the light path. Absorbance (A) is defined as[114]

$$A = log\frac{I_{in}}{I_{out}} \tag{3.3}$$

where $I_{in}$ is incident light intensity and $I_{out}$ is light intensity after passing through the sample. Baseline correction is another important step in UV/Vis, to account for light scattering arising from external sources. A custom built UV-Vis spectrometer (200nm-1000nm) was used for studying perovskite semiconductors in the following chapters. UV/Vis studies of perovskite thin films and quantum dots were used to study its broad absorption spectra, low Stokes shift and to quantify its chemical degradation.

## Polarization dependent PL spectroscopy

Fluorescence anisotropy or fluorescence polarization is the phenomenon where the light emitted by a fluorophore has unequal intensities along different axes of polarization. It was developed to understand rotation dynamics of molecules, protein folding and chemical kinetics.[113]
Nonetheless, physicists have used polarization dependent PL to study anisotropy in semiconductors arising from spin dephasing in electronic bands. Electronic spins are quanta of intrinsic angular momentum carried by elementary particles such as electrons and holes. Spins have been studied for more than 70 years and recently, have led to the development of the field of 'Spintronics'. Spintronics deals with using spin-charge coupled systems for application in solid state devices and quantum computers.[115]

Polarized light similar to electron spins carry intrinsic momenta, hence angular momentum conservation allows spin injection into semiconductors, through selective excitation using right or left circular polarized light. Polarization dependent excitation in perovskite bands is shown in figure 3.7. A transition with net total angular momentum quantum number change, $\Delta m_J = +1$ can be achieved using right circular polarization light and -1, with left. Now, if the spin dephasing/relaxation time is comparable to inter band charge carrier relaxation times, then the emitted photon will carry the same angular momenta. By studying the polarization of the emitted

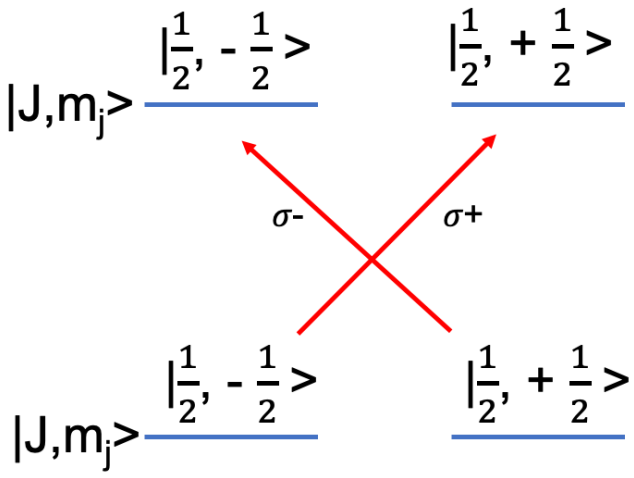


Figure 3.4: Schematic of polarization dependent optical excitation in the energy bands of perovskite semiconductors. $\sigma+$ and $\sigma-$ represent right and left circular polarized light respectively.

photon, it is possible to characterize the electron/hole spin dephasing lifetimes in the system. The polarization P is given by

$$P = |\frac{I_{rcp} - I_{lcp}}{I_{rcp} + I_{lcp}}| \tag{3.4}$$

where $I_{rcp}$ and $I_{lcps}$ stands for intensity of right circular and left circular polarized light respectively. Some example of polarization dependent polarization are Magnetic Optical Kerr rotation spectroscopy, Hanle effect spectroscopy (next section), Current induced spin rotation, Faraday rotation spectroscopy etc.

Right circular and left circular polarized light is generated by using a linear polarizer, kept at an angle of $45^o$ with respect to the fast and slow axis of the quarter wave plate. Additionally, in order to achieve better signal to noise ratio a chopper of Photoelastic modulator (PEM) was used in combination with a lock-in amplifier (further details is in chapter 6).

## 3.2 I-V characterization

The I-V curve of a solar cell is generated by adding light generated electric current to normal diode operation [116, 117]. A solar cell is reverse biased, hence the contribution from diode current is low towards net current density. The diode law

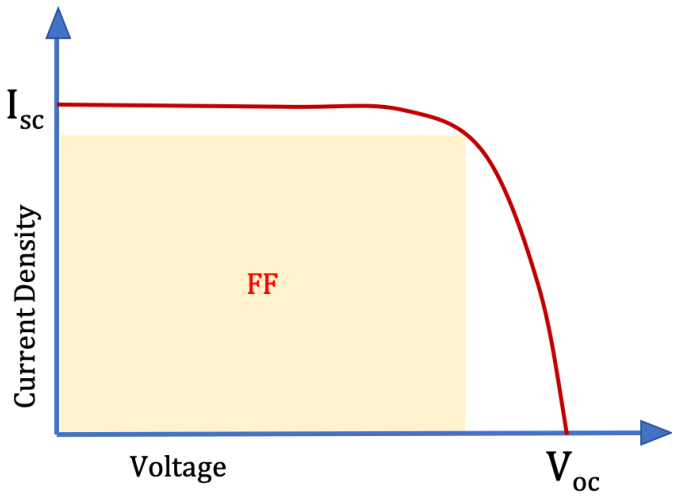


Figure 3.5: Example of a current - voltage curve in a working solar cell. The short circuit current $I_{sc}$ and open circuit voltage $V_{oc}$ are indicated

after correction from photogenerated current becomes:

$$I = I_o(e^{\frac{eV}{KT}} - 1) - I_L \tag{3.5}$$

where $I_L$ is light generated current. V is the voltage, e is an electron charge, T is temperature, and K is Boltzmann constant Short circuit current is calculated by substituting V=0 and open circuit voltage from I = 0, leading to

$$I_{sc} = I_L \tag{3.6}$$

$$V_{oc} = \frac{KT}{q} ln \frac{I_L}{I_o} \tag{3.7}$$

Power conversion efficiency (PCE) of a working solar cell is defined as the percentage of maximum working power generated by the device:

$$\eta = \frac{V_{oc} I_{sc} FF}{P_{in}} \tag{3.8}$$

$\eta$ is the solar cell efficiency, $P_{in}$ is incident power and FF is fill factor (maximum value of the product of current and voltage (I-V)).

Detailed equipments used in our experiments are described in chapter 3.

## 3.3 Hanle effect

Hanle effect is described as the depolarization of emission in the presence of a transverse magnetic field. In 1924, German physicist Wilhelm Hanle observed depolarization of Hg gas emission on applying a weak transverse magnetic field. This effect was later used to measure spin depolarization times in semiconductors, pioneered by Parsons in 1969. It is possible to explain the effect using classical electrodynamics as well as using a quantum mechanical formalism. A brief description of the classical approach is described below: Optical excitation of carriers in a semiconductor using right or left circular polarized light results in spin orientation in the conduction band. The orientational direction of the spins is dependent on excitation light helicity. In parallel, if the electron spin relaxation rates are slower or comparable to electron recombination times, optical spin orientation (let's assume the spin is oriented along the z-axis) can lead to polarized photoluminescence emission. The zero-field spin polarization $S_z(0)$ is given by[118]:

$$S_z(0) = \frac{S_0}{1 + \frac{\tau_r}{\tau_s}} \tag{3.9}$$

where $S_0$ is a constant and $\tau_r$ and $\tau_s$ are the electron recombination and spin relaxation time , respectively. As shown in figure 3.6, applying a transverse magnetic (y direction) field results in electron spin precession around the field with the Larmor frequency $\omega = \frac{\mu_B g B}{\hbar}$ (g is the Landau g factor, $\mu_B$ is Bohr magneton). This precession results in depolarizing of the spin along its initial direction, which increases with the value of $\omega$. Thus, higher the magnetic field, the larger spin depolarization.

The spin component along the z axis is affected by mainly two components, spin relaxation and electron recombination as shown in the above equation. Assuming time t has passed since electron excitation the $S_z$ component is given by $S_o e^{\frac{-t}{\tau_s}} cos(\omega t)$, where the cos($\omega$t) term corresponds to the Larmor precession and the exponential decay term arises from spin relaxation process. The average value of $S_z$ in a magnetic field B ($S_z$(B)) can be obtained by integrating over average spin lifetime distribution W(t)[118]:

$$S_z(B) = S_0 \int_0^\infty dt W(t) e^{\frac{-t}{\tau_s}} cos(\omega t) \tag{3.10}$$

where the W(t) is derived from the expectation value of radiative recombination time $\tau$ , which results in

$$W(t) = \frac{1}{\tau_r} e^{(\frac{-t}{\tau_r})} \tag{3.11}$$

The value of the integral leads to the well known Hanle depolarization curve

$$S_z(B) = \frac{S_z(0)}{1 + (\omega T_s{}^*)^2} \tag{3.12}$$

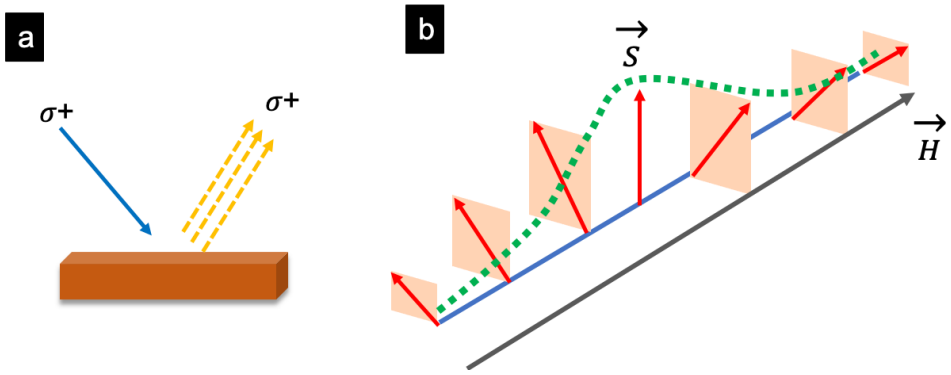


Figure 3.6: Schematic showing experimental measurement in Hanle effect(a). Schematic of spin precession in a transverse magnetic field (b)

where $T_s{}^*$ is the spin decoherence lifetime or spin lifetime related to the electron recombination lifetime $\tau_r$ and spin relaxation time $\tau_s$ by:

$$\frac{1}{T_s{}^*} = \frac{1}{\tau_r} + \frac{1}{\tau_s} \tag{3.13}$$

By measuring the half-width half max of the lorentzian Hanle curve, one can deduce the spin lifetime T*

$$\Delta B_{\frac{1}{2}} = \frac{\hbar}{g\mu_B T_s{}^*} \tag{3.14}$$

Knowing the value of g and electron recombination time, one can calculate the spin relaxation times $\tau_s$.

## Experimental setup

For temperature dependent Hanle effect measurement, the sample is kept in a liquid nitrogen cooled Janis cryostat. Polarized laser excitation was achieved using a tunable supercontinuum laser operating near the semiconductor band edge (480nm for PQDs in chapter7). Circular polarization is generated using a linear polarizer and a quarter-wave plate in series. A tabletop electromagnet is used to apply the transverse magnetic field. The emission is collected in reflection geometry and is investigated using circular polarization analyzer, comprised of a photo-elastic modulator (PEM) (operating at $\lambda/4$) and a linear polarizer (LP). After passing through the analyzer, the emission is focused on to photodiode connected to a Lock-in amplifier, working synchronously with the PEM. The voltage output of the Lock-in at the reference frequency is proportional to $I_{rcp}$-$I_{lcp}$. Replacing the Lock-in amplifier with a multimeter

gives $I_{rcp}$+$I_{lcp}$. Dividing these two terms, the polarization($\rho$) value of the emission can be calculated. $\rho$ is directly proportional to the electron spin projection along the z axis, $S_z$, described in the earlier section. By plotting $\rho$ as a function of B, a Hanle curve is produced.

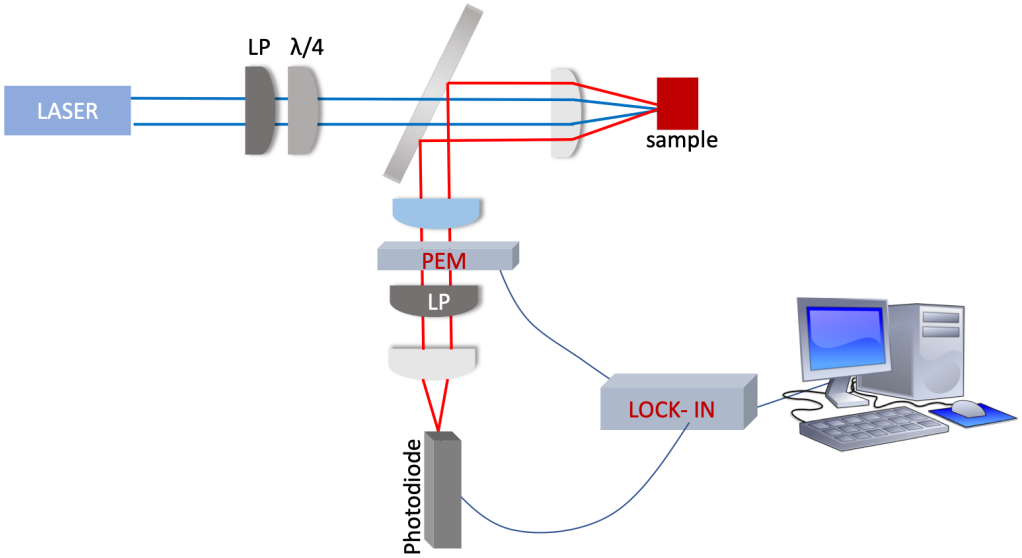


Figure 3.7: Schematic of Hanle effect measurement is shown.

## 3.4 Fabrication

[This section was reproduced from Ref.[13] with permission from The Royal Society of Chemistry.]

### Preparing of perovskite precursors

Hydroiodic acid (HI) (57 wt% in water), methylamine ($CH_3NH_2$) (2 M in methanol), DMF (anhydrous, 99.8%), NMP (anhydrous, 99.5%), DMSO (anhydrous 99.7%), dichlorobenzene (anhydrous, 99%), diethyl ether (anhydrous, 99%) and $PbCl_2$ (99.999%) were used as received from Sigma Aldrich.
Methylammonium iodide ($CH_3NH_3I$, MAI) was synthesized through a modified strategy by reacting 4.2 mL of HI with 15.8 mL of $CH_3NH_2$ at 0 °C for 2 hours in a three-neck flask under a nitrogen atmosphere with constant stirring. The solvent was evaporated from the mixture using a rotary evaporator and a MAI white precipitation

was collected. The crude product was washed with diethyl ether three times and dried under vacuum at 60 $^{o}$C overnight. The dried powder was stored inside a glove box. 420 mgmL$^{-1}$ of MAI and 245 mgmL$^{-1}$ of $PbCl_2$ were mixed together in a mixture of DMSO and NMP (4:6, v/v) at 60 $^{o}$C for 12 h until no visibly distinguishable precipitation. The final concentrations of MAI and $PbCl_2$ are 2.64 M and 0.88 M, respectively.

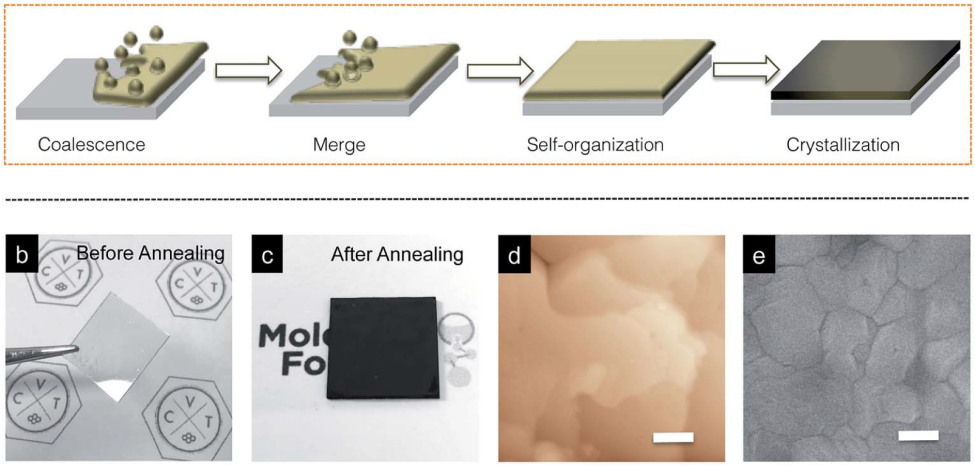


Figure 3.8: Scheme of hydrodynamical growth of perovskite thin films, fabricated using EHD. Photographs of perovskite thin films (b) before and (c) after annealing (d) AFM and (e) HRSEM characterizations of grown perovskite thin film.[Reproduced from Ref.[13] with permission from The Royal Society of Chemistry.]

## Perovskite thin film fabrication

The perovskite precursor solutions with various solvent combinations and volume ratios were fed through a programmable syringe pump at the constant feeding rate of 18 mL/min. A high DC voltage (12.5 kV) is applied between the spinneret and the substrate holder. The distance between the nozzle tip and the ground was kept at 2.5 cm. A multi-jet mode is employed throughout the deposition due to the high coverage and uniformity of droplets. A thermo couple was mounted on to a computer controlled moving stage to closely monitor the surface temperature. The moving speed of the linear motor stage (Newport, ILS 100LM) was programmed at 3.2 mm/s for the single-pass deposition. The total deposition time is 6 to 8 seconds for the thin film thickness of 600 nm. Note that we suggest controlling the speed of moving stage as opposed to altering the concentrations of perovskite precursors for achieving

various thicknesses. Finally, the whole electrohydrodynamic spraying (EHD) was carried out in a humidity controlled ($\leq$15%) fume hood and monitored by a high-speed camera (Phantom) in order to visualize the droplet dynamics.

## Solar cell fabrication

Indium tin oxide (ITO) substrates were treated with UV/ozone for 20 minutes, followed by depositing PEDOT:PSS (AI 4083, Clevios) as the hole transport layer. After spin-coating, the thin film was annealed at 120 $^{o}$C for 20 min. Prior to EHD deposition of perovskite precursors, additional UV/ozone treatment (40 seconds) was employed to enhance the hydrophilicity as well as removing any remaining organic contaminants. The substrate temperature was kept at 35 $^{o}$C to avoid the unwanted coffee ring effect. Flow rate was set at 18 mL/min while the moving speed of the linear motor stage was programmed at 3.2 mm/s . Note that humidity of the fume hood is closely monitored to keep at below 15%. The resulting substrates are immediately transferred to a glass Petri dish for 15 minutes to facilitate the Marangoni flow driven dynamic growth of perovskite grains. On the other hand, to emulate the spray-pyrolysis process, perovskite precursors were dissolved in DMF and sprayed at the surface temperature of 75 $^{o}$C. These substrates were then annealed under a hot-air assisted process to obtain highly crystalline and uniform perovskite thin films.
The continuous heat flow provided a two dimensional, uniformly directional flow at

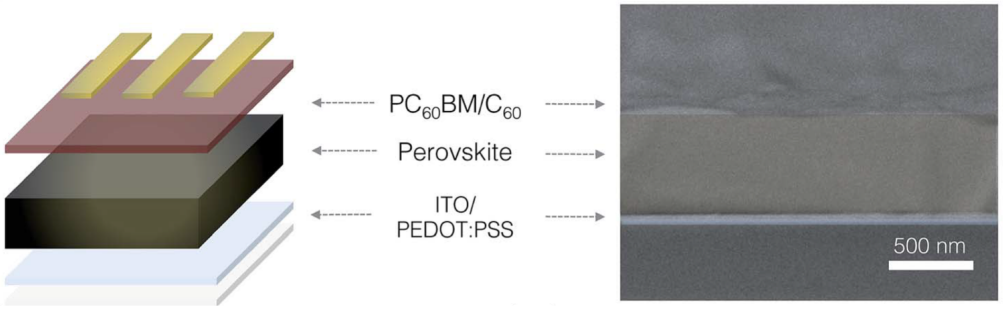


Figure 3.9: Schematic depicts the planar architecture of perovskite solar cell that consist of ITO/PEDOT:PSS/perovskite/$C_{60}$PCBM/$C_{60}$/Al. The corresponding cross-sectional HRSEM image shows the well-defined, continuous interfaces with the neighboring transport layers[Reproduced from Ref.[13] with permission from The Royal Society of Chemistry.]

the air-liquid interface to promote the crystallization of perovskite and remove the volatile byproducts. The distance between the heat gun (ProHeat 1100 Dualtemp,

Master Appliance) and the substrate was kept at 21 cm to maintain a temperature of 110 $^{o}$C at the substrate surface. The moving stage was iteratively oscillated at a speed of 5 mm/s during annealing to ensure uniformity. The annealed samples appeared to be dark brown in color, however at higher humidity the samples turned metallic grayish in color. Next, 2 wt% of $C_{60}$PCBM (Nano-C) dissolved in dichlorobenzene was spin-coated onto the as-prepared thin film at 3000 rpm and then annealed at 100 $^{o}$C for an hour. Another 30 nm of C60 was thermally evaporated as an additional blocking layer. 70 nm of aluminum was then thermally evaporated to complete the devices. The photovoltaic performance was characterized by a Keithley 2400 source measurement unit under a simulated AM 1.5G spectrum. QE-5 measurement system (Enli Tech., Taiwan) was used to acquire the external quantum efficiency (EQE) spectra.

# Chapter 4

# Nature inspired processing route towards high throughput production of Perovskite photovoltaics

## 4.1 Introduction

Nature provides a vast range of inspiring examples of diverse and complex nanostructures in order to achieve several essential functions. For example, the hydrophobic surface on a lotus leaf allows it to self-clean from its residing environment. The microstructure of cork reveals how biological cellular materials can be lightweight yet mechanically resilient, an efficient assembly that allows individual cells to form a honeycomb arrangement. Another compelling example is the formation of 'tears of wine'.

Upon a quick agitation, an instantaneous construction of uniform, self-organizing liquid thin film can be created on virtually any hard surfaces regardless of texture, surface chemistry, and curvatures by making using of surface tension gradient between two dissimilar solvents. In case of wine, the immiscible solvents are alcohol and water, a uniform film is formed on the sides of a wine glass, that falls back down under its own weight appearing as tears, hence the name. In addition, the different evaporation characteristics of individual solvents drive the initially stationary solvent fronts towards un-wetted areas, thus guiding the full coverage of uniform thin films. Specifically, such a scalable, and facile process that allows reproducible control of thickness, and morphological homogeneity at the nanoscale holds tantalizing prospect for printable solar cells, particularly the emerging inorganic-organic perovskite (PVSK) photovoltaics.

Over the past five years, rapid advancement in organic-inorganic perovskites has fascinated scientists across different disciplines because of their appropriate direct bandgap,[33] high absorption coefficient, [119] low processing temperature, [120] exceptional carrier transport, [121] ease of bandgap engineering, [122] long-range carrier lifetime, [69] and most importantly, the potential to achieve grid competitive efficiency over 25% [17, 69]all at a low manufacturing budget[33, 123–125].In particular, the convergence of exceptionally superior output characteristics, low processing temperature, and solution processability makes it possible for the realization of a high throughput, roll-to-roll production process of high efficiency photovoltaics, thus ending the gap between academic prototypes and industrial standards. While the prospect of harnessing these advantageous properties makes perovskites ideal candidates for next generation solar cells, there are roadblocks hindering widespread deployment.

Two of the major challenges are: (a) the lack of a proper processing route that is compatible with in-line production while generating thin films with both the material quality and morphology required to effectively harness solar irradiation and extraction of charge carriers at interfaces and (b) efficient management of the environmentally toxic element, e.g., lead (Pb). Thus far, spin-coating represents one of the most widely employed production routes in solution processed perovskite photovoltaics. Convective flow during spinning and the subsequent evaporation process induce rapid and strong ionic interactions between metal cations and organic anions, leading to the formation of well-crystallized structure. However, the overall morphology is neither homogenous nor continuous over the entire functional area unless lengthy thermal annealing, [126] sequential deposition, [16] multistep solvent infiltration at interfaces, [127] post solvent engineering,[12, 128]or hot casting[129] are implemented. The need for additional processing steps adversely interrupts the fabrication process and creates extra manufacturing complication and cost in scaling up. Further, excessive amounts of perovskite precursor solutions are wasted as a result of centrifugal forces, thus generating unwanted Pb wastes.

Built upon the successful demonstration of printable polymer photovoltaics, [130] spray coating techniques have been revisited to circumvent these formidable challenges as they potentially enable a glass-in-module-out processing technique for cost-effective and scalable production of large-area photovoltaics (the amount of solute directly scales with the volume of the precursor solutions deposited on the substrates). In essence, fine droplets containing perovskite precursors with a polydispersed distribution of diameters are iteratively deposited onto the substrates until a desired thickness is achieved.[131, 132] When incoming droplets meet the surface at a non-zero contact angle, the contact line is pinned to its initial position (4.1) This geometrical

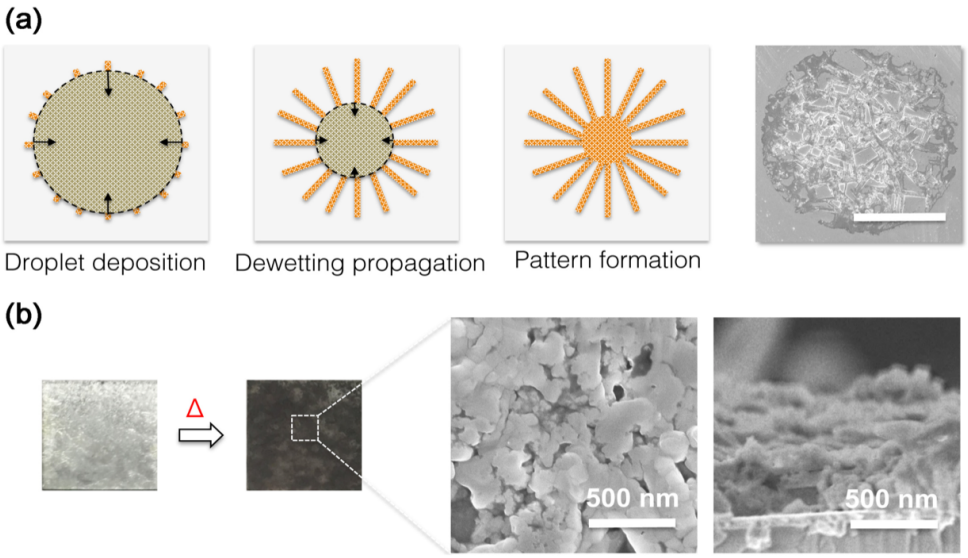


Figure 4.1: (a) Schematic drawings depict the formation of drying patterns as a result of de-wetting process. At the initial stage, the perovskite precursors in the droplet containing only a single solvent precipitates to form spoke like tips at the contact line, which then propagates further inwards as the solvent front (circular dashed lines) retreats, ultimately leading to a spoke pattern. (b) The rich distribution of intra and inter-grain defects; including voids, and grain boundaries adversely affects the propagation of charge carries and the associated photovoltaic characteristics.

constraint limits the interaction between adjacent droplets, preventing coalescing, spreading, and ultimately merging into a uniform thin film. Instead, de-wetting of individual droplets dominates and therefore results in radial, spoke-like patterns of perovskite crystals that not only comprise a high density of intra and intergranular defects but also show extremely rough morphology with peak-to-valley variation of up to a few tenths of micrometers.[132–134] As a result, the overall photovoltaic characteristics still fall short of those made by thermal evaporation and spin-casting counterparts because of the defect plagued morphology (Figure 4.1b).

It is known that the absorption profile and carrier transport of perovskite photovoltaics are highly dependent on the crystallinity, uniformity, and integrity of the perovskite thin film.[135] Furthermore, unlike soft polymeric absorbers with dynamic self-organizing capabilities, the morphological optimization of spray-coated perovskite will have to be completed at the deposition stage before unwanted drying and irreversible crystallization take place at a relatively low transition temperature ($\leq$100

$^{o}$C). In light of this, research directed at understanding how to regulate the deposition of incoming perovskite droplets, i.e., whether a droplet undergoes coalescing, spreading, drying, or de-wetting, is central to the potential for high throughput production of high quality perovskite thin films. This would also hold great promise for reducing the reliance on environmentally toxic Pb through efficient management during deposition. Recent advances in understanding hydrodynamics of liquid droplets suggest that the morphology of the thin film deposition is greatly influenced by their local microenvironment through a combination of geometric and physical cues. To date, geometric stimuli in the form of nanostructured texture and surface tension engineering are the most prevalent and best-characterized approaches to control morphology at the nanoscale. In contrast, relatively little is explored regarding physical routes for manipulating the hydrodynamics of impacting droplets. Understanding the accompanying physical phenomena will permit the direct manipulation of thin film characteristics including coverage, uniformity, thickness, grain sizes, and low grain-boundary activity, ultimately leading to a low non-radiative recombination for high power conversion efficiency (PCE).

Here, we report a continuous liquid interface propagation (CLIP) of perovskites enabled by electrohydrodynamic (EHD), inspired from tears from wine as a potentially scalable, general, and yet versatile nanomanufacturing route to synthesize high quality perovskite thin films with desired morphology, enhanced coverage, well defined crystallinity, and improved photovoltaic characteristics in a rapid and high throughput fashion. It takes at most ∼68 s (a single pass) to create a uniform coating of perovskite thin film with a tunable thickness on a 1.5 cm X 1.5 cm substrate and the results exhibit improved uniformity comparable to that of spin-coating specimens with a peak-to-valley variation of only approximately few nm after thermal annealing. (Highest and lowest achievable thicknesses are 750 and 250 nm, respectively.) The solution-based approach allows for judicious control over thin film thickness, morphology, and uniformity and the flexibility of solution chemistry for compositionally engineered perovskites. Further, incorporating a dual-sourced CLIP approach allows for piecing together building blocks comprised of organic and inorganic moieties without the need for common solvent characteristics. Of particular importance is that the CLIP process significantly reduces the consumption of Pb by two orders of magnitude compared to that of conventional spin-casting, thus mitigating the pressing issues of Pb contamination.

In spray-on solar cell fabrication, atomization of high densities of droplets is employed to ensure a sufficient coverage over the targeted area. From a hydrodynamic perspective, the outcome of the impacting droplets, e.g., merging into thin film or drying individually, is proportional to the product of dimensionless constant of $We^{1/2}$

$Re^{1/4}$ , where We is the droplet Weber number, $We = \rho D V_0^2/\sigma$ and Re is the droplet Reynolds number, $Re = \rho D V_0/u$ where $\rho$, $D$, $V_o$, $\sigma$ and $u$ denote liquid density, droplet diameter, impact velocity, surface tension, and viscosity, respectively.[136–140] It is known that effective promotion of the desired deposition phenomenon requires $u$ and $\sigma$ to be synergistically minimized while concurrently maximizing D.[141] To this end, we have systematically explored several approaches and are particularly intrigued by the readily accessible EHD process as schematically illustrated in Figure 4.2 a and Scheme 4.1. For decades it has been known that EHD can atomize liquid medium for high throughput production of thin film specimens.[142] A high voltage applied between a nozzle and a conductive support plate creates an electrohydrodynamic phenomenon that drives the flow of colloidal dispersions out of the nozzle, which later disintegrates into highly charged droplets. Different from spray coating, where droplets randomly deposit onto the substrates, external electric fields preferentially guide these electrostatically charged droplets onto collecting area, thus significantly enhancing the yield and coverage.

Next, upon the immediate contact of droplets and substrate, saturated solvent vapor at the interface creates a thin lamella on the substrate, providing a low surface tension medium as well as forming a saturated microenvironment around the droplets. In addition, the thin lamella can also be deemed as a seeding layer to facilitate the coalescence of droplets into a thin film. Once the droplets are uniformly deposited, they spread outwards due to surface tension gradients formed between the two dissimilar solvents of varying vapor pressure. This essentially results in a rapid self-assembly process leading to the formation of a uniform thin film without the help of any external stimuli.[143]In other words, incoming droplets continuously coalesce upon deposition, and then dynamically spread into uniform thin films without drying individually.

## 4.2 Results

To benchmark our CLIP process, we focused on the archetypal mixed halide perovskites, $CH_3NH_3PbI_{3-x}Cl_x$ , because of consistent output characteristics when processed in ambient conditions[144]. In a typical deposition, a precursor solution comprising methylammonium iodide (MAI) and lead chloride ($PbCl_2$) (molar ratio, 3:1; 2.64 M for MAI and 0.88 M for $PbCl_2$) is dissolved in a mixture of anhydrous dimethyl sulfoxide (DMSO) and N-methyl-2-pyrrolidione (NMP) with an optimized ratio (v/v, 4 to 6), followed by EHD spraying at a feed rate of 18 $\mu$L $min^{--1}$ , moving speed of the translation stage at 3.2 $mms^{--1}$ , and a surface temperature at 35 $^o$C, respectively. As schematically depicted in Figure 4.2, a high DC voltage (kV) is applied

between the nozzle tip and the metal plate using a computer controlled power supply to generate an electric field that causes charged species within the liquid medium to accumulate near the surface of the pendent meniscus. Upon reaching the threshold electric field (5 $kVcm^{--1}$), the electrostatic stress overcomes the capillary tension at the apex of the liquid cone, giving rise to fine, charged droplets. External electric fields electrostatically guide the charged droplets onto the substrates.

Next, incoming droplets immediately coalesce on the substrate, ultimately merging into a uniform thin film as a result of much reduced surface tension. Unlike the conventional spray coating approach where droplets contract right after deposition, the resulting thin film is strikingly uniform over the entire substrate and remains yellowish and wet even after 15 min inside a petri dish. This is intriguing as most of the perovskite thin films made by spray-coating quickly turn into a hazy brown color right after deposition even if solvents with high boiling points are used. Finally, the color of the perovskite thin films gradually turns into a dark brown to matte black upon a heat-gun-assisted annealing at 110 C for 6 min as indicated in the inset of Figure 4.2 b and Scheme 4.1b. The X-ray diffraction (XRD) pattern confirms the highly crystalline and oriented nature of the perovskite thin film emanating from the sharp (110) and (220) peaks, respectively (Figure 4.2 b). In parallel, the morphology of perovskite thin film fabricated by CLIP process was systematically examined through both atomic force microscopy (AFM, Figure 4.2 c) and scanning electronic microscopy (SEM, Figure 4.2 d), respectively. The resulting thin film not only shows a smooth topology with the root mean square roughness of only a few nm but also reveals a random distribution of micrometer-sized grains interspersed between interconnected crystalline networks. This is in a stark contrast with previous strategies, as the deposition duration of the proposed EHD spraying is remarkably short and does not involve heat-assisted flash welding of crystalline domains or the post-diffusion of secondary solvent with immiscible solubility characteristics.[17, 129] Intuitively, one would expect that the underlying mechanism of the EHD-enabled CLIP process to greatly resemble that of polymer-blended composites, e.g., solvent vapor-induced self-organization. In such systems, solvent evaporation gradually drives the formation of molecularly ordered and sterically interlocked stacking between polymers and fullerene additives.[145] It has been shown that the optimization of morphology in the polymer blended cases predominately hinges on the degree of solvent engineering. In contrast, the self-organizing feature in CLIP process occurs in a hierarchical and more prompt fashion.

At a molecular level, the charged droplets provide seemingly infinite interfaces for efficient intercalation of MAI and DMSO between $PbCl_2$ to take place, thus forming an MAI-$PbCl_2$-DMSO intermediate phase similar to that previously reported.[17]

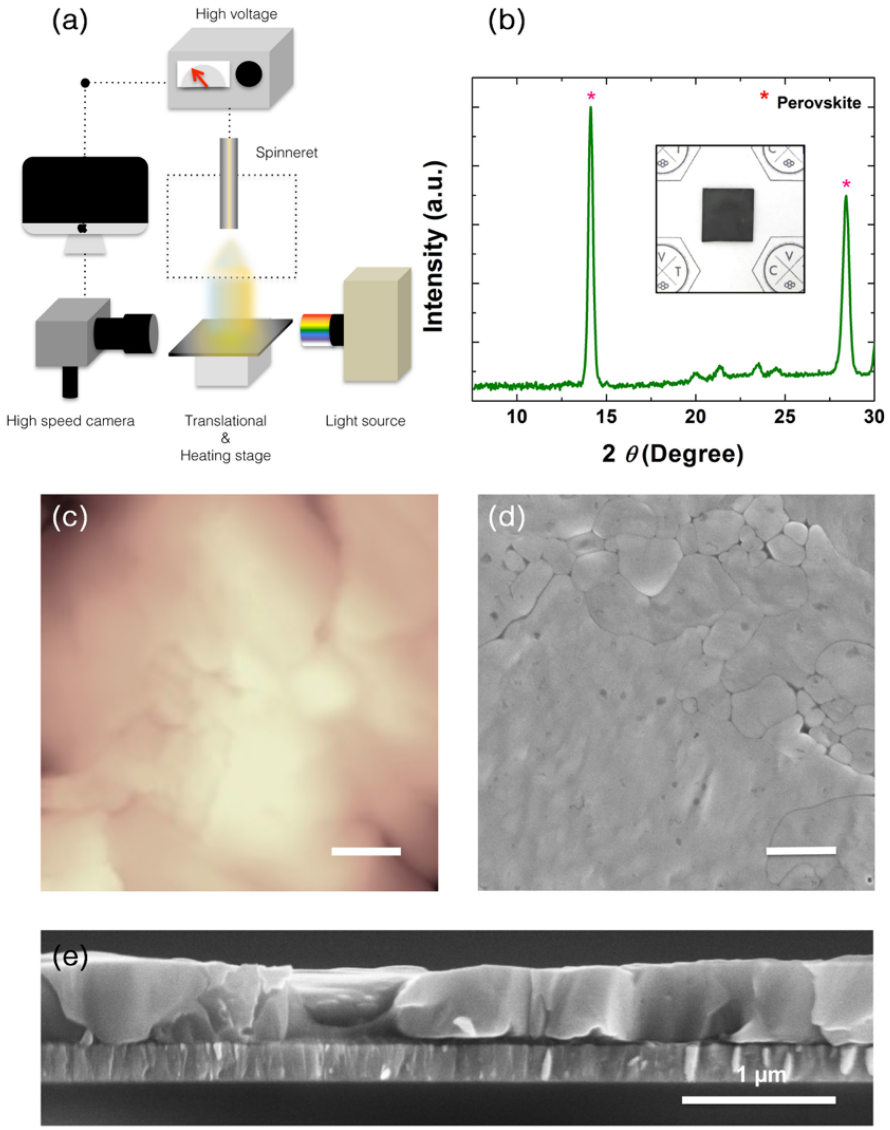


Figure 4.2: EHD assisted CLIP production of perovskites. (a) Schematic illustration depicts the setup of the EHD-assisted CLIP process. (b) XRD, (c) AFM, (d) SEM, and (e) corresponding cross-sectional SEM collectively show the crystallinity, uniformity, and integrity of the perovskite thin films. Inset displays the perovskite thin film deposited on an ITO substrate. Scale bars are 2 $\mu$ m in AFM and SEM, respectively.

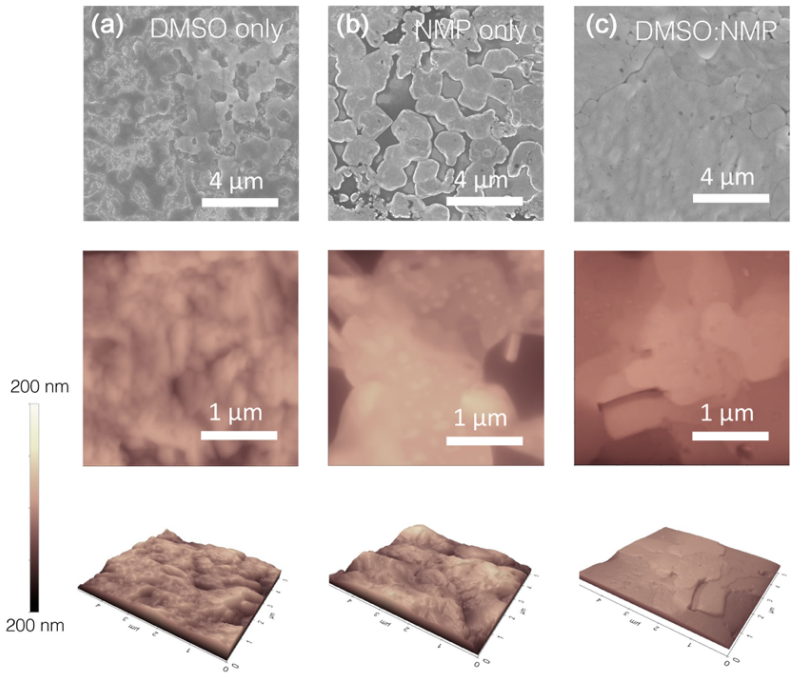


Figure 4.3: Morphological, topological, and 3D profile characterizations. Morphological features (top panel), topological variations (middle panel), and 3D profiles (bottom panel) of (a) DMSO only, (b) NMP only, and (c) the combination of both solvents collectively underscore the importance of self-organizing features enabled by nano-Marangoni flows. Thin films without nano-Marangoni flow often display jagged edges, and rugged terrain, adversely affecting the efficiency of carrier transport.

Wet films made of intermediate phases are known to be very uniform, flat, and self-organized in nature, forming a solid foundation for subsequent conversion into the perovskite phases with desired morphological features. At the nanoscale, the combination of two solvents with dissimilar fluid dynamic characteristics (where the two miscible liquids differ by their volatility and surface tension) tends to create preferential evaporation of the relatively volatile solvent, e.g., DMSO (DMSO, surface tension of 43.54 $\mathrm{mNm}^{-1}$ at 20 $^{o}$C and b.p. of 189 $^{o}$C; NMP, surface tension of 40.79 $\mathrm{mNm}^{-1}$ at 20 $^{o}$C and b.p. of 202 $^{o}$C). The locally unsaturated vapor pressure therefore drives the spreading phenomena, originating from a nano-Marangoni effect (tears of wine), that can be expressed as

$$V_c^2(x) = \frac{1}{2\eta(x)} \frac{d\sigma}{dx} x(1-x)(-A_1\alpha_1 + A_h\alpha_h) \tag{4.1}$$

where $V_c$ is the Marangoni velocity, $\eta$ is the viscosity of the film, $\sigma$ is the surface tension, x is the volume fraction of the low surface tension solvent, and A is the evaporation capacity, induced by evaporation from a two-component mixture.[145, 146] Further, the formation of such dynamic solvent fronts also in turn mobilizes the initially static pinning lines to recover the un-wetted areas and pinholes (stage II, figure4.1), forming a homogenous film. We thus summarize that the combination of these advantageous self-organizing features at different length scales simultaneously and continuously triggers the continuous liquid interface propagation of MAI-$PbCl_2$-DMSO intermediate phases upon deposition. Indeed, morphological and topological characterizations as well as perspective views from 3D profiles collectively corroborate the proposed mechanism (Figure 4.3).

Although perovskite droplets made of a pure DMSO microenvironment did settle and merge into thin films upon deposition due to the formation of self-organizing MAI-$PbCl_2$-DMSO intermediate phases, it is the lack of secondary solvent that results in the static solvent fronts and unwanted contraction leading to non-uninform coverage. Consequently, such thin films tends to rupture upon thermal annealing and thus exhibits inhomogeneous morphology filled with voids and rugged terrains, leading to a height variation of upto few tenths of micrometers (Figure 4.3 a). In the pure NMP control experiment, retraction process dominates as perovskite thin films quickly break into separate droplets during EHD deposition, thus leaving behind a spike-like morphology with discontinuous grains and distributed craters after thermal annealing as shown in Figure 4.3 b. The formation of these largely uneven and separated perovskite islands is problematic as the subsequent deposition of electron extraction layer, e.g., fullerene derivatives, forms a direct contact with the underlying hole transport layer, creating energetically unfavorable shunting pathways.

Such discrete perovskite islands converge into densely packed and morphologically uniform thin films when the optimized bi-solvent composition was reached (Figure 4.3 c), thus underscoring the importance of self-organizing methodology. Detailed processing conditions can be found in the Experimental Section. The ability to create uniform perovskite thin films with continuous crystalline grains in all directions also greatly enhances the reproducibility, fidelity, and scalability for subsequent photovoltaic fabrication. The cross-sectional SEM images reveal more information about the crystalline size. Unlike the conventional spray-coating that typically exhibits a coin-stacked crossection, the perovskite thin films prepared by the CLIP process displays sharp and continuous interfaces with the absence of apparent grain boundaries even when thickness exceeded 1$\mu$m. This translates to the photogenerated charge car-

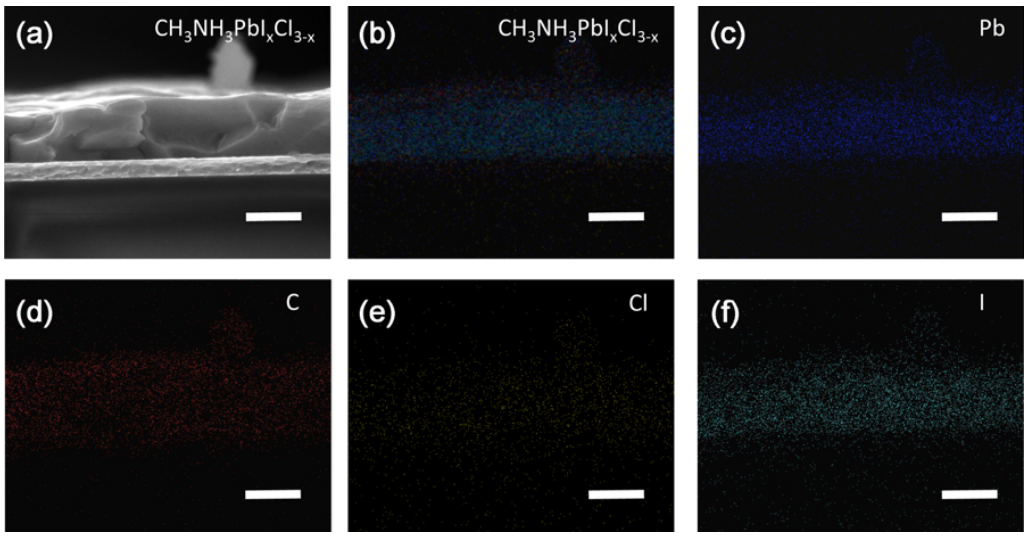


Figure 4.4: Spatial distribution of relevant elements within perovskite thin films. (a) Cross-sectional SEM image reveals the chunky, continuous crystalline grains of perovskites. The exceedingly large grains produced by one step CLIP process establish uninterrupted pathways for dissociated carriers between cathode and anode, without encountering the energetically unfavorable traps. Corresponding EDX mapping shows the spatial distribution of relevant elements within perovskites, including (b) overlaid $CH_3NH_3PbI_{3-x}Cl_x$, (c) Pb in blue, (d) C in red, (e) Cl in yellow, and (f) I in cyan, respectively. Scale bars are 500 nm.

riers being able to leverage the energetically favorable, readily established transport pathways in both in-plane and out-of-plane directions within the perovskite thin films. UV-vis absorption spectra, especially the increasing band-edge absorption around 750 nm, scale well with the increased thickness of the perovskite thin films.

In parallel, the uniformity and/or the complete reaction of the perovskite precursors are also evident in the energy dispersive X-ray spectroscopy (EDX) mapping elemental analysis. We mapped out the relevant elemental distribution (Pb in blue, C in red, Cl in yellow, I in cyan, and the mixture of all three elements) with EDX in the cross-sectional SEM as shown in Figure 4.4 . While the outlines of Pb, C, and I overlay very well with the corresponding crosssectional SEM image, the Cl map only shows limited distribution throughout the entire cross section. The calculated atomic ratio of Cl/(Cl+I) is way less than 2% reported previously, and is significantly lower than that of the compositional stoichiometry in the precursor solutions due to the removal of volatile byproducts, $CH_3NH_3Cl$ (MACl) during annealing and growth.

While the role of Cl has not been conclusively determined yet, several reports have collectively pointed out the existence of Cl ions effectively promote the crystal growth in a 3D fashion and help improve with associated charge carriers dynamics.[60, 147] These compelling structural and morphological features collectively make CLIP assembled perovskites well suited for opto-electronic applications.

## 4.3 Photovoltaic measurements

A planar photovoltaic cell that comprises indium tin oxide (ITO)/poly(3,4-ethylenedioxythiophene)polystyrene sulfonate (PEDOT:PSS)/perovskites/phenyl-C61-butyric acid methyl ester ($C_{60}$PCBM)/fullerene ($C_{60}$)/aluminum (Al) was fabricated and systematically examined. The perovskite thin film with thickness of 600 nm was directly deposited through the EHD-assisted CLIP process (electric field of 5 kVcm$^{-1}$ , flow rate of 18 $\mu$L min$^{-1}$ , deposition time 6 s, and surface temperature of 35 $^{o}$C) onto ITO substrates pre-coated with a thin hole transport layer of PEDOT:PSS (40 nm), followed by a heat gun annealing process at 110 $^{o}$C for 6 min (Scheme 4.1b). Note that the uniformity of thin films can be further improved by a short UV-ozone treatment (40 s) on PEDOT:PSS prior to perovskite deposition. Next, an electron extraction layer of $C_{60}$PCBM (2 wt% in dichlorobenzene) was directly spin-coated at 3000 rpm onto the perovskite layer and then annealed at 100 $^{o}$C for an hour. Another layer of $C_{60}$ (30 nm) is thermally evaporated to act as both an additional blocking and electron transport layer. Finally, Al electrodes were thermally evaporated to complete the device. Figure 4.5 a schematically illustrates the final device architecture and the corresponding false colored, cross-sectional SEM image. Sharp and well-defined interfaces between perovskite (light gray) and neighboring transport layers with $C_{60}$PCBM/$C_{60}$ in magenta and PEDOT:PSS/ITO in blue are clearly distinguished. In particular, the continuous, slab-like grains extend effectively to bridge between the separate charge carrier extraction layers.

Self-dissociated charge carriers under external electric fields can essentially propagate to the collecting electrodes without encountering energetically unfavorable traps. Indeed, average current-voltage (I-V) output characteristics from 20 devices depicted in Figure 4.5 b collectively show a short circuit current ($J_{sc}$) of 21.07 mAcm$^{-2}$, an open circuit voltage ($V_{oc}$) of 0.97 V, and fill factor (FF) of 0.72, thus giving rise to average power conversion efficiency (PCE) of 14.68% under AM 1.5G. The reported PCE represents a nearly two-fold increase compared to that of conventional spray-pyrolysis approach ($J_{sc}$ of 14.90 mAcm$^{-2}$, $V_{oc}$ of 0.84 V,FF of 0.63, and PCE of 7.88%) and is highest among all the spray-coated approaches.[132] We occasionally observed that PCE well exceeds 16.50% but havent reported it here, as we are

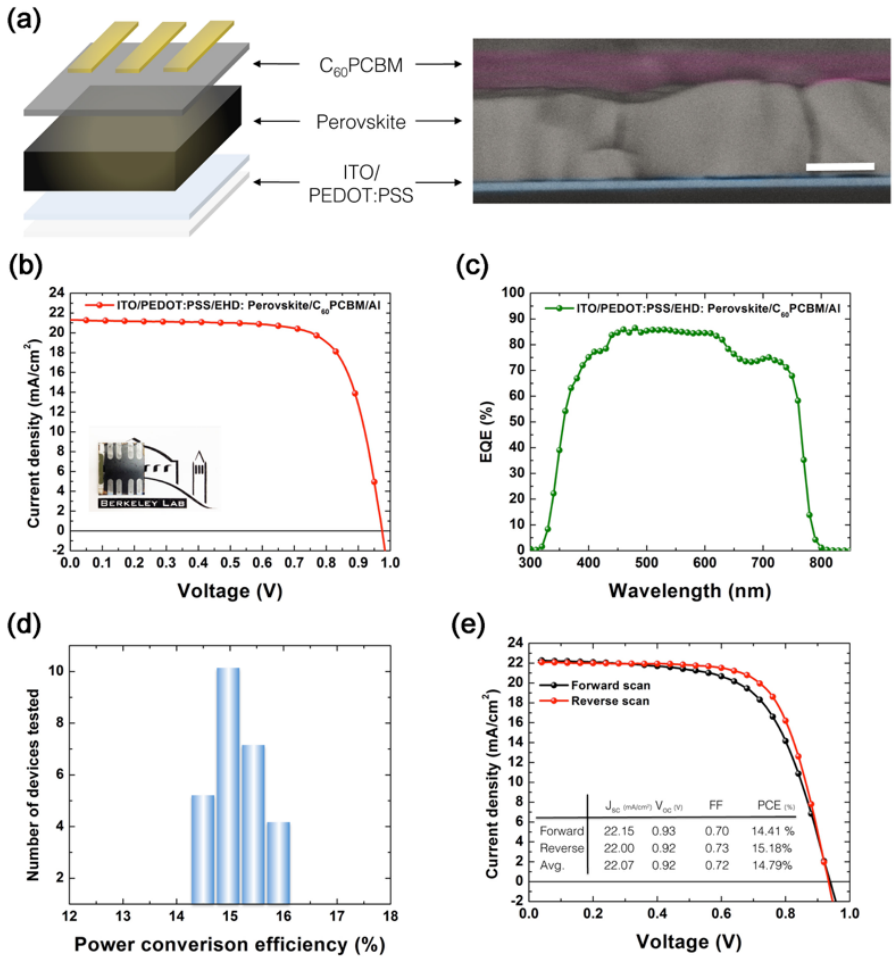


Figure 4.5: Device architecture, and output characteristics of planar perovskite solar cells. (a) Device architecture of the planar perovskite solar cell comprises of ITO/PEDOT:PSS/Perovskite/$C_{60}$PCBM/Al. The false-colored, cross-sectional HRSEM image shows the well-defined interfaces between each layer. Scale bar is 500 nm. (b) I-V curves, and (c) corresponding EQE are obtained and averaged from 20 devices. (d) Histogram of photovoltaic efficiency for 26 devices shows the reproducibility, and low variability of quality perovskite thin films produced by the EHD-assisted CLIP process. (e) I-V curves measured in forward (short circuit to open circuit), and reverse (open circuit to short circuit) directions with 10 mV voltage steps, and 40 ms delay times under an AM 1.5G illumination. Inset shows the table of output characteristics, including forward, reverse scans, and the average of both, respectively.

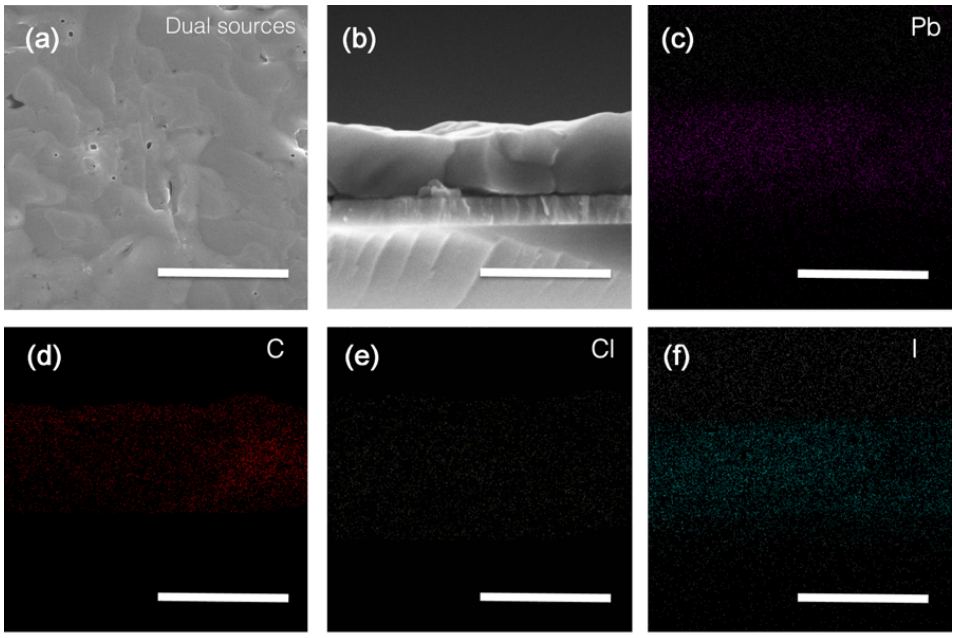


Figure 4.6: (Both (a) top, and (b) cross-sectional views of dual-sourced CLIP generated perovskite thin films collectively reveal uniform coverage as well as large and contiguous crystalline grain formation. Note that the dual-sourced CLIP process requires a longer reorganization time to pave a full, mostly pinhole free coverage. EDX mappings reveal the spatial distribution of relevant elements including (c) Pb in purple, (d) C in red, (e) Cl in yellow, and I in cyan, respectively. The overall mappings overlay well with the cross-sectional SEM images. Scale bars are 2 /*mu*m.

still optimizing the conditions. Nevertheless, given the relatively simple device architecture, we envision that the output characteristics can be readily improved by the interfacial engineering and by use of double blocking layer to suppress the possible leakage current. Meanwhile, external quantum efficiency (EQE) spectrum shows an onset of photocurrent at 790 nm, a characteristic bandgap of $CH_3NH_3PbI_{3-x}Cl_x$. The EQE gradually increases in a monotonic manner and reaches a plateau at 625 nm. Specifically, the average EQE is beyond 80% at the spectral range of 450-600 nm. The facile and high throughput CLIP process also shows a high reproducibility as is evident in the narrow distribution of histogram of photovoltaic PCEs over 20 devices shown in Figure 4.5 d.

In addition, the utility of the versatile CLIP approach is further demonstrated by the incorporation of dual sources (Figure 4.6a). This dual-sourced setup bears

a close resemblance to that of vacuum evaporation where building blocks comprised of organic and inorganic moieties can be rationally pieced together without the need for common solvent characteristics. As a first proof of concept, perovskite precursors dissolved in NMP and DMSO, respectively, were sprayed from two different sources. Similar to the single sourced CLIP process, incoming droplets first quickly merge into a semi-transparent thin film but slowly turned to a yellowish color after being placed inside a petri dish for few minutes (Figure 4.6b), presumably due to the relatively slow intercalation, organization, and optimization of perovskite precursors at macroscale. Aside from the prolonged diffusion process at interfaces, the resulting thin film converts into well-crystallized perovskites thin films with comparable morphology and compositional distribution after thermal annealing (Figure 4.7). XRD, UV-vis and output I–V characteristics further confirm the preserved quality, integrity, and photovoltaic properties of perovskite active layers produced by the dual-sourced CLIP process. With a wide variety of the organic/inorganic precursors, we envision that a wealthy suit of novel perovskites that combine complementary strengths from two different chemical worlds can be rationally and compositionally created, thus greatly enhancing the complexity and functionality.

The ability to create contiguous and crystalline grains also manifests in the steady output photovoltaic characteristics as a function of increasing thicknesses. It is known that grain size plays a pivotal role in efficient transport of dissociated charge carriers. In most sprayed coated perovskites, the thin film is largely limited to around 400 nm in order to match the in-plane dimension of grains. Consequently, the $J_{sc}$ is significantly lower than that of thermal evaporation and solution process counterparts due to the limited absorption profile. When thickness increases, the output I-V characteristics quickly deteriorate because of the defect-plagued transport pathways, particularly in the case of spray-coating approach where the multi-pass deposition is needed for achieving the desired thickness of perovskite absorbers. In contrast, high quality perovskite crystals with various thicknesses can be conveniently and continuously fabricated through simply increasing the flow rate, in a way similar to the additive manufacturing. For example, increasing the flow rate 26 L $min^{-1}$ readily gives rise to the highest achievable thickness of 1130 nm. All samples made of different thicknesses display comparable photoresponses, as PCE remains competitive over the full spectral range (>11%). They display a decrease in $J_{sc}$ attributed to the formation of uneven morphology as the roughness surges to 80 nm when thin film thickness exceeds 900 nm. For the EQE measurement, the spectra looks similar for different thickness, except for the region near the adsorption edges that flatten out as thickness increases. This can be attributed to the single path absorption of the thicker perovskite films. Perovskite solar cells fabricated by CLIP process also demonstrated steady state measurements for $J_{sc}$ is, which confirms the device performance parameters extracted from I–V

curves as well as demonstrating the reliability and reproducibility.

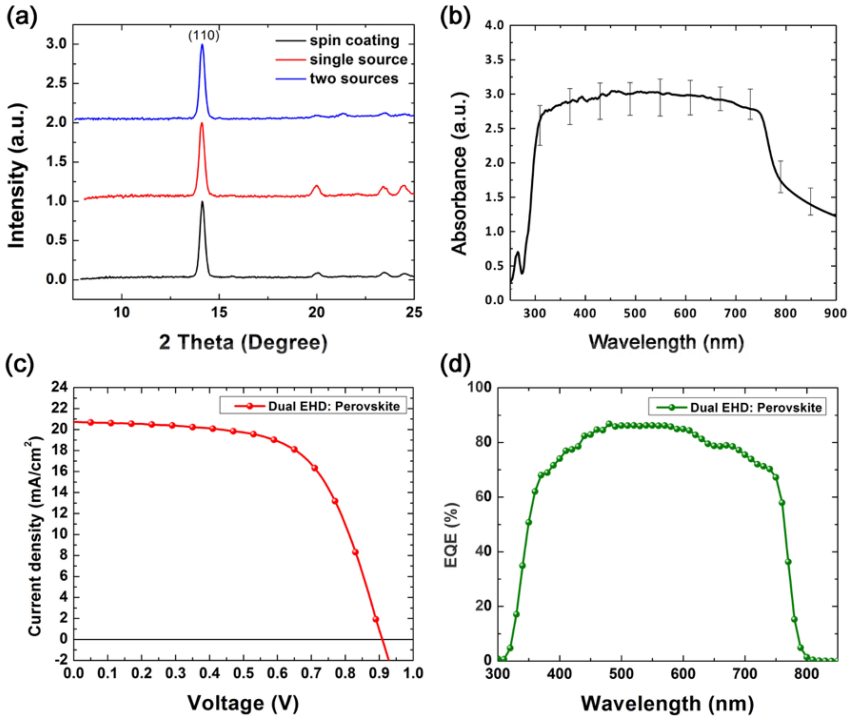


Figure 4.7: (a) XRD patterns of specimens prepared from spin-coating (black), single-sourced (red) and dual-sourced CLIP process on ITO glasses exhibit characteristic, sharp peaks of perovskites. (b) Absorption spectrum also displays a significant, broad absorption over the entire visible light range. (c) I–V characteristics in tandem with (d) EQE as a function of wavelength collectively demonstrate the comparable photoresponses when compared with the single-sourced counterpart.

These advantageous features highlight the integrity within perovskites during CLIP deposition steps. Further, I–V curves obtained in reverse (from $V_{oc}$ to $J_{sc}$) and forward directions ($J_{sc}$ to $V_{oc}$) mesh well with the bulk crystalline nature of the perovskite thin films as summarized in Figure 4.5 e. The overall PCEs% of both reverse and forward directions are 15.18 % and 14.41%, respectively, with an average of 14.79%. Note that the minor discrepancy in PCE mainly emanates from the FF of forward scan because the output characteristics such as $V_{oc}$ and $J_{sc}$ remain unchanged in both directions. Such hysteresis is a common feature on Perovskite solar cells and have been attributed to ion migration in Perovskite crystals.

To further quantify layer quality and charge extraction, we systematically explored

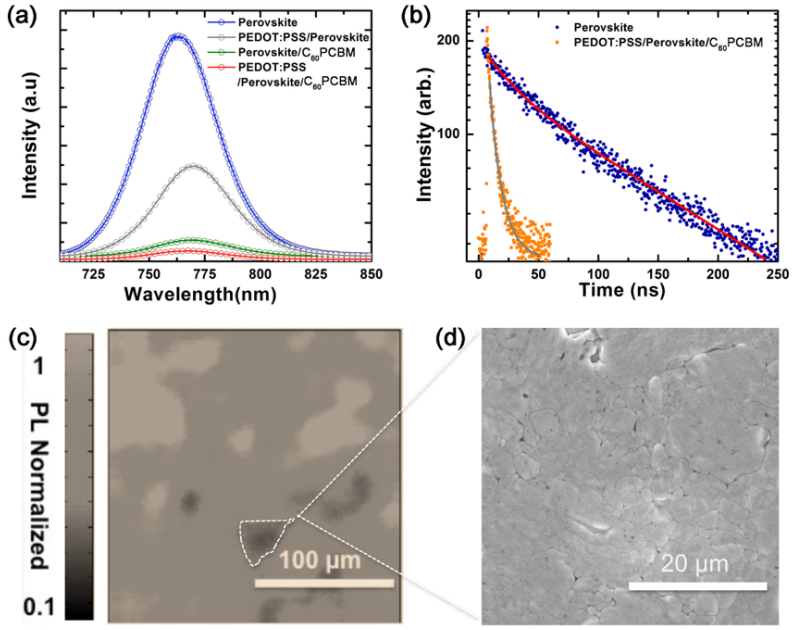


Figure 4.8: Spatially, spectrally and temporally resolved photoluminescence spectroscopy.(a) Photoluminescence of perovskite (blue), PEDOT:PSS/Perovskite (gray), Perovskite/$C_{60}$PCBM (olive), and PEDOT:PSS/Perovskite/$C_{60}$PCBM (red) shows the effective quenching when paired with transport layers. (b) Time resolved photoluminescence lifetime of the perovskite thin film on the ITO glass, and from the full device architecture. (c) Photoluminescence mapping and (d) corresponding, low magnification SEM image of a perovskite thin film spectrally interprets the spatial variation of crystalline grains over a large area (200 /*mu*m x 200 /*mu*m with 1 /*mu*m resolution).

the dynamics of photogenerated charge carriers at the interfaces and within perovskite layers. We first measured charge generation by means of photoluminescence (PL) and time-resolved photoluminescence lifetime measurements (TRPL) of thin film specimens made of $CH_3NH_3PbI_{3-x}Cl_x$, PEDOT:PSS/ $CH_3NH_3PbI_{3-x}Cl_x$ /$C_{60}$PCBM, and PEDOT:PSS/ $CH_3NH_3PbI_{3-x}Cl_x$ / $C_{60}$PCBM on ITO glass substrates, respectively. As featured in Figure 4.8 a, the expected PL quenching occurs when the perovskite thin film (blue open circle) is in contact with either PEDOT:PSS (gray open circle) or $C_{60}$PCBM layers (olive open circle). The drastically reduced PL intensity suggests the effective extraction of charge carriers at both interfaces (red open circles). In par-

allel, TRPL also yields an average lifetime of 184 ns from neat perovskite thin film specimens (Figure 4.8 b). This long lifetime can be translated to equivalently long carrier diffusion lengths that allow the use of thicker perovskite thin films for light harvesting. In particular, we observed a bimodal recombination process, an indication of large grains with good crystalline quality. PL lifetime significantly drops to 15 ns when the perovskite film is incorporated in full device architecture, originating from the rapid charge transfer at the interfaces.

Previous studies have shown that PL intensity and lifetime varied across neighboring grains in the same film.[148]Interfaces between these tightly packed grains showed a much weaker PL intensity as well as exhibiting a faster non-radiative decay. Due to the lateral dimensions of bulky perovskite grains that well extend into hundreds of micrometers, large area PL mapping (200 $\mu$m  200 $\mu$m, with 1 $\mu$m resolution) was employed to spectrally interpret the spatial uniformity within the thin film (Figure 4.8 c). While the majority of PL mapping appears to be mostly uniform along the perovskite crystalline networks, the presence of the sporadically dispersed dark regions suggests the formation of local non-radiative pathways. Figure 4.8 d presents the corresponding SEM image taken from the area of dimmer PL intensities, revealing a polygonal assembly of grains. This indicates that the smaller grains arranged in a polygon fashion may be responsible for the formation of defect states or shallow trapping levels.

One possible solution to address such shallow traps arising from the grain boundaries is through assisted thermal annealing, which vastly improves the overall crystallinity by the reconstruction of thin film morphology.[148, 149]The implementation of vacuum assisted annealing is directly compatible with in-line production, and together with the CLIP process can help in realizing a glass-in-perovskite-out inline production while preserving the competitive output characteristics.

Another drawback that has hindered the terrestrial deployment of perovskites is by the fact that Pb has been a major constituent of all highly performing perovskite photovoltaics to date, raising environmentally hazardous concerns during processing, device fabrication, deployment, and disposal. While strenuous efforts have been dedicated to exploring alternatives of Pb, relatively little is investigated to efficiently manage Pb consumption during the deposition steps.[98] Furthermore, to ensure both desired morphology and optimized coverage, excessive perovskite precursors are needed in the conventional spin-casting process. For example, nearly 100 $\mu$L of perovskite precursors (containing 2.64 M MAI and 0.88 M $PbCl_2$) are typically used in each spincasting cycle that accounts for 18.40 mg of Pb usage; however, more than 70% of the solution was wasted in order to generate thin films with desired morphology

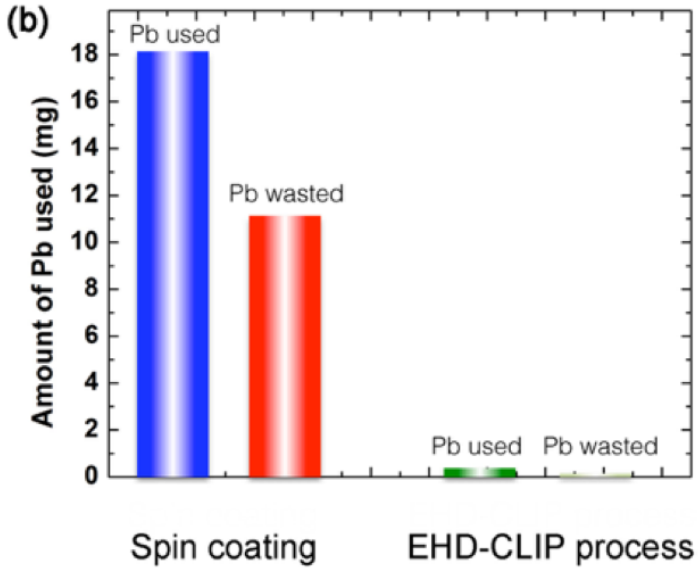


Figure 4.9: (Comparison of lead used in EHD-CLIP process and conventionally used spin coating technique)

over the entire substrates (typically set at 3000 rpm to deliver perovskite thin film thickness of 500 nm over a 1.5 cm  1.5 cm substrate). The consumption of Pb will be further pushed into an exponential model when the scale of production becomes progressively close to an industrial standard, making it less competitive to the silicon based photovoltaics. In contrast, CLIP process requires only 1.70 $\mu$L of perovskite precursor solutions with same concentrations to generate a fully covered, continuous thin film with a comparable thickness of 525 nm (5 kV $cm^{-1}$ , flow rate 18 $\mu$L $min^{-1}$ , and stage speed of 3.2 $mms^{-1}$). This significant reduction of Pb during the fabrication process occurs because over 90% of the precursor droplets are effectively used to constitute the active layers. This can be translated into that only $\sim$ 0.31 mg of Pb in total will be needed in each spray cycle, a two orders of magnitude of reduction compared to that of spin-coating counterpart as summarized in Figure 4.9 . The substantial reduction of Pb consumption during deposition thus diminishes the negative impact of Pb in large-scale production of perovskite-based photovoltaics, representing a significant step closer to meet the legislative regulations.

## 4.4 Conclusion

In conclusion, inspired from the Marangoni flow seen in nature, we developed an efficient deposition technique for the fabrication of highly uniform Perovskite thin films with enhanced coverage and grain size. By the virtue of marangoni flow which originated from the vapor pressure gradient in a binary solvent system, the PVSK precursor-containing droplets undergo a continuous process of coalescence, merging and spreading that leads to a continuous thin film morphology without the needs for post-deposition engineering. These advantageous features collectively drive the average PCE over 16%, representing 1.5 times higher than that of conventional spray-pyrolysis process. Given the relatively simple device architecture, we envision that the PCE can be further improved through the use of more efficient charge extraction layers. Meanwhile, marangoni-assisted deposition demonstrated here alleviates the impacts of excessive consumption of Pb during fabrication through effective management. With the rapid advancement in compositional engineering and morphological tailoring, highly efficient PVSK photovoltaics with limited environmental impact can be envisioned through this massively parallel nanomanufacturing route, we have developed.[125, 135]

## 4.5 Experimental characterization

### Solar Cell Fabrication

Prior to EHD spraying, ITO/PEDOT:PSS substrates were again treated with UV-ozone for 40 s to remove organic contaminates as well as improving the wettability. Next, the $CH_3NH_3PbI_{3-x}Cl_x$ precursor solution was EHD sprayed. The distance between the spinneret tip (gauge 23 TW) and the ground (copper plate) was carefully kept at 2.5 cm. An external electric field of 12.5 kV was applied to ensure the generation of a multi-jet mode. The dynamics of EHD spraying were closely monitored through a high-speed camera (Phantom). The substrate temperature was kept at 35 $^o$C to avoid the unwanted coffee ring effect. Flow rate was set at 18 $\mu$L min$^{-1}$ while the moving speed of the linear motor stage (Newport, ILS 100LM) was programmed at 3.2 mms$^{-1}$ . Note that humidity of the fume hood was closely monitored to keep at below 20%. The resulting substrates were immediately transferred to a glass petri dish for 15 min prior to thermal annealing. Alternatively, spraying coating samples were made using the analogous conditions except for the pre-annealing of the substrate at 75 $^o$C, emulating the spray-induced de-wetting process. All coating processes were completed inside the fume hood. Upon completion of EHD cycles, perovskite thin films were immediately transferred into a petri dish to further initiate reorganization and optimization process.

Finally, highly crystallized perovskite thin films were obtained through a hot air assisted annealing process (Heat gun, Master ProHeat 1100 Dualtemp) at 110 $^{o}$C for 6 min. Specifically, the directional flow of hot air constantly creates turbulence at the airperovskite liquid interfaces. Volatile MACl byproducts can thus be effectively removed through thermal annealing, thus leaving the room for rapid crystallization of perovskites. To ensure the surface uniformity, the distance between the heat gun and substrates was carefully kept at 21 cm. During the annealing process, samples were iteratively oscillated at a frequency of 5 mms$^{-1}$ . 20 mgmL$^{-1}$ of $C_{60}$PCBM (Nano–C) was dissolved in dichlorobenzene solution and filtered before spin-coating onto the perovskite layer at 3000 rpm, followed by thermal annealing at 100 $^{o}$C for an hour. To complete the photovoltaic cell, 30 nm of $C_{60}$ and 70 nm of Al were thermally evaporated through a shadow mask. The device area was determined to be 0.13 cm$^2$ . I-V characteristics of photovoltaic cells were taken using a Keithley 2400 source measurement unit under a simulated AM1.5G spectrum. Light intensity was calibrated by a KG-5 silicon diode. EQE spectra were taken using a QE–5 measurement system (Enli Tech., Taiwan).

### Characterizations

The morphological and topological information of CLIP generated perovskite thin films were obtained using a combination of FESEM (Zeiss, ULTRA–55) integrated with an energy dispersive X-ray spectroscopy, AFM (Multimode, DI), and optical microscopy (Leica, DM-2500). Thickness of perovskite thin films was determined through cross-sectional SEM images. The XRD characterizations were collected using a Bruker AXS D8 Discover GADDS X-ray diffractometer (Cu K$\alpha$ radiation, $\lambda$ = 1.54059 $\mathring{A}$). A pulsed supercontinuum source (NTK Photonics) at 690 nm wavelength with 1.2 mWcm$^{-2}$ power was used for optical measurements. The PL measurements were done using an Action 150i spectrometer, which disperses the signal onto a thermoelectrically cooled CCD. For time-resolved PL measurement, a 690 nm pulsed light source was used at a Rep rate of 3.9 MHz.

## 4.6 Acknowledgements

The work was done in collaboration with Prof. Vincent Tung, Dr. Hidetaka Ishihara and Dr. Yen-Chang Chen. Prof. Vincent Tung was a co-PI on this project along with Prof. Sayantani Ghosh. Dr. Hidetaka Ishihara helped with I-V characterization as well as sample preparation. Dr. Yen-Chang Chen assisted with various microscopy imaging. The work was funded by U.S. Department of Energy under Contract No.

DE-AC02-05CH11231, NASA MIRO Center under Contract No.NNX15AQ01A and National Science Foundation DMR-1056860

# Chapter 5

# Low temperature excitonic spectroscopy as a probe of quality in hybrid perovskite thin films

After achieving $\sim$ 16% efficiency in PSCs synthesized from electrohydrodynamic spraying, we used low temperature optical spectroscopic techniques to investigate the physical properties of PSCs and its correlation to different crystal phases. A framework for using temperature dependent static and dynamic photoluminescence (PL) studies to probe lattice defects in thin films is expected to be developed.

We report that the room temperature tetragonal phase (T $\geq$ 120 K) of perovskite thin films exhibit bi-exponential recombination from free charge carriers, with an average PL lifetime  200 ns. Below 120 K, the emergence of the orthorhombic phase is accompanied by a reduction in lifetimes by an order of magnitude, which we establish to be the result of a crossover from free carrier to exciton-dominated radiative recombination. Analysis of the PL as a function of excitation power at different temperatures provides direct evidence that the exciton binding energy is different in the two phases, and using these results, we present a theoretical approach to estimate this variable binding energy. Probing inherent fundamental properties of hybrid perovskite semiconductors is an important tool to understand the full potential as well as limitations of perovskite devices.

## 5.1 Introduction

Organic-inorganic perovskite (PVSK) materials began their foray into the field of photovoltaics (PVs) as sensitizers in solar cells[7], but have since transitioned to the primary role of active material in a new generation of hybrid PVs. Perovskite

solar cells (PSCs) have demonstrated impressive power conversion efficiencies, routinely ranging between 15  22%[17, 129, 150] This results from perovskites possessing a unique combination of properties: high mobility[151–153] and charge carrier lifetimes[123, 152] of inorganic semiconductors[154], but the flexibility and ease of fabrication of organic materials[15, 124, 155, 156]. Researchers in the field are actively engaged in optimizing PV performance enhancement, and in the span of just a couple of years significant progress has been made, including growth of large high-quality single crystals with micron-scale carrier diffusion lengths[37, 123] , improved stability in thin film samples and faster sample preparation techniques[157]. Compared to the effort invested in the PV aspect of perovskite materials, there have been fewer investigations in the study of the fundamental properties of hybrid PSCs. The characteristics that make PVSKs ideal for energy harvesting applications also make them well suited in the fields of opto-electronics[158], particularly for high efficiency lasers[159] and broadband photo detectors[160]. Recent magneto-optical studies have demonstrated magnetic-field induced state mixing, opening up an entirely new set of possibilities regarding the use of PVSKs in spin-based quantum information platforms[161]. Given the range of possible uses, understanding the fundamentals of charge generation, transport and recombination is essential for not only developing high-efficiency PVs, but also to fully harness the capabilities of hybrid PVSKs for applications in a broader applied context.

Spectroscopic techniques have been key in most of the recent studies that have provided critical insights into the PVSK phase space. This includes a structural phase transition from tetragonal to orthorhombic[162, 163], where the transition temperature depends on the halide composition and concentration[148, 164]. For $CH_3NH_3PbI_{3-x}Cl_x$ this typically occurs in the range 140–120 K. Optical spectroscopy has shown that the photoluminescence (PL) of the tetragonal phase red-shifts with decreasing temperature, resulting in a positive thermal coefficient, contrary to what is observed in the majority of semiconductors[162, 164]. This emission is homogeneously broadened18, and has long recombination times on the order of hundreds of nanoseconds[148, 165]. The onset of the orthorhombic structure at low temperatures results in a sharp increase of the recombination rate and carrier lifetimes drop to tens of nanoseconds[163]. The mechanism behind this abrupt and sudden change has proven difficult to pin down. Another aspect where both anomalies and possible answers were highlighted by spectroscopic measurements is with regards to the excitonic binding energy ($E_B$). It is typically evaluated to be anywhere in the range 30–100 meV from PL and photo-absorption data, an indication that a considerable fraction of excitons must be present at room temperature (an equivalent of 25 meV). But experiments have shown that room temperature PL is dominated by free charge carriers[166]. Magneto-absorption measurements have shown empirical evidence that $E_B$

is temperature dependent, decreasing to 6 meV by 300 K[167]. This has been posited as a reason why hybrid PVSKs are unstable under ambient conditions, a subject at the very root of the biggest hindrance to their commercial viability. The value of a thorough investigation of the PVSK phase space is therefore not limited to pedagogical interests, but essential for critical insights into fundamental properties that will allow rational design and fabrication to extract the best performances. We focus on static and dynamic PL spectroscopy of hybrid halide organic PVSK fabricated using a high throughput and potentially scalable continuous liquid interface propagation (CLIP) technique[13, 168] that has produced uniform thin films and demonstrated improved sample stability, often extending to weeks under ambient conditions.

Using extensive temperature-dependent static and time-resolved spectroscopy, we have addressed several unresolved issues. First, we have systemically quantified the carrier recombination with temperature in the region $< 140$ K. These measurements show that charge lifetimes decrease with decreasing temperature, unusual for semiconductors, but indicative of radiative excitonic recombination. Next, by monitoring photoluminescent emission as a function of excitation power, we have demonstrated that the sudden increase in recombination rates accompanying the phase transition is related to the nature of the dominant charge carriers, which switches over from free elections and holes to excitons. Additionally, we have developed a theoretical approach that allows estimating the exciton binding energy directly from spectroscopic data. And finally, we have established a simple and direct technique to gauge PVSK film quality, a finding that will be of significant use in device design and development.

## 5.2 Experimental methods

PVSK was synthesized using the electrohyrdodynamic fabrication technique described in chapter 3. Scanning electron microscope (SEM) images of the sample [figure 5.1a andb] show both the uniformity and large crystal grains on the order of almost 10 m. Specifically, the cross-sectional SEM image [figure 5.1(c)], reveals a continuous, single-slab like grain in the out-of-plane direction. For optical measurements we use two excitation sources: a pulsed supercontinuum source (NKT Photonics) and a continuous wave diode laser tuned to 532 nm (Coherent Inc.) The PL data are taken using an Acton 300i spectrometer and then dispersed onto a thermoelectrically cooled charge-coupled device with a spectral resolution of 0.18 nm. For the time-resolved measurements we use a time-correlated single photon counting (TCSPC) system (Picoquant) in conjunction with the supercontinuum source that allows us to vary the repetition rate. The temperature dependent measurements are done in a cryo-free system from Advanced Research Systems with a base temperature of 10 K.

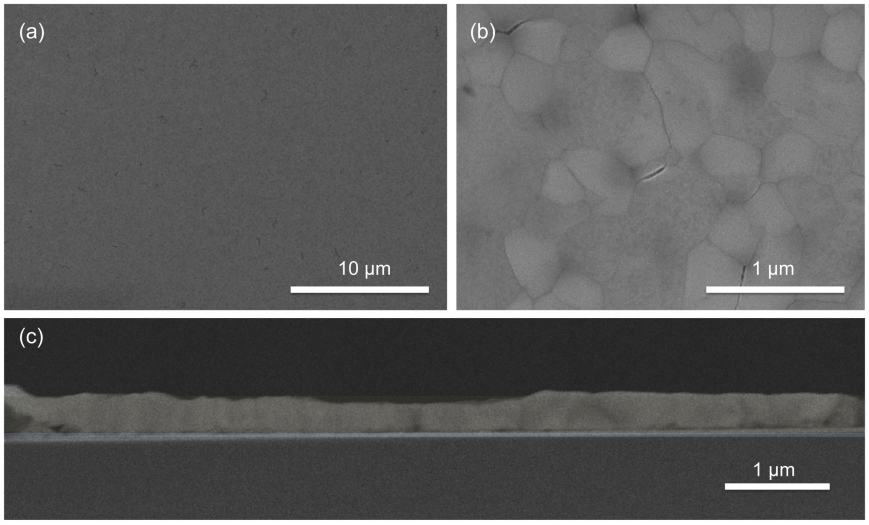


Figure 5.1: SEM image of CLIP fabricated perovskite thin films shows (a) high coverage and (b) unique morphology comprising a hybrid of perovskite networks and grains. Of particular importance is the single-slab like out-of-plane grain that can effectively bridge the extraction layers of opposite polarities.

## 5.3 Results and discussion

The results of optical characterization of the tetragonal structure above the phase transition (T $\geq$ 120 K) are summarized in figure 5.2. At room temperature, the emission is centred on 1.6 eV. As T is lowered, the emission spectrum narrows and red-shifts [figure 5.2(a)]. Fitting the spectrally integrated PL intensity ($I_{PL}$) with temperature using $I_{PL}(T) = I_0[1 + Ae^{(-E_b/k_BT)}]$ allows us to extract $E_B = 105 \pm 3$ meV [figure 5.2(b)]. However, it has been suggested that this approach of predicting $E_B$ is inaccurate, as emission at different temperatures has contributions from varying proportion of excitons and free charge carriers[166]. The rate of change of exciton and free charge carrier concentration can be explicitly written as:

$$\frac{\partial n}{\partial t} = -(1-\gamma)Rnp - Rnp + K_dX \tag{5.1}$$

$$\frac{\partial p}{\partial t} = -(1-\gamma)Rnp - Rnp + K_dX \tag{5.2}$$

$$\frac{\partial X}{\partial t} = -K_dX - K_rX + G + Rnp - R_{nr} \tag{5.3}$$

where n, p and X are the electron, hole and exciton concentrations respectively, R the recombination rate of electrons and holes, $\gamma$ the proportion of electrons and holes recombining to form excitons, $K_d$ the exciton dissociation rate, G the exciton generation rate, and $K_r$ and $R_{nr}$ the rates of radiative and non-radiative exciton recombination. At the excitation powers used the non-radiative sites are saturated, and hence the non-radiative rate may be considered to be constant. Generation of free charge carriers is solely attributed to exciton dissociation. Charge trapping is not considered a contributing factor, as the extent of any unintentional doping is negligible compared to the photo-excited carrier concentration ($\sim 10^{15}$ cm$^{-3}$). Nor are exciton-exciton interactions, as they are noticeable only at a high free carrier concentration ($>10^{21}$ cm$^{-3}$). Under continuously pulsed illumination it is safe to assume all the generated charge carriers recombine and the dissociation of excitons to holes and electrons to be in dynamic equilibrium. Since the electron-hole recombination ($R_{np}$) is proportional to the photo-generated densities of the electrons and holes and the exciton radiative recombination ($K_r$X) is proportional to the exciton concentration, we get

$$I_{PL} \sim Ax^2[N_{tot}]^2 + B(1-x-k)N_{tot} \tag{5.4}$$

where $I_{pl}$ is the spectrally integrated emission and x the fraction of free carriers and A and B are mono and bimolecular recombination rates. (1–x–k) is the fraction of excitons that undergo radiative recombination, where k is the fractional population that contributes to non-radiative recombination[158, 169]. Ntot is the total charge carrier concentration, which in turn is linearly proportional to the excitation power P. Thus, the contribution of the free carrier recombination to the emission leads to $I_{PL} \sim P^2$, while the corresponding contribution from exciton recombination will show up as $I_{PL} \sim P$. Therefore, we can estimate the relative fraction of free carriers and excitons by fitting a second order polynomial to data as shown in figure 5.2(c). The square root of the quadratic part represents the fraction of electrons/holes and the linear part corresponds to the fraction of excitons undergoing radiative recombination. Using this method, we can accurately estimate the fraction of excitons, utlizing the internal quantum efficiency spectra of these films[158, 169]. For example, a clear quadratic dependence of the data at 294 K as shown in figure 5.2(c) suggests that the emission is a result of recombination of mostly free carriers and not excitons, though there might still be excitons undergoing non-radiative recombination.

We begin our investigation into the low temperature phase space by studying PL at the initiation of the structural transition from tetragonal to orthorhombic phase and map the spectra as functions of emission energy and temperature in figure 5.3(a).

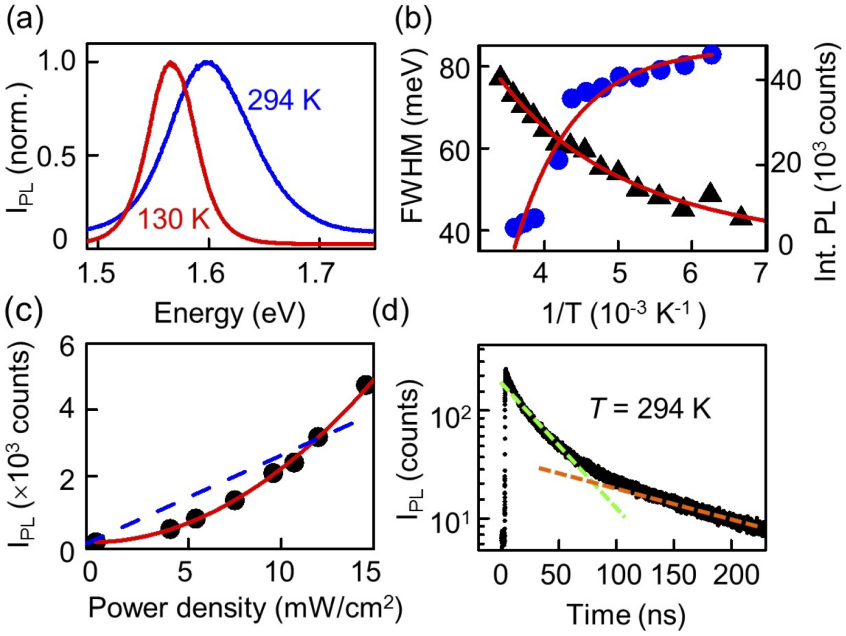


Figure 5.2: Temperature dependent emission of tetragonal phase (a). (b) Peak full-width at half maxima (FWHM, triangles) and spectrally integrated emission intensity (circles) varying with temperature T. The fits are discussed in the text. (c) Spectrally-integrated PL at 294 K as a function of excitation power density. The lines compare linear (dashed) and quadratic (solid) fits to the data. (d) Time-resolved emission on a semi-log scale showing two distinct lifetimes in the tetragonal phase.

Unlike the behaviour at T > 120 K, the tetragonal emission (centred on 1.59 eV at 120 K) now blue-shifts and broadens considerably between 120–100 K. By 90 K it merges with an emerging low energy side-band, while the orthorhombic peak (1.65 eV) dominates the spectral signature. On lowering temperature further, the orthorhombic peak is clearly visible and the spectral region enclosed by the dashed box still shows a weak emission from the tetragonal phase. The relative novelty of hybrid PVSKs mean that the energy states of these systems are not definitively understood yet. Using this PL data we have summarized our results to sketch an energy level diagram in figure 5.4(b). The persistence of the tetragonal phase at low T is supported by absorption data [166]. For a quantitative analysis, we fit the emission over the entire energy range using three Gaussian distributions (see figure 5.4 a), centred about the emission energies designated P1 – P3 at 120 K, which means these are not fixed peak

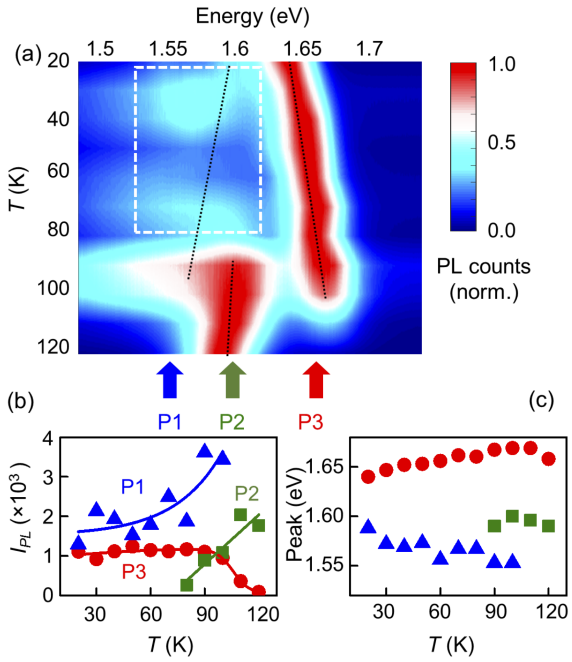


Figure 5.3: (a) PL intensity mapped with emission energy and temperature. Arrows highlight spectral positions of peaks under investigation for T < 120 K , dashed lines shows the position of peaks (b) Spectrally integrated PL and (c) centre wavelength of the peaks shown in part (a) varying with temperature

positions, but rather, identify the starting points. The integrated emission intensity and peak position of each of these are plotted with T in figure 5.3(b) and (c), respectively.

The data for P3 in figure 5.3(b) shows that after the phase transition progresses to completion at T = 90 K, the spectral weight associated with this peak is unchanged down to 10 K, while its spectral position in figure 5.3(c) shows a minor red-shift with decreasing T. The results of the analysis of P1 and P2 are more complex and illuminating. P2 centres on the tetragonal emission and its spectral weight decreases steadily, disappearing by T $\sim$ 80 K in figure 5.3(b). Its peak position in figure 5.3(c) shows no discernible variation between 120 K and 80 K. The demise of P2 is accompanied by the emergence of a broad sideband, labelled P1, at T = 100 K, but this too quenches with decreasing temperature, as seen in figure 5.3(b). Its peak positions in figure 5.3(c), however, show that while the sideband emerges separate from the tetragonal peak at first, for T < 90 K it is likely that P1 is a contribution from

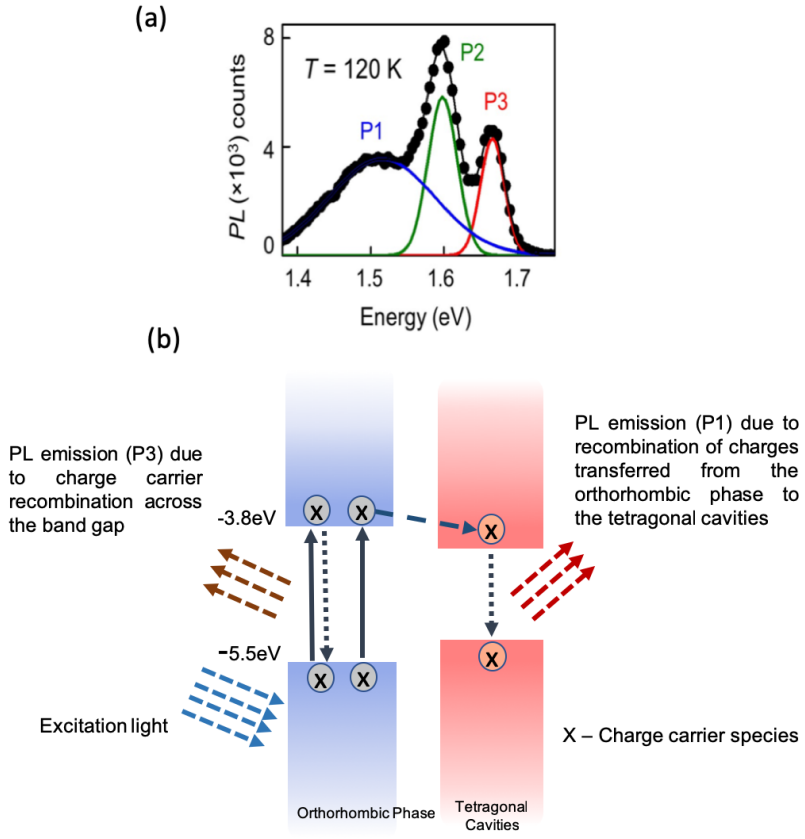


Figure 5.4: (a) PL spectrum at the cusp of the phase transition showing multi peak fits with peak designations. The black curve is the cumulative fitted peak. ($R^2$ =0.99). (b) Schematic showing charge carrier recombination and energy transfer process between orthorhombic phase and tetragonal cavities leading to band P2 and side band P1 in low temperature PL of Perovskite films. P3 peak not shown in schematic arise due to direct band gap recombination in the low temperature orthorhombic phase.

remnants of the tetragonal phase after all.

The most striking spectroscopic change that accompanies the structural transition is in the PL recombination rates across the entire spectral range. The time-resolved PL at T = 294 K [figure 5.2(d), 5.5] shows a bi-exponential decay with long and short lifetimes of 186 and 24ns respectively, corresponding to an average recombination lifetime of 169 ± 2.4 ns, and this persists till T = 130 K (figure 5.6). At T

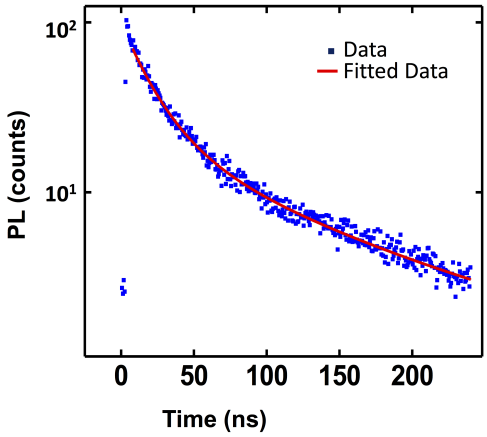


Figure 5.5: Time-resolved emission on a semi-log scale showing two distinct lifetimes at 294 K ($R^2 = 0.989$)

= 120 K the recombination lifetime drops abruptly and drastically by an order of magnitude, a result that has been previously observed but not studied systematically or in-depth, and consequently, not fully investigated. One proposition is an energy transfer process where the carriers of the high-energy orthorhombic phase may diffuse to the small inclusions of the persisting tetragonal phase that provide a low energy channel for recombination[160]. The co-existence of two phases has been observed in a number of systems before and the smaller inclusions are stabilized due to the strain or pressure developed within the films[130, 170].

These inclusions could be a result of pressure stabilised inclusions or lattice defects in the high temperature phase that induces spontaneous plane shifts during phase transition in the films, and can have major effects on the film conductivity and other photovoltaic properties[130, 170]. Due to extensive scattering at these lattice or grain boundaries originating from randomly oriented lattices, there will be increased resistance and lowered mobility of charge carriers[171]. These locations have also been observed as electron trapping sites in magnesium oxide (MgO) films and hence minimizing these grain boundaries or defect states is of paramount importance to enhance film quality[172]. In figure 5.6 we highlight our results of spectrally-resolved time-resolved PL in the range 120–10 K. figure 5.6(a) maps the PL as a function of time and temperature, with the 0 on the time axis demarcating the arrival of the excitation pulse for emission peak P3, which we can tie to PL from just the orthorhombic phase. Figure 5.6(b) shows the corresponding data for emission from the low energy states which is peak P2 for temperatures between 120 K and 100 K, and P1 for T <

100 K. The insets in both these figures show representative time-resolved PL traces at 80 and 50 K.

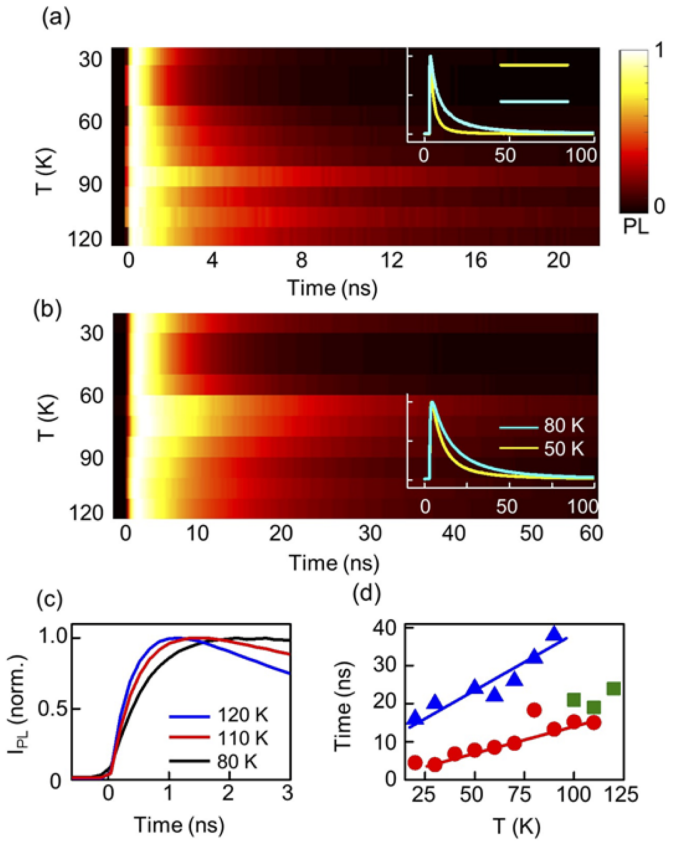


Figure 5.6: Time-resolved PL data mapped with temperature and time for (a) high energy peak, P3 and (b) low energy states (P1 and P2). (insets) Sample time traces. (c) Initial rise of time-resolved PL for low energy states at different temperatures (d) Recombination lifetimes extracted from exponential fits to data in (a) and (b) with symbols corresponding to peaks in figure 5.4(b). Fit errors are 0.17 ns for (a) and 0.015 ns for (b).

Comparing the two data sets, the most noticeable observation is how much faster the recombination at the orthorhombic site is than that from the lower energy states associated with the tetragonal phase. This gives credence to the hypothesis that there

is energy transfer from the high to low energy sites. Figure 5.6(c) shows the first 3 ns following the arrival of the excitation pulse for the low energy states. The observed initial rise, which slows with decreasing T, is a charging time denoting signal build-up as carriers arrive from the high energy state, providing further confirmation. In cases of such incoherent energy transfer, the recombination times of the high energy states is reduced from its normal value as carriers migrate to the low energy sites and recombine there instead. This is observed very clearly in ensembles of semiconducting quantum dots[173], and the result is a monotonic increase of recombination times as the emission energy decreases. However, the longest lifetime observed at the lowest energies is never longer than the native unaltered lifetime of the system. Therefore, while there is definitely some aspect of energy transfer between the close-lying low temperature states in the hybrid PVSKs, there could also be variations in intrinsic charge carrier dynamics of the films due to the presence of high temperature nanoscale domains that could further lead to the faster recombination. It does not explain at all why the recombination from the remnants of the tetragonal phase should have such a highly reduced lifetime as well. Studying the change in optical properties and charge carrier dynamics will be an effective tool to characterize these lattice defects and will be a check for film quality. As figure 5.6(d) demonstrates, the recombination times show further variations with decreasing temperature. The orthorhombic emission decays faster as T decreases. And for T $<$ 100 K, the low energy PL shows an even steeper reduction. This decrease of lifetimes as T is lowered, while unusual in direct band-gap semiconductors where reduced phonon coupling to photo-generated carriers increases charge lifetimes, is an indication of the emission PL being dominated by radiative excitonic recombination.

In an effort to explain these changes in carrier dynamics, we focus on the type of the carriers that lead to recombination at different temperatures. In figure 5.7(a) we plot the variation of $I_{PL}$ with P at different temperatures, fit the data with a second order polynomial and compare the linear and quadratic coefficients of these fits in figure 5.7 4(b). As expected, at T = 294 K the quadratic component is responsible for almost the entire weight, confirming that radiative recombination is driven entirely by free carriers and the exciton fraction solely comes from the nonradiative part. However, at 200 K there is linear component that accounts for almost 25% of the total weight, implying the radiative recombination of both free carriers and excitons, with the majority still being the former. By 80 K the majority component in $I_{PL}$ is linear, accounting for 60% of the total weight. Based on this monotonic change with T we conclude that there is a crossover from free carriers to exciton-dominated radiative recombination, and in figure 5.7(c) the calculated free charge carriers using the Saha-Langmuir equation is plotted for an exciton binding energy of 100 meV. The Saha-Langmuir equation[174, 175], derived in the context of ionization of gases,

provides a relationship between this fraction x and temperature T for a constant ionization energy, which in this case is $E_B$. The calculated x with T for $E_b = 100$ meV and electron carrier density n = $10^{15}$ cm$^{-3}$ (squares) underestimates the crossover T considerably. Our experimental parameters indicate a carrier density in the range $10^{15} - 10^{16}$ cm$^{-3}$, but we re-calculate by increasing the free carrier concentration to n = $10^{18}$ cm$^{-3}$ (triangles), which moves the crossover T higher, but does not replicate the experimental fractions of charge carriers. In fact, there exists no reasonable combination of $E_B$ and n that can mimic the experimental x. We therefore consider more closely the statistical mechanics underlying the dissociation of the excitons into electron-hole pairs.

The equilibrium constant for this reaction $exc \Leftrightarrow e+h$ is given by $K = (N_e N_h)/N_{exc}$. The corresponding free energy $\Delta$G is:

$$\Delta G = -k_B T ln K = -k_B T ln[\frac{x^2}{(1-x)N_{tot}}] \tag{5.5}$$

where Ntot is the total number of all carriers (free electron/holes and excitons). Rearranging, we arrive at:

$$ln[\frac{x^2}{(1-x)}] = \frac{-\Delta G}{k_B T} - ln N_{tot} \tag{5.6}$$

This is the form of a standard Van't Hoff plot[176] , and is shown in figure 5.7(d), where we plot ln[K] as a function of 1/T . In order to calculate the total exciton concentration (1–x), we will need to find the fraction undergoing non-radiative recombination, From the IQE spectra reported by our group[13, 168], we can estimate it to be 0.2 in the 500-680 nm wavelength range. This value is a constant and does not vary with temperature as all the recombination sites are occupied. The slope of this plot yields the change in free energy, –$\Delta$G, and therefore, leads us to the following conclusions: (a) the slope is negative, implying the change in free energy is positive, i.e., energy is needed to dissociate excitons, an expected result; and (b) the slope changes with T, and has a larger negative value in the low temperature phase compared to the high temperature phase, indicated by dotted lines in 5.7(d), which clearly shows that the binding energy is different in the two temperature regimes. We now use this measured free energy to calculate the exciton binding energy as follows:

$$\Delta G = -k_b T ln[\frac{(Z_e Z_h)}{(Z_{exc})}] = -k_b T ln[e^{(-E_b/K_b T)} \frac{(Z_e^* Z_h^*)}{(Z_{exc}^*)}] \tag{5.7}$$

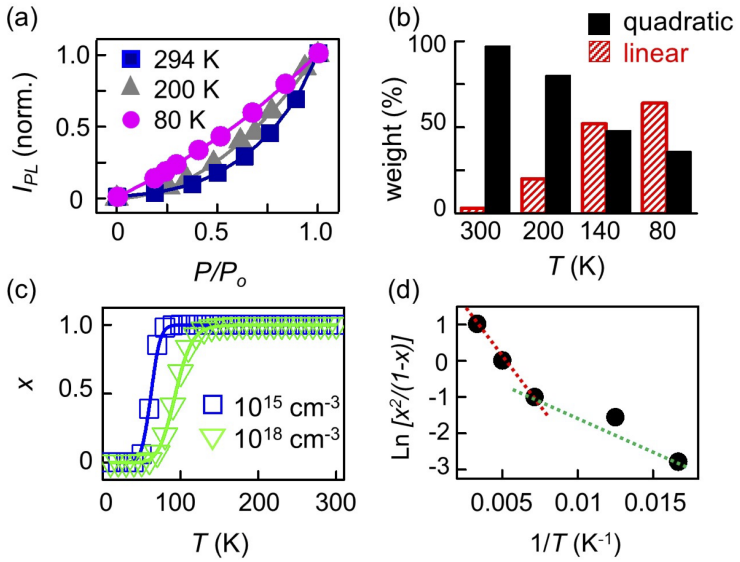


Figure 5.7: (a) Integrated PL counts varying with excitation power at T = 294, 200 and 80 K for the peak designated P2 in figure 5.4(a). Lines are polynomial fits ($R^2$ value=0.99). (b) The relative weight of the linear (shaded) and quadratic (solid) components derived from the fits in (a). (c) Calculated fraction of free carriers as a function of T for $E_B$ = 100 meV, n =$10^{18}$ cm$^{-3}$ n =$10^{15}$ cm$^{-3}$ (d) Calculating exciton binding energy varying with T using Vant Hoff plot. ($R^2$= coefficient of determination)

and

$$\Delta G = E_b - k_b T ln[\frac{(Z_e^* Z_h^*)}{(Z_{exc}^*)} \tag{5.8}$$

where * denotes the translational partition functions. For an ideal gas $\frac{(Z_e^* Z_h^*)}{(Z_{exc}^*)} = ((2\pi m^* k_b T)/h^2)^{3/2} V$, and $m^* = (m_e m_h)/m_{exc}$ and we use a numerical value of 0.1m$_e$. Combining the above equations while keeping $E_b$ constant, yields the Saha equation. The calculated $E_b$ for the high temperature phase had an average value of 95 meV and the low temperature phase had a value of 45 meV. The reason for the change in binding energy could be due to band bending at the domain boundaries, and hence the change could be a convenient indicator of these domains, which indirectly helps us determine the amount of lattice defects in the films.

## 5.4 Conclusion

Hybrid PVSKs show great promise for a variety of applications, making it imperative that we invest in understanding their fundamental properties. We have used low temperature spectroscopy to study the phase space of $CH_3NH_3PbI_{3-x}Cl_x$ and our results demonstrate that the notable spectral and dynamic changes that accompany the structural phase transition occur due to the presence of domains in the low temperature phase. These low temperature domains can be an effective way to characterize lattice defects in the high temperature film. We use the variation of spectrally integrated PL with excitation power to estimate the proportion of each carrier type at different temperatures and apply fundamental statistical physics principles to calculate $E_b$ from these data. We calculated the average $E_b$ values in the two temperature regimes and found the high temperature value (95 meV) to be very close to the numerical value of 105 meV derived from fit to temperature dependent PL data. This leads us to conclude that the typical approach to measure $E_b$ gives us an average value, while evaluating the PL at specific temperatures over a range of excitation powers offers a more accurate result. This change in binding energy indirectly lets us estimate film defects in the high temperature phase and can be an effective check of film quality. We have also developed a direct method to estimate the binding energy of excitons in hybrid PVSKs. Our approach provides a route towards checking film for lattice defects and ensuring the high quality necessary for superior performance and will assist greatly in ongoing materials engineering efforts to minimize defects and electron trapping sites, therefore making application of PVSKs photovoltaics a reality.

## 5.5 Acknowledgements

The work was done in collaboration with Prof. Ajay Gopinathan, Prof. Vincent Tung, Dr. Hidetaka Ishihara and Dr. Yen-Chang Chen. Prof. Gopinathan assisted with the theoretical analysis concerning free charge carrier to exciton cross over in perovskite semiconductors at low temperatures. Prof. Tung, Dr. Ishihara and Dr. Chen helped with the sample preparation. The work was funded by NASA MIRO Center under Contract No.NNX15AQ01A and National Science Foundation DMR-1056860 and ECC-1227034

# Chapter 6

# Stabilization of cubic crystalline phase in hybrid perovskite quantum dots via surface energy manipulation

As described in chapter 5, low temperatures partial phase transitions in perovskite thin films result in reduction in PSC performance. Preventing such phase transitions will be pivotal for the realization of low temperature perovskite devices. On this account, we investigate perovskite quantum dots instead of thin films, as they provide the opportunity to stabilize perovskite semiconductor crystals at low temperatures utilizing surface passivation techniques. Surface functionalization of nanoscale materials has a significant impact on their properties given their large surface-to-volume ratio. In this work, we demonstrate the effect that different ligands have on the surface energy contribution to the phase space of organo-metallic hybrid perovskite quantum dots (PQDs). Using a framework of static and dynamic spectroscopy, we study phase transitions in $CH_3NH_3PbBr_3$ PQDs ligated with either octylaminebromide (P-OABr) or 3-aminopropyl triethoxysilane (P-APTES). Around 140 K P-OABr undergoes the expected structural phase transition from tetragonal to orthorhombic, established by the emergence of a higher energy band at 2.64 eV in the photoluminescence (PL) spectrum. This transition is not observed in P-APTES, despite cooling the samples down to 20 K. We investigate the consequences of this altered phase space using time-resolved pl, excitation power dependent PL and Raman microscopy over a range of 300-20 K, and find that the recombination rates and types of carriers involved are significantly different in the P-APTES, compared to the P-OABr. Our findings highlight how aspects of PQD phase stabilization are linked to nanoscale morphology and to surface energy manipulation of the crystal phase diagram, and these could provide critical insights into the fabrication of stable perovskite crystals.

## 6.1 Introduction

Over the past decade, organo-metal halide based perovskite materials have been extensively researched as promising candidates for photovoltaic and other opto-electronic applications, such as light emitting diodes (LEDs)[13, 17, 21, 69, 129, 168, 177]. Following the excellent performance of single crystal samples and polycrystalline thin films, research efforts have broadened to investigate perovskite nanocrystals, also referred to as perovskite quantum dots (PQDs)[80, 81, 87]. These studies have shown that, with typically high quantum yield and versatility regarding bandgap tuning within the visible spectrum, PQDs are ideal materials for use in LEDs, lasers, biomedical applications, and optical sensors[55, 178, 179]. They have demonstrated good amplified spontaneous emission (ASE) response, with thresholds as low as 220 $nJ/cm^2$, narrow spectral width, and high output intensity[180]. Aside from device applications, PQDs have also served as ideal platforms to study the aspect of chemical instability that plagues perovskites, and has hindered the widespread implementation of perovskite solar cells, despite thin films demonstrating a higher power conversion efficiency than existing silicon solar cells[181].

These many desirable properties in PQDs have not translated into the expected high performance metrics, particularly when compared to their thin films counterparts, although they have the potential to outperform them. For example, perovskite thin film based LED devices have reported external quantum efficiencies (EQEs) of 3.5% and 8.5% for infrared and green wavelengths[182], respectively, and with higher exciton binding energy, PQDs should have higher EQEs. However, the highest reported EQE is $\sim 1\%$, far less than expected, attributed to incomplete surface passivation and poor charge transport in PQD films[182]. Similarly, while hybrid perovskite thin films have demonstrated optical efficiency of $\sim 30\%$ as luminescent solar concentrators, one of the highest reported in the field, PQD based concentrators have only achieved 6%, a result of fluorescence quenching when deposited within polymer matrices, again a consequence of incompatible surface properties[183, 184].

It is well known that surfaces of nanocrystals have several charge trap states, arising either from intrinsic defects, or from differences in the local environment, when compared to the bulk, leading to accumulation of surface charges and thus driving charge carrier migration[185]. Therefore, surface passivation of PQDs using appropriate ligands is necessary to minimize surface trap-related recombination and to improve and sustain fluorescence quantum yield. There have been successful reports of capping PQDs with linear straight chain ligands such as octylamine (OA) and octylaminebromide (OABr), but these synthesis approaches have led to non-uniform structures with variation in morphologies due to the rapid delivery of monomers, resulting from minimal steric hindrance of the capping layer[81]. The use of branched ligands has

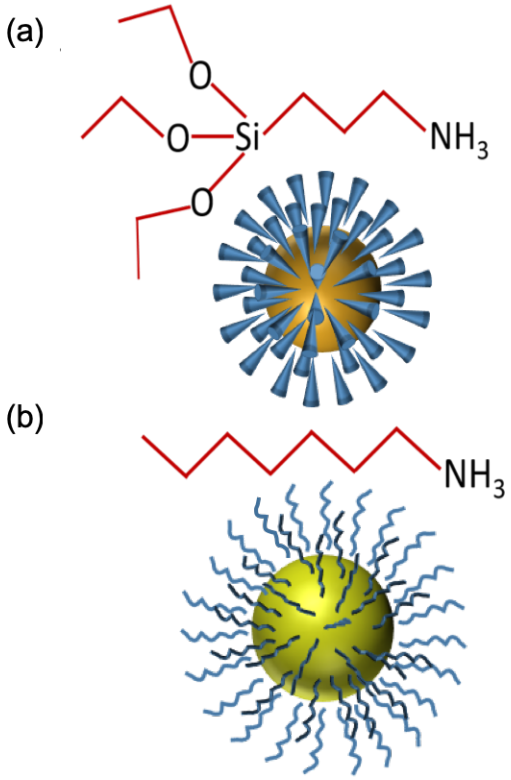


Figure 6.1: Schematics of ligand molecules and corresponding functionalized perovskite quantum dots (PQDs) with (a)APTES, designated P-APTES, and (b) OABr, referred to as P-OABr

partly resolved this issue, leading to spherical morphology with higher uniformity. Additionally, computational results have indicated that capping ligands can improve the chemical stability of PQDs, and ligand dependent variation in morphology and surface properties has been experimentally linked to PQD crystal stability[81].

Methylammonium lead bromide ($CH_3NH_3PbBr_3$) PQDs with a linear (OABr) or a branched ligand (APTES) have been synthesized using a dissolution-precipitation method[81]. Both types of dots stabilized in the crystalline $\alpha$ cubic structure at room temperature. Under ideal conditions, to maintain high cubic symmetry, the tolerance factor t of the crystal should be close to unity[10]. A deviation from this value will lead to crystal distortions and crystal structures with lower symmetry. Density functional theory calculations have shown the cubic phase to be the most unstable as it is difficult to satisfy the t = 1 condition, and hence, iodide-based perovskite thin films exist in the cubic phase only at a temperature greater than 330 $^o$C[10]. However, bromide-based perovskite crystals do exist in a pseudo-cubic phase at room

temperature, due to the difference in the ionic radii of Br- and I-, with the smaller Br- helping in stabilizing the cubic lattice[186]. Interestingly, the phase diagram is also tunable by crystal size, as evident from the fact that iodide- based PQDs exist in cubic phase at room temperature[90]. Further, in the quest for improved stability and performance of perovskite based devices, the crystal phase plays an important role. Substitution of methylammonium (MA) with formamidinium (FA) enhances chemical stability considerably, but FA-based perovskite crystals have a phase transition to the yellow non-perovskite polymorph ($\delta$ -phase) very close to photovoltaic operational temperatures, making the performance unpredictable[187]. The current route has been to adopt multi-cation synthesis, such as MA/FA or FA/Cesium (Cs), with the goal of optimizing both performance and stability, the latter focusing on arresting the phase transition[21, 188].

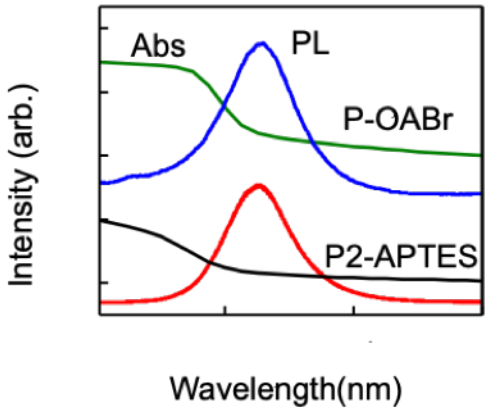


Figure 6.2: Absorption and emission spectra for P-OABr and P-APTES at room temperature

## 6.2 Results and discussion

In this work, we report phase stabilization in PQDs, manifesting as a consequence of morphological and surface ligation differences in PQDs. This results in a difference in surface energy contribution towards the enthalpy of formation of the PQDs, leading to an altered crystal phase diagram compared to the bulk and thin film counterparts. Room temperature photoluminescence (PL) spectra confirm a bandgap around 530 nm, with a spectral full width half maximum of 135 meV. However, below 150 K,

while a low wavelength peak emerges in the PL signal at 470 nm for the PQDs functionalized with OABr (termed P-OABr), no such peak is observed in the ones with APTES (termed P-APTES). This high energy peak is attributed to the low temperature transition to the orthorhombic crystal phase, typical of OMH perovskites. Unlike P-OABr, P-APTES appears to be arrested in the high temperature cubic phase with no apparent transition at temperatures as low as 20 K. We further validate phase transition in P-OABr using temperature dependent Raman scattering, with P-OABr exhibiting phonon modes below 150 K, whereas P-APTES shows no sharp features indicating the persistence of the Raman inactive cubic phase. Presence of two phases can have detrimental effects on the performance of the PQDs due to charge transfer between the two phases, loss of monochromaticity and reduction in recombination lifetime[112]. Our investigation, therefore, not only pertains to improving the optoelectronic properties of PQDs, but also has far reaching consequences for enhancing stability of perovskites in general.

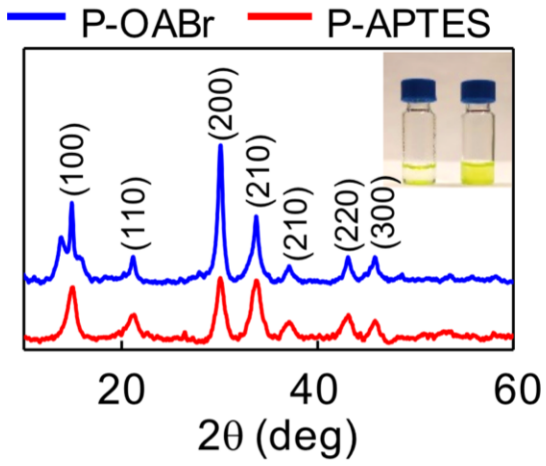


Figure 6.3: X-ray diffraction confirming cubic phase of the quantum dots at room temperature with relevant identifying peaks labelled

Schematics of the ligands OABr and APTES are shown in Figures 6.1(a) and 6.1(b), along with the functionalized PQDs, referred to as P-OABr and P-APTES, respectively, and the branched structure of APTES is represented as conical appendages on the dots surface. X-ray diffraction (XRD) patterns of P-OABr and P-APTES shown in Figure 6.3 have peak positions that confirm the cubic crystal phase of $CH_3NH_3PbBr_3$ at room temperature. Both P-OABr and P-APTES are highly dispersive (inset), remaining stable in solution for almost a week, which we attribute to the high yield of ligand passivated PQDs obtained through the dissolution-precipitation

synthesis route. Transmission electron microscope (TEM) images in Figure 6.4 show that while P-OABr has a non-uniform morphology, consisting of both particulate and sheet-like structures, P-APTES has a far more uniform distribution of almost exclusively spherical structures with an average diameter of 6.2 ± 1.5 nm. The amorphous network visible in the background is due to excess amount of APTES ligand added during synthesis to counter steric factors. An additional high-resolution image is included as an inset as further affirmation of the spherical morphology. The non-uniformity of P-OABr is typical of PQD ensembles, and follows as a result of the fast transport of monomers through the capping layer[81].

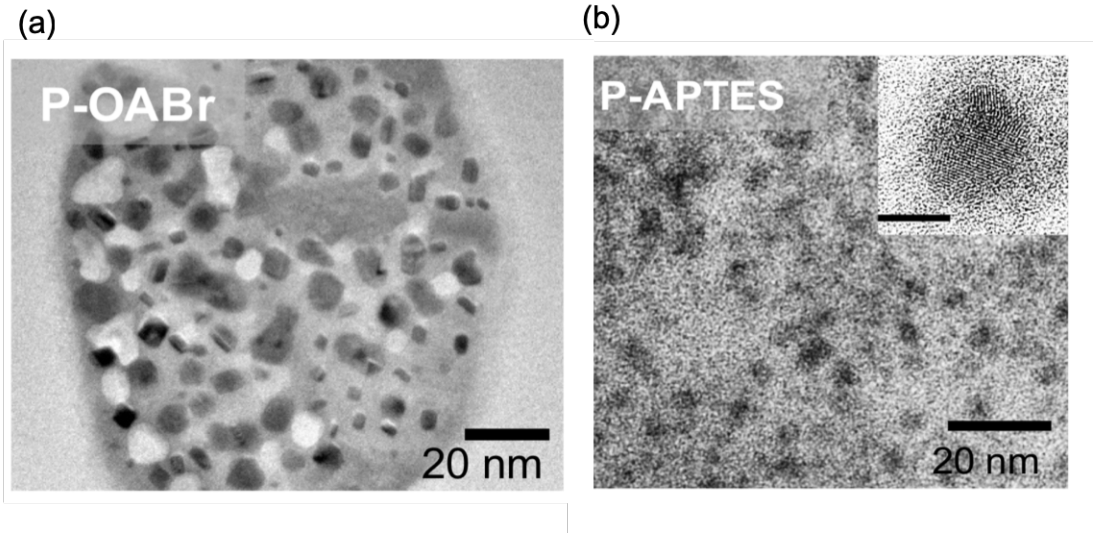


Figure 6.4: Transmission electron microscopy (TEM) images of the samples.

The higher steric hindrance offered by the branched ligands on P-APTES reduces this transport rate, facilitating uniform shape and size homogeneity. The absorption spectra in Figure 6.2 show that both PQDs have a characteristic broad spectrum with an excitonic peak centered at 520 nm. The long tails observed at longer wavelengths are due to scattering from the bigger dots in the ensemble[81]. Room temperature PL spectra of P-OABr and P-APTES in the same figure reveal Gaussian-shaped emission spectra centered at 531 nm with full width half maxima (FWHM) of 135 meV. PQDs have Bohr radii ranging between 1.2 - 4 nm, smaller in comparison to II-IV semiconductor quantum dots(CdSe, CdS), and as a result, variations in FWHM are dominated by homogeneous broadening effects[189, 190]. Consequently, a phonon energy value of 62 meV in P-OABr can be derived from the variation of FWHM with decreasing temperature as shown in Figure 6.5.

The difference in surface functionalization causes intriguing differences in the optical properties of the PQDs as well, arising from their surface energy differences, as borne out in temperature dependent PL spectroscopy. The PL emission for both P-OABr and P-APTES red-shifts with lowering temperature, contrary to conventional semiconductors, a result attributed to the reverse band ordering in perovskite crystals[10]. $CH_3NH_3PbBr_3$ transitions from the room temperature $\alpha$ cubic phase to tetragonal ($\sim$ 220 K) and orthorhombic ($\sim$ 140 K) phases, and the PL emission of P-OABr redshifts from 531 nm to 545 nm on lowering the temperature from 300 K to 150 K (figure 6.6). However, this linear shift in PL peak with temperature has an observable change of slope at 220 K, which could be an indication of the phase transition from cubic to tetragonal phase. Yet, obtaining a clear proof of a phase transition using PL measurements alone becomes difficult as the band gap is similar in the two crystal phases and hence both phases have indistinguishable emission spectra. At temperatures below 140 K, the spectrum of P-OABr has multiple emission bands, a result also observed in perovskite thin films due to the co-existence of both orthorhombic and tetragonal phases[112]. The map in Figure 6.7 (a) shows a high energy emission band at 470 nm that arises from the orthorhombic phase owing to its larger bandgap, a low energy band at 545 nm from the remnant tetragonal inclu-

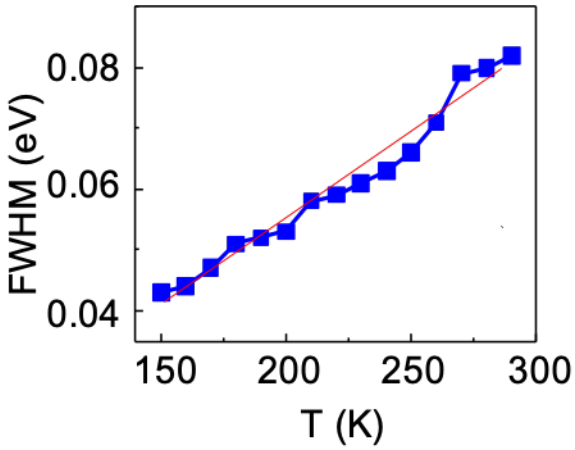


Figure 6.5: FWHM of P-OABR from temperatures 150-300K. We can extract the phonon energy by fitting the FWHM to $\Gamma(T) = \Gamma_0 + \sigma T + \Gamma_1/e^{(\frac{-\hbar\omega}{K_b T}-1)}$ where $\Gamma$(T) corresponds to FWHM at temperature T and first term on the left represents inhomogeneous broadening the second and third term are due to exciton phonon coupling with $\hbar\omega$ corresponding to the phonon energy and $K_B$ the Boltzmann constant[191]

sions, and a broad band centered at 505 nm, arising from defect and bound exciton emissions in the orthorhombic phase. Figure 6.7 (c) is a representative spectrum at 40 K.

The most prominent difference in the emission properties of P-OABr and P-APTES at low temperatures is clear in Figures 6.7 (b) and 6.7 (d). There is no emergence of the high energy emission peak, indicating P-APTES remain in the original cubic phase. P-OABr and P-APTES have identical chemical structures before passivation, implying that the origin of this phase stabilization is in the variation of surface energy between the quantum dots due to differences in surface ligands and nanoscale morphology. Our group previously reported the formation of smaller and more uniform spherical PQDs with branched ligand APTES, due to slower monomer delivery, while linear ligands lead to a significant percentage of sheet-like structures, some of which can be seen in Figure 6.4 [81]. Researchers have previously observed such intriguing crystal phase dynamics in MA - and FA-based PQDs, although the underlying reasons have been difficult to identify[192].

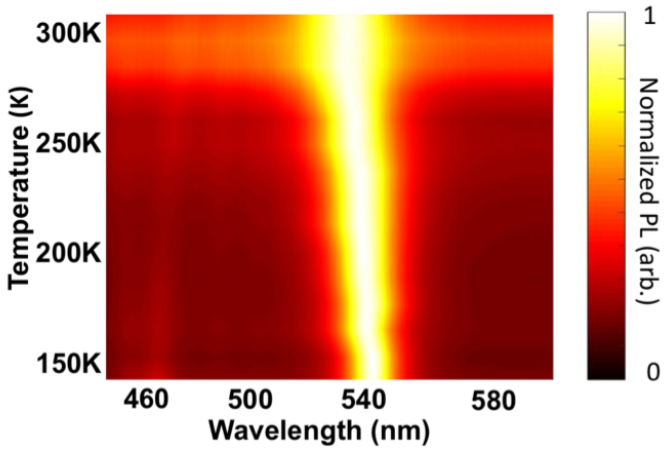


Figure 6.6: Photoluminescence (PL) intensity mapped with emission wavelength and temperature (300-150 K) for P-OABr.

Unlike bulk materials, the surface energy contribution has a more significant perturbation in the Gibbs free energy of nanoparticles, and hence plays an important role in determining the crystal phase. By varying the surface energy of nanomaterials, it is possible to attain a thermodynamically stable polymorph of the crystal, otherwise metastable in the bulk. One example is the stabilization of the $\alpha$ $Al_2O_3$ phase at room temperature for crystallites smaller than 14 nm, while bulk prefers $\alpha$ $Al_2O_3$[193]. Size driven effects on structural phases have also been observed in metal

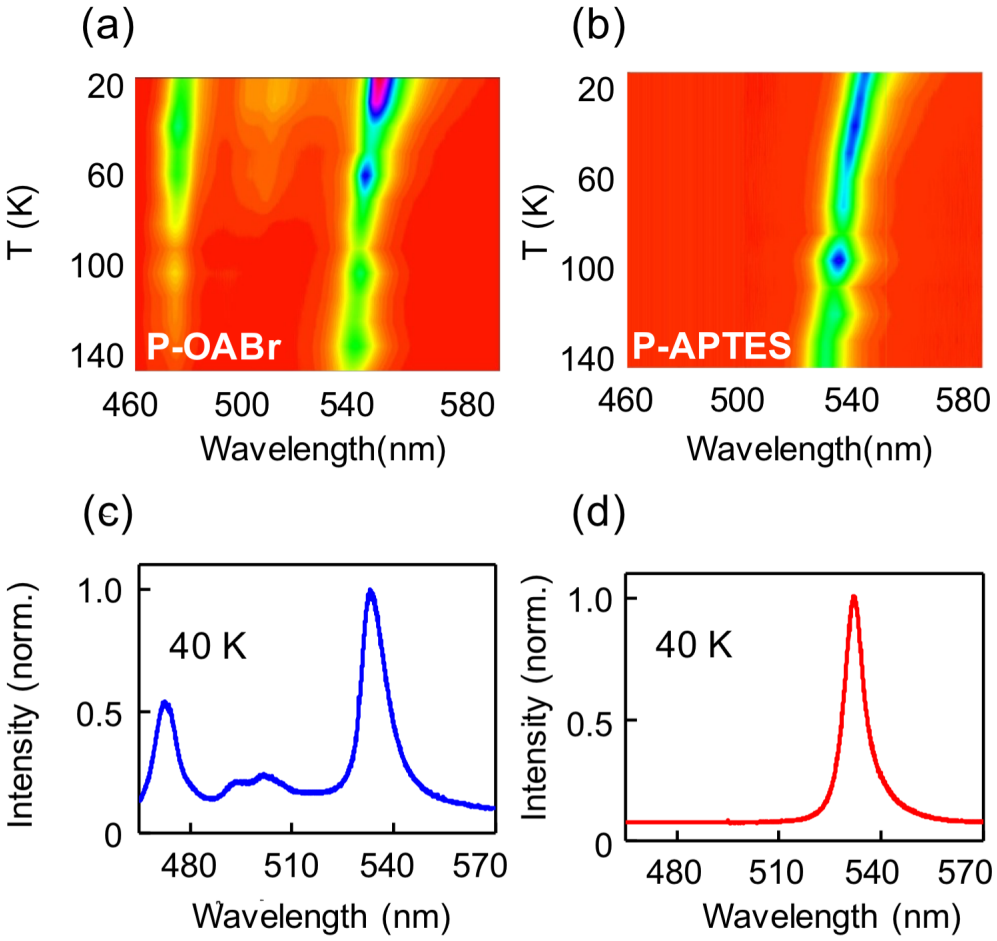


Figure 6.7: Photoluminescence (PL) intensity mapped with emission wavelength and temperature for (a) P-OABr and (b) P-APTES. Linecuts of the same maps at 40 K for (c) P-OABr and (d) P-APTES.

oxides like $TiO_2$ and lanthanides[194], while low temperature phase stabilization has been reported in $CsPbI_3$ nanocrystals[87]. Furthermore, bromide-based perovskite crystals have an internal energy difference of 7 kJ/mol between the cubic and orthorhombic crystal phases at room temperature, which can be used as an estimate of the surface energy contribution needed to modify the crystal phase diagram[75]. To further understand the mechanism behind this phase stabilization in P-APTES, and uncover any other consequences, we follow up with spectroscopy as a function of temperature and include not just P-OABr and P-APTES, but additional PQDs of different sizes ligated with APTES, one larger ($> 10$ nm) and one smaller than P-APTES ($< 3$ nm). These are designated P1-APTES and P2-APTES, respectively.

As expected, PL spectrum of the larger quantum dots (P1-APTES) is red-shifted, while that of the smaller quantum dots (P2-APTES) is blue-shifted compared to that of P-APTES, as shown in Figures 6.8 (a) and 6.8 (b). Neither of these quantum dots show the phase transition, implying that the surface energy structural stabilization has contributions from both the nanoscale morphology and surface ligation, unlike the stabilization of $\alpha$ $Al_2O_3$ phase, which solely arises from morphology. Temperature dependent integrated PL intensity of the PQDs (Figure 6.9), fit with the Arrhenius equation $I(T) = I_0/(1 + C_1 e^{(-E_B/(k_B T))})$ , allows us to extract their respective exciton binding energies $E_b$. I(T) and $I_0$ are integrated PL intensities at temperatures T and 0 K. C1 is a constant and $k_B$ is the Boltzmann constant. The fits give values of 105 $\pm$ 4.3 meV for P-APTES and 230 $\pm$ 7.4 meV for P-OABr. The higher value of the latter is because of the presence of nanosheets in the ensemble[195].

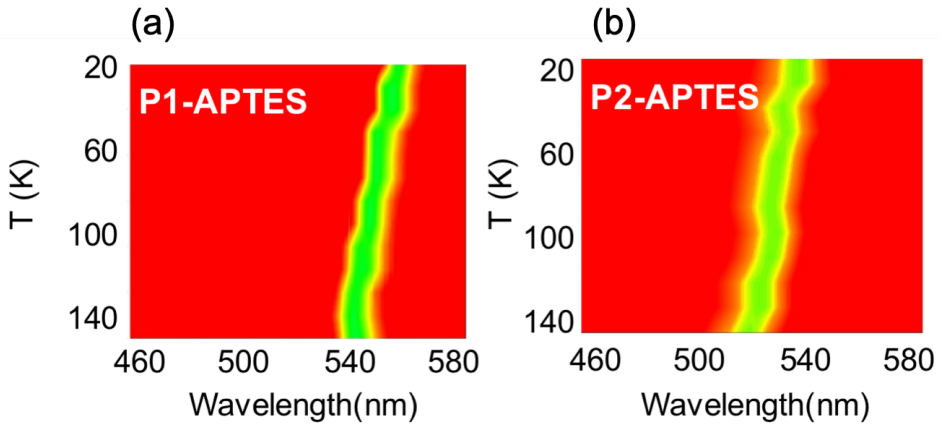


Figure 6.8: P1-APTES(a) and P2-APTES(b), PQDs ligated with APTES but with larger and smaller diameters than P-APTES.

Given that there could be a small chance that the absence of PL may be a result of trap states, we further probe phase transition in the PQDs using temperature dependent Raman scattering in the high frequency region where phonon modes appear, depending on structural symmetry. Intramolecular modes originating from methylamine can serve as an indication of structural phase transition. As seen in Figures 6.10(a) and 6.10(b), room temperature Raman scattering of P-APTES and P-OABr and exhibit broad peaks with no significant sharp features, typical for perovskite crystals with cubic phase symmetry, as they have no Raman-active phonon modes present[196]. However, upon lowering the temperature below 120 K, we observed a sharp Raman band for P-OABr at around 105 $cm^{-1}$, consistent with previous reports

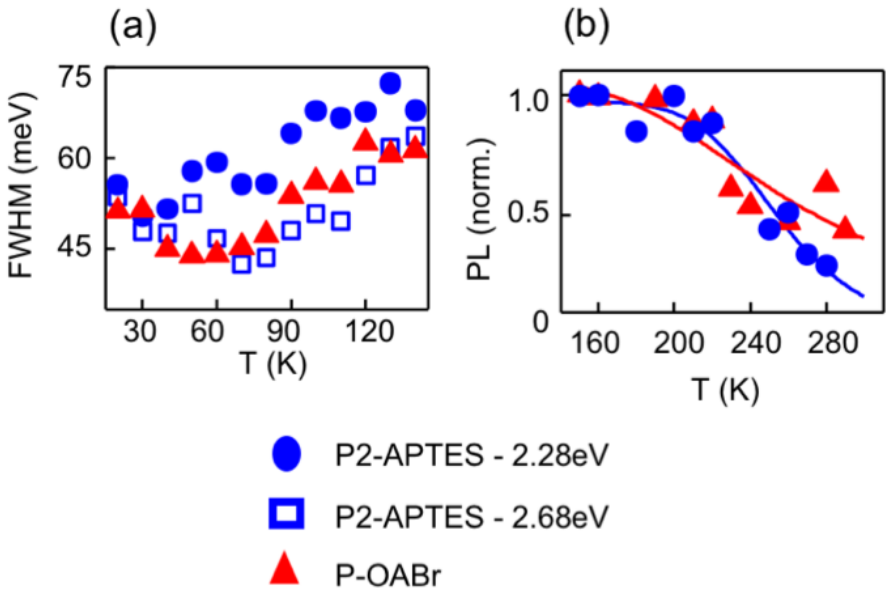


Figure 6.9: Full width half-maximum (FWHM)(a) values of PL emission spectra in P2-OABr and P-APTES varying with temperature. (b) Integrated PL varying with temperature fitted to Arrhenius equation to acquire exciton binding energy values.

of phase transition from tetragonal to orthorhombic phases[197]. On the other hand, no sharp feature in the Raman spectra was observed for P-APTES, even on lowering temperature below 70 K as shown in Figure 3.10(a), confirming the structure remains arrested in the cubic phase, and supporting our conclusion drawn from PL data.

Structural phase transition in perovskite thin films is accompanied by changes in charge carrier behavior, including both the type of carriers that dominate recombination (bimolecular or excitonic), as well the associated timescales. To correlate phase transition with carrier dynamics, we measured low temperature time resolved PL between 290 K and 20 K. Given that the calculated $E_b$ for the PQDs is larger than those of thin films, free carrier recombination is suppressed across the entire temperature range. The average lifetimes of exciton decay for P-OABr and P-APTES are calculated by fitting the data in Figures 6.11 (a) and 6.11 (b) to a stretched exponential fit $I(t) = I_o e^{((t/\tau)^{\beta})}$, to account for continuous higher order recombinations[198]. Although, even without the benefit of quantitative analysis, difference between the two trends with temperature is clearly visible. For P-OABr, the results mimic what is observed in thin film samples – a single, long lifetime in the tetragonal phase between 300–140 K followed by the emergence of a rapid recombination route when the or-

thorhombic phase appears[112]. In contrast, the P-APTES time-resolved curves show a continuous and gradual decrease of exciton lifetime with temperature. The values of these recombination times, extracted from fits, are plotted in Figures 6.12(a) and 6.12(b) for P-OABr and P-APTES, respectively.

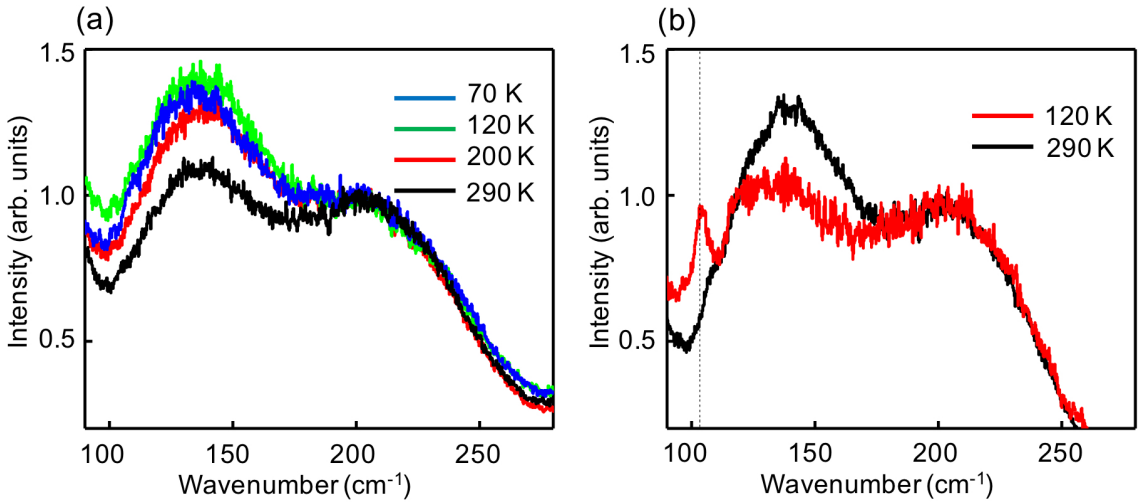


Figure 6.10: Raman microscopy results for (a) P-APTES and (b) P-OABr with varying temperature. While P-AOBr data show a second emerging peak at 120 K proclaiming the onset of transition to the orthorhombic phase, no such peak is observed in P-APTES.

They reveal an average lifetime of 2 ns and 9 ns for the two at room temperature, and the mildly longer value for the P-APTES ensemble is likely a reflection of more homogeneous morphology and size. The dynamics of the low energy PL in P-OABr in Figure 6.11(a) shows a sudden jump in the lifetime at around 210 K, reaching a value of 13.5 ns. It is interesting to note that this occurs at the same temperature where one would expect the cubic to tetragonal phase transition, and where such enhancements in carrier lifetimes can occur due to excessive scattering of excitons at grain boundaries. The lifetime decreases to 4 ns at 190 K and no big changes are observed till 140 K, where another sudden rise in carrier lifetime is observed, attributed to the phase transition from tetragonal to orthorhombic phase. As temperature was reduced further, a gradual decrease in the carrier lifetime was observed. Most colloidal quantum dots show an increase in PL lifetime with lowering temperature due to dominant excitonic emissions. Nevertheless, previous reports have indicated a reverse trend in PQDs where a reduction in charge carrier lifetime with lowering temperature arises

from the interactions of free and trapped excitons with surface states or localized states as relaxation pathways[199].

Around 130 K, the high energy band emerged with a much shorter lifetime, $\sim 350$ ps, compared to the lower energy band. This short carrier lifetime has been observed in perovskite thin films for the orthorhombic phase, and is attributed to the migration of charge carriers from the higher energy band to the lower energy tetragonal inclusions[112]. In the P-OABr dots, an interesting observation is the small contribution of higher order exponential decay terms in the higher energy band (evident from $\gamma$ values close to 1) indicating that the charge transfer rate between high and low energy bands to be at least an order of magnitude faster than the charge recombination rate. The formation of smaller tetragonal inclusions as temperature was lowered further increased the bi-excitonic recombination rate, with a gradual decrease in lifetime of this energy band, down to 300 ps at 40 K. As shown in Figures 6.11(b) and 6.12 (b), the time-resolved PL of P-APTES is far less complicated. The charge carrier lifetime continuously decreases as temperature is reduced, bottoming out at 1.4 ns at 70 K, with a small recovery beyond that. The recovery mechanism is still not fully understood, but may be related to thermal activation energy for charge transfer to localized centers or surface states previously mentioned.

Finally, we consider the dependence of integrated PL intensity on excitation power in Figure 5. The fit used is a power law, described as $I_{PL} = I_{ex}^{k}$. In direct bandgap semiconductors, $k > 2$ indicates free charge carrier recombination, $1 < k < 2$ for free and bound exciton recombination, and $k \sim 1$ signifies free to bound exciton recombination or the emission from excitons bound to isoelectronic defects or localized states, as observed in the case of silicon[200, 201]. Due to the high exciton binding energies in all our PQDs, we do not expect free carrier recombination to have a significant presence and this is proven correct. In Figure 6.13, P-OABr quantum dots show $k \sim 1$, confirming excitonic recombination, although there is a change of slope at higher powers due to saturation of the localized states involved, particularly at 290 K. In P-APTES, $k = 0.8$ at 290 K, which means that while recombination is predominantly due to free excitons, there is possibly some contribution from bound excitons. The weight of this latter category increases with decreasing temperature and we observed $k \sim 0.5$ at 200 K and 120 K.

## 6.3 Conclusion

In this work, we have studied the temperature dependent PL emission of PQDs ligated with two different ligands, OABr and APTES. PL spectra at low temperatures reveal the expected phase transition, from tetragonal to orthorhombic phase

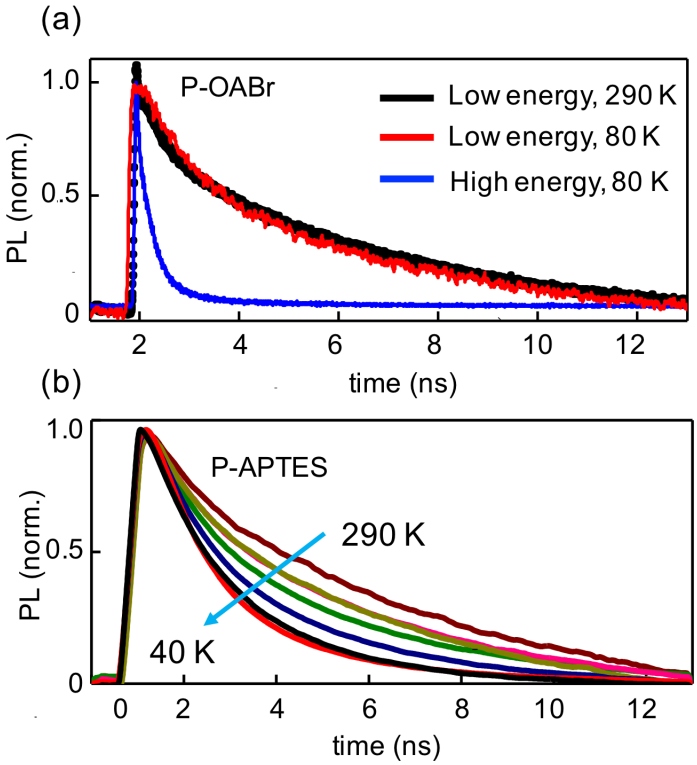


Figure 6.11: Time-resolved PL curves for (a) P-OABr and (b) P-APTES as functions of temperature.

in P-OABr at $\sim$ 140 K, but no such phase transition was observed in P-APTES, which remained in the cubic phase. We attribute this absence of phase transition to differences in surface energy contributions to their Gibbs free energy which significantly modifies the crystal phase diagram, leading to energetically stable crystal cubic phase in P-APTES nanocrystals. This difference in surface energy arises from difference in the surface ligation and the morphology of PQDs, with APTES favoring the formation of uniform spherical nanostructures. The observed phase stabilization in P-APTES was further demonstrated using Raman spectroscopy and time-resolved PL, which showed a sudden drop in PL recombination lifetime associated with the transition to orthorhombic structure in P-OABr, but not in P-APTES. Temperature and power dependent PL reveals strictly excitonic recombination over the full temperature range measurements are performed at, albeit with varying contributory levels from bound and free excitons. Our reported results establish a link between phase stabilization and morphology-related surface stabilization of PQDs. This opens up new possibilities of phase stabilization in other quantum dot systems using appropriate ligands and provide insights to proposing new routes for the stabilization of

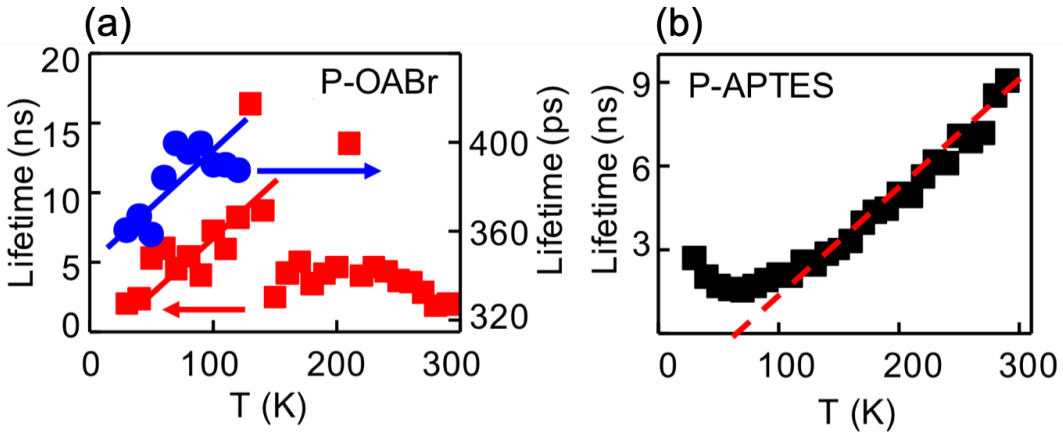


Figure 6.12: Recombination lifetimes extracted from stretched exponential fits of the two are plotted in (a) and (b), respectively. For P-OABr the high temperature low energy phase is plotted as squares and the low temperature high energy orthorhombic phase as circles. All lines in (a) and (b) are guides to the eye.

perovskite crystals.

## 6.4 Experimental Methods

PQDs are synthesized using previously reported methods by our groups[80, 81]. Detailed description of the synthesis process and an affirmation of surface ligation can be found in ref [81]. Samples for low temperature PL were prepared by drop-casting 2 $\mu$l of the PQDs in toluene onto clean glass slides and subsequent drying. For optical measurements, we used two excitation sources: a tunable, pulsed ultrafast laser (MIRA 900) with a repetition rate of 76 MHz, and continuous wave (CUBE) laser emitting at 409 nm. The PL data were taken using an Acton 300i spectrometer and then dispersed onto a thermoelectrically cooled charge-coupled device (CCD) with a spectral resolution of 0.18 nm. For time-resolved PL measurements we used a time-correlated single photon counting (TCSPC) system (Picoquant) in conjunction with the pulsed source. The temperature dependent measurements were done in a cryo-free system from Advanced Research Systems with a base temperature of 10 K. Transmission electron microscopy (TEM) and X-ray powder diffraction were used to demonstrate high crystallinity and attain average PQD size. The P-APTES and P-OABR were carefully dispersed on a silicon substrate to perform the Raman scattering measurements. A variable wavelength continuous wave diode laser source, operated at wavelength - 915 nm with power - 100 $\mu$W was focused on the sample using a 50X

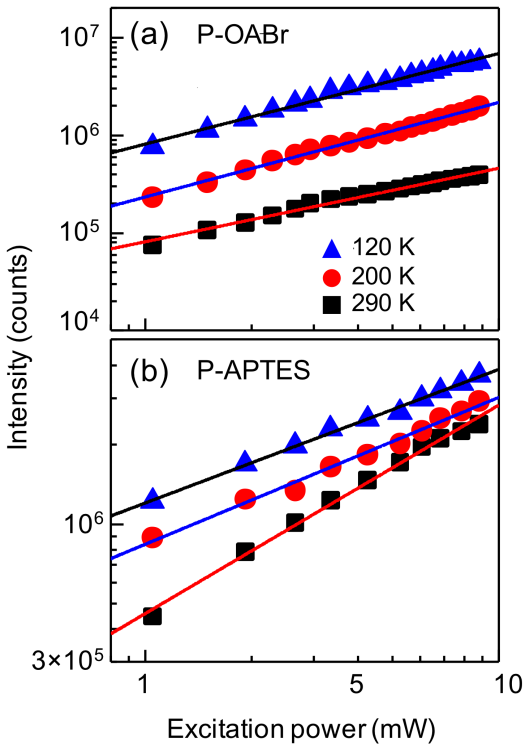


Figure 6.13: Integrated PL intensity as functions of excitation power at different temperatures for (a) P-OABr and (b) P-APTES. Power law fits are used to identify the type of carriers participating in the emission (explained in text).

objective. The wavelengths below bandgap were used to minimize the exciton-phonon interaction. The backscattered light was passed through the same objective and a single stage spectrometer, and collected using a liquid nitrogen cooled CCD camera. The slit width of the single spectrometer was set at 100 m. All measurements are done in closed cycle helium cooled cryostat at temperature 70 - 300 K.

## 6.5 Acknowledgements

The work was done in collaboration with Prof. Jin Zhang, Dr. Sara Bonabi, Dr. Binbin Luo, Prof. Michael Scheibner and Dr. Parveen Kumar. Prof. Zhang, Dr. Bonabi and Dr. Luo prepared the perovskite quantum dots and helped with the transmission electron microscopy images and XRD spectra. Prof. Michael Scheibner and Dr. Parveen Kumar performed the low temperature Raman spectroscopy

imaging. This work was supported by NASA MIRO Grant No. NNX15AQ01A.

# Chapter 7

# Spin polarized charge carrier dynamics in perovskite quantum dots

In just over a decade, hybrid organic-inorganic perovskites have made rapid progress as next generation of solar cell materials.[4] Recently, perovskite semiconductors have also shown great promise as candidates for spintronic applications, attributed to their high spin-orbit coupling, polarization dependent excitation properties and high band edge tunability.[106, 107] After stabilizing the crystal structure of perovskite quantum dots at low temperatures, we were interested in investigating their spin polarized exciton dynamics using circularly polarized resonant light excitations. Hanle effect measurement is employed, that revealed a exciton spin lifetime of 111 ps at 90K. The lifetime decreased to 16 ps at 120 K due to larger spin scattering at elevated temperatures. Further, in doped perovskite quantum dots, efficient energy transfer between the quantum dot excitonic bands and dopant Manganese(Mn) ion energy levels is achieved, resulting in Mn ion ${}^6A_1(\frac{5}{2}) \longrightarrow {}^4T_2(\frac{3}{2})$ energy emission. Optical spin orientation of the dopant Mn ions through spin polarized exciton energy transfer from the quantum dot is demonstrated. These results shed light into spin polarized dynamics in perovskite quantum dots, providing insights into future perovskite spintronics studies.

## 7.1 Introduction

Progress in the field of spintronics, both experimental and theoretical, has led to the exploration of different materials for their potential application in spintronic devices. Among them, perovskite semiconductors with their large spin orbit coupling(SOC), optically selective excitations, high optical quantum yield and long exci-

ton recombination lifetimes have shown promise in potential application in spin-based devices.[4, 106, 107]

Over the last decade, alongside the extensively studied photovoltaic applications, perovskite semiconductors also forayed their way into other opto-electronic devices[93], such as LEDs[101, 165], sensors[202], Photodetectors[203], lasers[90, 92] and, even spin based devices[107]. The large spin orbit coupling in the electronic band structure of perovskite semiconductors is due to the presence of heavy atoms such as Pb and Sn, that give it some unusual temperature dependent optical properties such as the red shifting of its PL with lowering temperature. Scientists have also predicted Rashba/Dresselhaus effect in perovskite attributed to random, static and dynamic structural distortions in the crystal structure that removes inversion symmetry leading to a noncentrosymmetric crystal, a prerequisite for such effects. This can lead to a spin dependent splitting in the conduction band extremum, resulting in an indirect band gap material.[30, 204] Recent reports have also indicated this indirect nature of the band gap to be the reason for the large recombination lifetime and long diffusion lengths, observed in perovskite solar cells. However, a comprehensive understanding of Rashba effect in perovskite solar cells is still lacking and its observation still challenged.[49] In 2018, Frohna et al. suggested incorrect structural relaxations to be responsible for observing Rashba effect in theoretical predictions ruling out any dynamic or static Rashba effects.[49].

Nonetheless, there is an enormous interest generated on perovskite semiconductors for spintronics. One such experimental investigation was to measure spin relaxation lifetimes in perovskite semiconductors. These measurements establish a lower limit on spin decoherence lifetimes of electrons or holes in semiconductors.[205, 206] Long spin relaxation times are of paramount importance for the use of spin in quantum information processing systems. Wang et al. reported circular polarized emission from hybrid perovskite thin films and reported a spin dephasing lifetime of 240 ps at 77K.[202] Most semiconducting systems require low temperatures to observe spin related phenomenon attributed to low thermal scattering of electrons. Odenthal et al. observed long spin decoherence lifetimes on the order of nanoseconds in perovskite thin films using time resolved Faraday rotation measurements.[107] In order to check for the common Elliot-Yafet, Dyakonov-Perel and Bir-Aronov-Pikus spin relaxation mechanisms in perovskite thin films, Odenthal et al. looked at spin scattering rate with temperature. Despite having a pristine sample, it was concluded that spins in perovskite semiconductors do not relax via a single relaxation pathway, due to its polycrystalline nature.[107]

These experiments confirmed that electron spin polarization can be generated in perovskite semiconductors through optical excitation. This was again validated

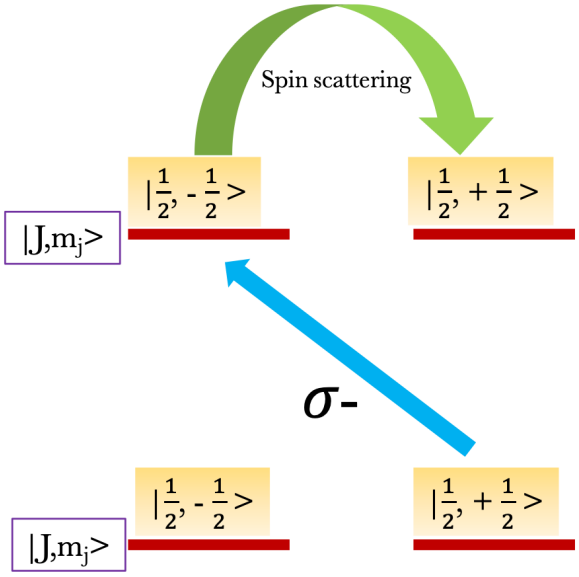


Figure 7.1: Schematic of polarization dependent excitation in perovskite electronic band structure. $\sigma-$ stands for left circular polarized light.

by Wang et al. in 2018, when they demonstrated two prototype spin based opto-electronic devices, a spin LED and a spin valve with high magnetoresistance.[106] Though, still a prototype device, it confirmed the ability of spin control and manipulation in perovskite semiconductors. These above mentioned results opened the research field of perovskite spintronics. With impressive results seen in thin films, it only seemed compelling to look into perovskite quantum dots systems for improved spin control and longer dephasing lifetime. Quantum dot systems are predicted to have longer spin decoherence times credited to their discrete energy level spitting, for example, several quantum dots systems such as lnAs, CdSe, systems have shown long nanosecond spin lifetimes.[205, 206]

In this work, we investigate spin relaxation timescales and mechanisms in perovskite quantum dots using Hanle effect. PQDs show spin polarized optical emissions at a low temperature of 80K, but their control is difficult due to multiple relaxation pathways, which is believed to arise from defect related scattering and improper surface passivation. Energy transfer from the spin polarized exciton to $Mn^{2+}$ ion dopants confined within the quantum dot is also investigated. Circular polarized emission associated with $Mn^{2+}$ spin orientation is demonstrated in the absence of an external magnetic field. The polarization is persistent up to a temperature of $\sim$120 K. To our knowledge, this is the first result indicating spin injection from a perovskite host to

a dopant material.

## 7.2 Results and Discussion

### Hanle effect measurement

Initial spin relaxation measurements were conducted on $CH_3NH_3PbBr_3$ (C-PQD). The energy bands in a PQD are determined by Pb and halide ions, the cation does not contribute to the band edge formation. They are though essential for crystal stability and contribute to electron spin scattering pathways. C-PQD were synthesized using previously reported techniques.[80, 81] X-ray diffraction spectra revealed confirmed cubic crystal structure at room temperature. Previous reports from our group have shown the effects of different ligands on the uniformity of PQDs. A branched ligand led to much higher uniformity with low size distribution compared to a linear ligand such as the commonly used octyl amine (OA) or octyl aminebromide (OABr). Hence, the PQD was surface functionalized using the branched APTES ligand. This primarily satisfy the need for a uniform distribution of PQD size as well as stabilizes the cubic crystal structure at low temperatures.
In general, at low temperatures, perovskite semiconductors have multiple pholuminescence(PL) emission peaks, the reason behind this is still controversial. The most commonly agreed upon hypothesis is the existence of two crystal phases resulting from partial phase transitions.[112, 163] While some researchers have also suggested biexcitonic emission or cation disorder at low temperatures to be a possible reason for multiple emission bands.[207, 208] Though the reason behind the emergence of multiple energy bands at low temperature is still debated, the concurrent occurrence of faster charge carrier recombination due to carrier migration between the two energy bands, was consistently observed between multiple groups.[112, 163, 207–209] In order to prevent this, APTES was used to surface functionalize the PQD (details in chapter 5).

Hanle effect is used to measure the scaled spin lifetimes ($gT^*$, g being the Lande factor) in C-PQD. In a typical Hanle effect measurement, resonant optical excitation is used to spin polarize charge carriers and the degree of polarization of their resultant emission is measured. By depolarizating the excited spin states using a transverse magnetic field, the spin lifetime $T^*$ can be obtained from the half width half max of the Hanle curve :[118]

$$T^* = \frac{\hbar}{\mu_B g B_{\frac{1}{2}}} \tag{7.1}$$

where $\hbar$ is the Planck's constant, $\mu$ is the Bohr magneton, and $B_{\frac{1}{2}}$ is the half width

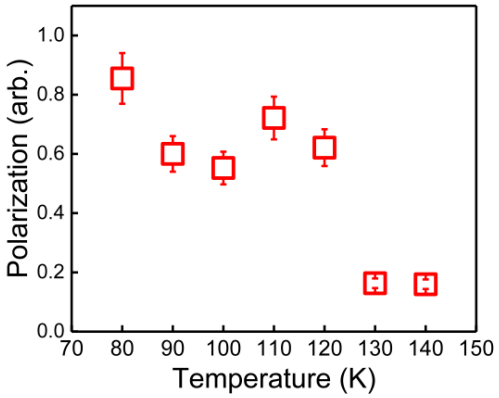


Figure 7.2: Zero-field spin polarization in perovskite quantum dots between 80-140K

half max of the lorentzian Hanle curve. Right or left circular polarized light were used to optically excite spin polarized excitons as shown in figure 7.1. Angular momentum conservation rules determine the excitation dynamics of electrons from the valence band to the conduction (both represented by the total angular momentum operator J and angular momentum projection along z axis, $m_j$). It is to be noted that this representation is an approximation as solid materials lack rotational symmetry and only works as the band extremes are predominantly formed by the Pb ion orbitals. The amount of polarization in the emission is defined as:

$$P = \frac{I_{PL}(+) - I_{PL}(-)}{I_{PL}(+) + I_{PL}(-)} \tag{7.2}$$

As shown in figure 7.2, at zero magnetic fields, we were able to observe ∼1% polarization in C-PQD. The observed value of polarization is in agreement with previously reported studies. On further increasing the temperature we observe a sudden sharp decrease in the polarization at $\sim$ 120 K. Wang et al. reported a similar decrease observed in polarization in perovskite thin films and suggested it to arise from phase transitions in perovskite films. Here, however the crystal phase is arrested and there is an absence of phase transitions (Chapter 5). Therefore the quenching of spin polarization cannot be associated with phase transitions. We hypothesize this sudden drop in spin polarization in PQDs to be a result of exchange interaction driven spin flipping, resulting in an average zero spin orientation. Spin flipping in materials is associated with a second order phase transition like the one observed here, mathematically similar to a ferromagnetic to paramagnetic phase transition at the Curie temperature. Within the mean field approximation, the spin exchange interaction

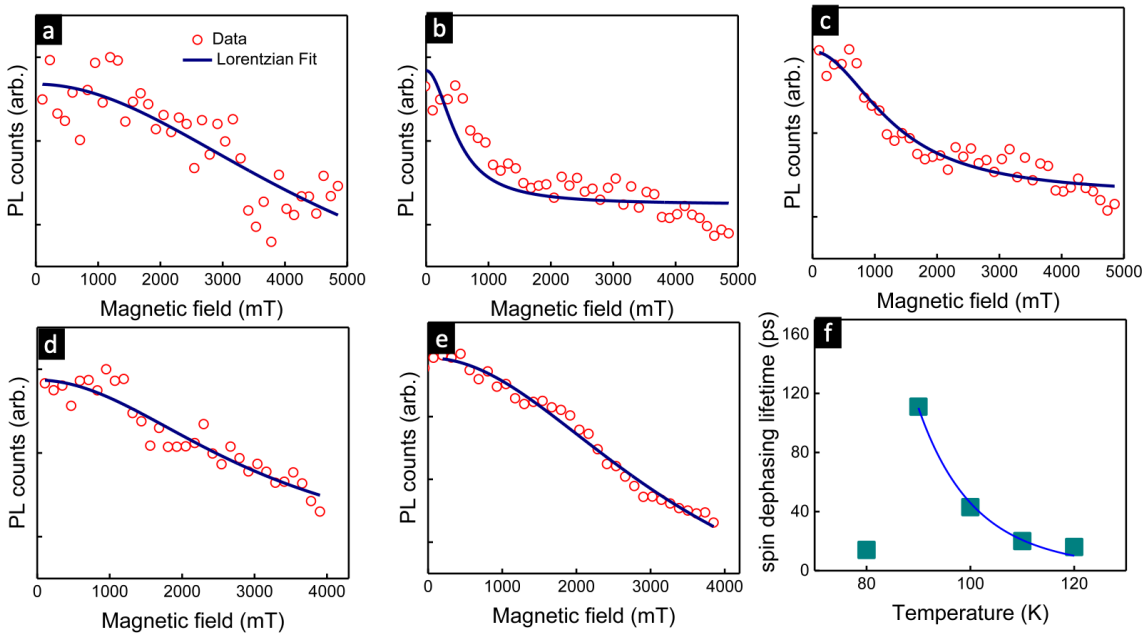


Figure 7.3: (a)-(e) Hanle depolarization curve of PQDs from 80-120K, respectively. (f) temperature dependent spin lifetimes T* calculated from fits to Hanle curves

energy of a 2D spin lattice can be calculated as[210]

$$J = \frac{2kT_c}{z} \tag{7.3}$$

where k is the Boltzmann constant, $T_c$ is critical temperature and z is the number of nearest neighbours. Assuming the critical temperature to be 120K we get an exchange interaction energy of 5 meV. The formalism assumes the optical pumping to orient the spins and the spin flipping to occur at a timescale much faster than other spin relaxation pathways. This however is a simplistic approach and further understanding requires extensive theoretical study, not within the scope of this work.

Following this, the Hanle depolarization curve was measured for C-PQD within the temperature range, 80-120 K, above which the zero-field polarization approximates to zero (figure7.3]. Samples were resonantly excited using 500nm pulsed laser (77.8Mhz). As shown in figure 7.3 , the curves were fit to a lorentzian curve to deduce the spin lifetime T*. The spin lifetime is related to the exciton recombination lifetime $\tau_{ex}$ and

spin relaxation lifetime $\tau_s$ by[118]

$$\frac{1}{T^*} = \frac{1}{\tau_{ex}} + \frac{1}{\tau_s} \tag{7.4}$$

As shown in figure 7.3f, between 90-120 K the spin lifetime follows the expected trend. The spin lifetime decreases exponentially from 111 ps at 90 K to 16 ps at 120 K (value of g = 2.03).[202] The decrease is attributed to increased thermal scattering rates at higher temperatures. While a longer lifetime is expected in quantum dots compared to thin films, the observed values were indeed similar, if not shorter than their thin film counterpart. One major reason for this shorter lifetime could be the high concentration of surface defects in perovskite quantum dots. Being a relatively recent material in opto-electronic research, synthesizing PQDs with uniform morphology and low defects is still a major challenge. Additionally, the low exciton Bohr radius (2.5nm) of PQDs, downplays quantum confinement effects. Nonetheless, the observed Hanle effect in perovskite quantum dots opens opportunities into PQD spintronics.
It is to be noted that the sample shows an abnormally short spin lifetime of 14 ps at 80 K. The origin of this abnormality is not clear and could arise from imperfections in the sample or degradation of the surface ligands.

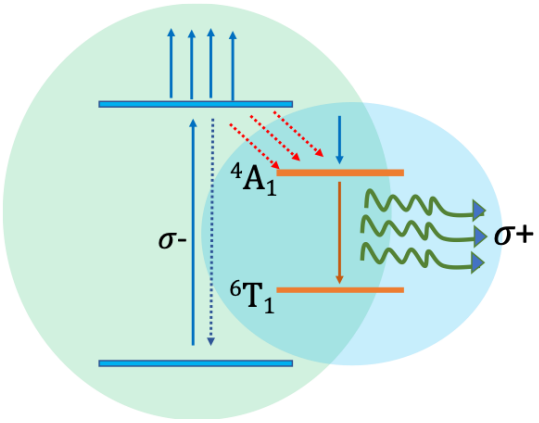


Figure 7.4: Schematics showing non radiative energy transfer from the quantum dot to the $Mn^{2+}$ energy levels

## Spin polarization of $Mn^{2+}$ions

Even though optical spin polarization in C-PQD is realized, their spin decoherence lifetimes and polarization values are highly dependent on PQD quality, size and

defect passivation. Controlled incorporation of dopant impurities in a semiconductor host could open further routes to effectively control the optical properties of the host material. Efficient energy transfer between II-IV semiconductor quantum dots and Manganese 2+ ions through sp-d interactions are widely reported.[211–214] Recently, studies have also demonstrated successful incorporation of Mn ions into 2D Ruddlesden-Popper perovskite quantum dots (RP-PQD). The layered structure of the quantum dots provide sufficient intercalation of the dopants. RP-PQD have a crystal structure $A_2BX_4$ with a similar band structure to C-PQD. Direct optical excitation from ${}^6A_1(\frac{5}{2}) \longrightarrow {}^4T_2(\frac{3}{2})$ in the $3d^5$ shell of the $Mn^{2+}$ is spin forbidden (the bracket indicates S, total spin angular momentum and not the spin projection along z axis, $s_z$).[215–217] This is sometimes partially overcome through spin orbit coupling of dopant ions with the anion of the host material. It is however possible to excite the ${}^6A_1$ level of the dopant Mn ion, through Auger non-radiative recombination of 'bright' and 'dark' excitons in the quantum dot host (figure 7.4.[215–217] Once excited, the radiative recombination into the ${}^4T_2(\frac{3}{2})$ occurs through phonon mediated processes. The most commonly accepted mechanism of non radiative recombination mediated energy transfer is through sp-d mixing of energy orbitals. It is also possible to have some amount of Coulomb interaction assisted non radiative recombination.[215–217]

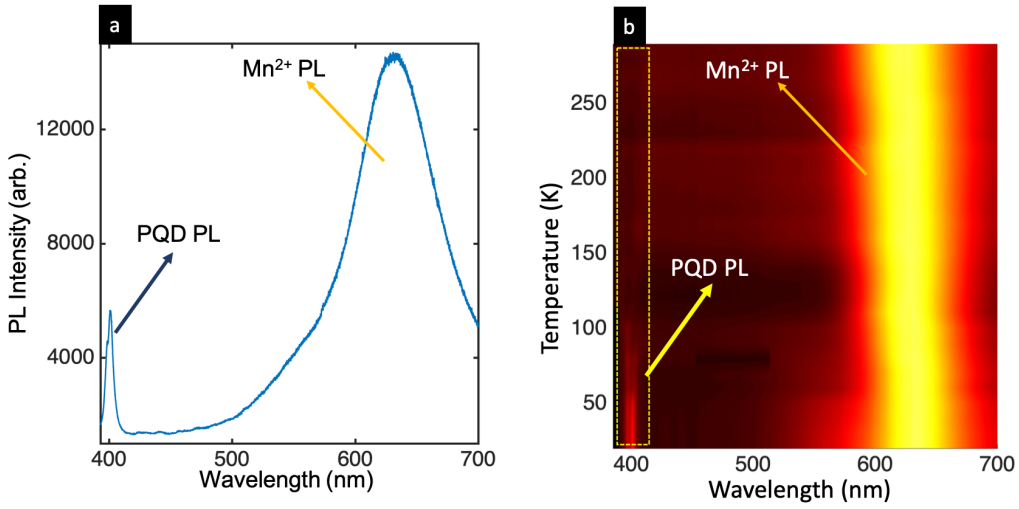


Figure 7.5: PL spectra at 50 K showing excitonic and $Mn^{2+}$ emission peaks (a). Temperature dependent PL map showing efficient energy transfer between the quantum dot and Mn ion dopants

As shown in figure7.5 a, the PL spectra at 50 K shows efficient energy transfer be-

tween the RP-PQD excitons and $Mn^{2+}$ energy levels. The Mn ion doped RP-PQD (Mn:RP-PQD) was synthesized using a previously reported technique. The Mn ion doping concentration in our samples were $\leq 5\%$ . At low temperature, radiative recombination process dominates over non-radiative ones and results in lower efficiency energy transfer to the dopant ions. In Mn:RP-PQD system, the temperature dependent PL map indicates an efficient transfer mechanism even at extremely low temperatures, contrary to studies on doped CdSe/ZnSe quantum dots. We believe this unconventional behaviour to possibly arise due to two reasons a) Trapped excitons have been observed (even at 20K) in RP-PQDs, leading to broad band white light emission. Energy transfer could occur through the trapped exciton recombination b) lower exciton binding energy in RP-PQDs, aiding exciton dissociation even at low temperatures.

Nawrocki et al. showed that the energy transfer mechanism in Mn doped quantum dots is spin-dependent and that the exciton-Mn transfer rates were suppressed in the presence of a magnetic field.[217] Selection rules require the total spin projection of the system to be conserved, i.e. $s_z^{ex} + S_z$. This implies that a bright exciton ($s_z^{ex}$=0) cannot non radiatively excite out of ${}^6A_1(s_z = \pm\frac{5}{2})$ level as this would require $\Delta S = \pm 1$, while a dark exciton ($s_z^{ex} = \pm 0$) can excite this spin state. While this is true for most systems, it may not hold for systems with strong spin-orbit coupling (like perovskite semiconductors) where the spin projection would be replaced by the total angular momentum projection term $J_z^{ex}$ and therefore opens the possibility for bright excitons with $\Delta J = \pm 1$ to excite the $s_z = \pm\frac{5}{2}$ spin state.[216]

We observed spin polarized emission in Mn doped quantum dots in the absence of an external magnetic field. RP-PQD is resonantly excited using left circular polarized light ($\sigma-$) at 380 nm and the emission from the Mn ions is analysed using circular polarized spectroscopy. We observe a right circular polarization of 4%, in the emission PL at 80K. The polarization value drops to 2.4% at 120 K (figure7.6b). The fact that the $Mn^{2+}$ PL polarization is opposite to the excitation polarization, indicates exchange coupling between the quantum dot excitons and $Mn^{2+}$ $3d^5$ electron. Figure 7.6a shows the PL spectra comparing $\sigma+$ and $\sigma-$ emissions. The Mn ion polarization also persists at higher temperature indicating a faster spin transfer process compared to spin dephasing mechanisms. Some earlier reports have indicated circular polarized emission from $Mn^{2+}$ ions in InGaAs quantum well structures, where they proposed the dopants to act as a spin reservoir due to their relatively long spin relaxation times. It is to be noted that these new findings are not the same as the ones observed in diluted magnetic semiconductor nanocrystals, where a similar spin polarized emission was observed in $Mn^{2+}$ ion was detected in a high magnetic field.[214] There, researchers noted no spin memory retention from selective spin excitation of the nanocrystal

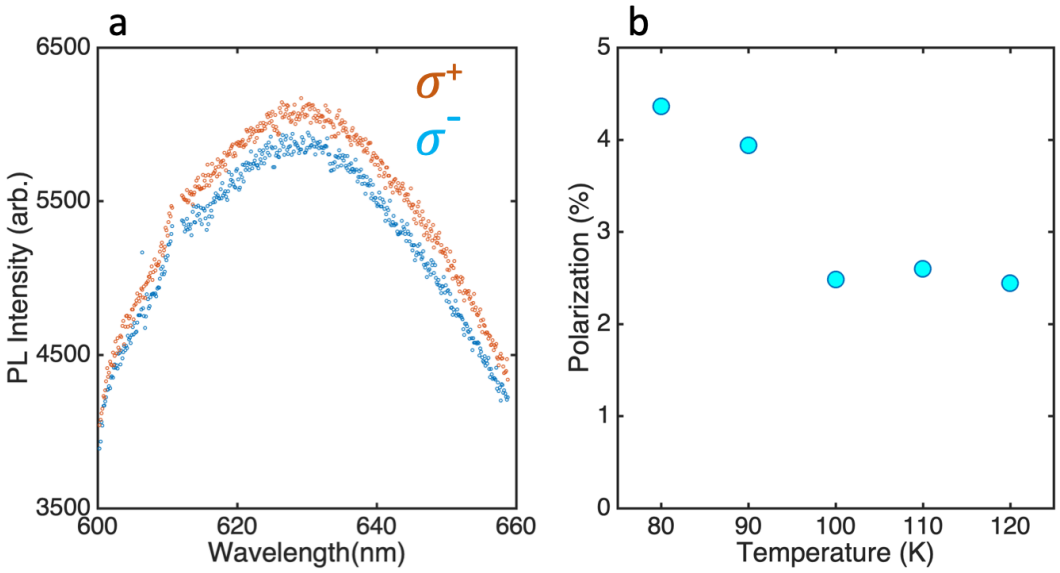


Figure 7.6: Right ($\sigma^+$) and Left ($\sigma^-$) circular polarized components of the $Mn^{2+}$ PL emission following excitation from Left circular polarized light (a). Temperature dependent $Mn^{2+}$ spin polarization (b)

and the spin polarization in the dopant was achieved only after the application of a strong magnetic field.[214] While the exact underlying mechanism behind such spin polarization is not fully understood, it is believed to arise from strong s p band and d orbital hybridization, greater than that of conventional quantum dots, that can lead to spin preserved energy transfer. Additionally high level of band mixing can also lead to non-radiative pathways other than the expected Auger recombination, between the exciton and $Mn^{2+}$ energy levels. We propose two possible mechanisms that can lead to this spin polarized emission, (a) exchange interaction between the excited Mn ion electron spins and optical injected exciton spins. Theoretical studies have shown that off-diagonal terms of the sp-d exchange interaction to facilitate simultaneous spin-flips and spin transfer from the PQD to Mn ions.[218, 219] (b) Secondly, assuming a spin conserved energy transfer between the quantum dots and $Mn^{2+}$ $3d^5$ electrons, the transition probability between the ground state and other higher energy levels in $Mn^{2+}$ have different transition probabilities, leading to a non-equilibrium distribution of Mn spins.[220] Both these mechanisms could lead to a spin polarization in $Mn^{2+}$ ions.

Establishing the exact mechanism requires additional experimental and theoretical studies, nonetheless, we successfully achieved spin polarized emission from doped Mn

ions through spin polarized exciton injection. Future studies on the role of the recently observed magnetic polarons in perovskite semiconductors, in the exchange interaction as well as the in energy transfer mechanisms also needs examination.

## 7.3 Conclusion

In conclusion, we were able to optically excite spin polarized charge carriers in perovskite quantum dots using circularly polarized resonant excitation. Hanle effect was used to study their spin relaxation lifetimes. which range from 111 ps to 16 ps in the range 90K to 120 K, respectively. Doping of Mn ions in RP-PQD resulted in efficient energy transfer from the exciton to the $Mn^{2+}$ $3d^5$ energy levels. In addition, optical polarized charge carriers from the quantum can transfer the spin information to the dopant ion even in the absence of a magnetic field. This experimental realization of spin writing in a dopant magnetic ion confined with a quantum dot opens opportunities for optical information storage devices and quantum computing.

## 7.4 Acknowledgements

The work was done in collaboration with Prof. Jin Zhang and Dr. Sara Bonabi. Prof. Zhang and Dr. Bonabi prepared the doped and undoped perovskite quantum dots. This work was supported by NASA MIRO Grant No. NNX15AQ01A.

# Bibliography


1. Odabasi, Ç. & Yildirim, R. Performance analysis of perovskite solar cells in 2013-2018 using machine-learning tools. *Nano Energy* **56,** 770–791 (Feb. 2019).
2. Shi, Z. & Jayatissa, A. H. Perovskites-Based Solar Cells: A Review of Recent Progress, Materials and Processing Methods. *Materials (Basel, Switzerland)* **11.** doi:10.3390/ma11050729. http://www.ncbi.nlm.nih.gov/pubmed/29734667 (May 2018).
3. Hong, K., Le, Q. V., Kim, S. Y. & Jang, H. W. Low-dimensional halide perovskites: review and issues. *Journal of Materials Chemistry C* **6,** 2189–2209 (Mar. 2018).
4. Jena, A. K., Kulkarni, A. & Miyasaka, T. Halide Perovskite Photovoltaics: Background, Status, and Future Prospects. *Chemical Reviews* **119,** 3036–3103 (Mar. 2019).
5. Park, N.-G. Perovskite solar cells: an emerging photovoltaic technology. *Materials Today* **18,** 65–72 (Mar. 2015).
6. *Best Research-Cell Efficiency Chart — Photovoltaic Research — NREL* https://www.nrel.gov/pv/cell-efficiency.html (2019).
7. Kojima, A., Teshima, K., Shirai, Y. & Miyasaka, T. Organometal Halide Perovskites as Visible-Light Sensitizers for Photovoltaic Cells. *Journal of the American Chemical Society* **131,** 6050–6051 (May 2009).
8. Ning, W., Wang, F., Wu, B., Lu, J., Yan, Z., Liu, X., Tao, Y., Liu, J.-M., Huang, W., Fahlman, M., Hultman, L., Sum, T. C. & Gao, F. Long Electron-Hole Diffusion Length in High-Quality Lead-Free Double Perovskite Films. *Advanced Materials* **30,** 1706246 (May 2018).
9. Motta, C., El-Mellouhi, F. & Sanvito, S. Charge carrier mobility in hybrid halide perovskites. *Scientific Reports* **5,** 12746 (Oct. 2015).
10. Yin, W.-J., Yang, J.-H., Kang, J., Yan, Y. & Wei, S.-H. Halide perovskite materials for solar cells: a theoretical review. *Journal of Materials Chemistry A* **3,** 8926–8942 (Apr. 2015).

11. Wu, W.-Q., Wang, Q., Fang, Y., Shao, Y., Tang, S., Deng, Y., Lu, H., Liu, Y., Li, T., Yang, Z., Gruverman, A. & Huang, J. Molecular doping enabled scalable blading of efficient hole-transport-layer-free perovskite solar cells. *Nature Communications* **9,** 1625 (Dec. 2018).

12. Deng, Y., Peng, E., Shao, Y., Xiao, Z., Dong, Q. & Huang, J. Scalable fabrication of efficient organolead trihalide perovskite solar cells with doctor-bladed active layers. *Energy & Environmental Science* **8,** 1544–1550 (May 2015).

13. Ishihara, H., Sarang, S., Chen, Y.-C., Lin, O., Phummirat, P., Thung, L., Hernandez, J., Ghosh, S. & Tung, V. Nature inspiring processing route toward high throughput production of perovskite photovoltaics. *J. Mater. Chem. A* **4,** 6989–6997 (May 2016).

14. Lee, M. M., Teuscher, J., Miyasaka, T., Murakami, T. N. & Snaith, H. J. Efficient hybrid solar cells based on meso-superstructured organometal halide perovskites. *Science* **338,** 643–7 (Nov. 2012).

15. Liu, M., Johnston, M. B. & Snaith, H. J. Efficient planar heterojunction perovskite solar cells by vapour deposition. *Nature* **501,** 395–398 (Sept. 2013).

16. Burschka, J., Pellet, N., Moon, S.-J., Humphry-Baker, R., Gao, P., Nazeeruddin, M. K. & Grätzel, M. Sequential deposition as a route to high-performance perovskite-sensitized solar cells. *Nature* **499,** 316–319 (July 2013).

17. Jeon, N. J., Noh, J. H., Yang, W. S., Kim, Y. C., Ryu, S., Seo, J. & Seok, S. I. Compositional engineering of perovskite materials for high-performance solar cells. *Nature* **517,** 476–480 (Jan. 2015).

18. Eperon, G. E., Stranks, S. D., Menelaou, C., Johnston, M. B., Herz, L. M. & Snaith, H. J. Formamidinium lead trihalide: a broadly tunable perovskite for efficient planar heterojunction solar cells. *Energy & Environmental Science* **7,** 982 (Feb. 2014).

19. Kulbak, M., Gupta, S., Kedem, N., Levine, I., Bendikov, T., Hodes, G. & Cahen, D. Cesium Enhances Long-Term Stability of Lead Bromide Perovskite-Based Solar Cells. *The Journal of Physical Chemistry Letters* **7,** 167–172 (Jan. 2016).

20. Zhou, W., Zhao, Y., Zhou, X., Fu, R., Li, Q., Zhao, Y., Liu, K., Yu, D. & Zhao, Q. Light-Independent Ionic Transport in Inorganic Perovskite and Ultrastable Cs-Based Perovskite Solar Cells. *The Journal of Physical Chemistry Letters* **8,** 4122–4128 (Sept. 2017).

21. Saliba, M., Matsui, T., Seo, J.-Y., Domanski, K., Correa-Baena, J.-P., Nazeeruddin, M. K., Zakeeruddin, S. M., Tress, W., Abate, A., Hagfeldt, A. & Grätzel, M. Cesium-containing triple cation perovskite solar cells: improved stability, reproducibility and high efficiency. *Energy & environmental science* **9,** 1989–1997 (June 2016).

22. McMeekin, D. P., Sadoughi, G., Rehman, W., Eperon, G. E., Saliba, M., Hörantner, M. T., Haghighirad, A., Sakai, N., Korte, L., Rech, B., Johnston, M. B., Herz, L. M. & Snaith, H. J. A mixed-cation lead mixed-halide perovskite absorber for tandem solar cells. *Science* **351,** 151–5 (Jan. 2016).

23. Rehman, W., McMeekin, D. P., Patel, J. B., Milot, R. L., Johnston, M. B., Snaith, H. J. & Herz, L. M. Photovoltaic mixed-cation lead mixed-halide perovskites: links between crystallinity, photo-stability and electronic properties. *Energy & Environmental Science* **10,** 361–369 (Jan. 2017).

24. Yuan, Z., Zhou, C., Tian, Y., Shu, Y., Messier, J., Wang, J. C., van de Burgt, L. J., Kountouriotis, K., Xin, Y., Holt, E., Schanze, K., Clark, R., Siegrist, T. & Ma, B. One-dimensional organic lead halide perovskites with efficient bluish white-light emission. *Nature Communications* **8,** 14051 (Apr. 2017).

25. Mao, L., Wu, Y., Stoumpos, C. C., Traore, B., Katan, C., Even, J., Wasielewski, M. R. & Kanatzidis, M. G. Tunable White-Light Emission in Single-Cation-Templated Three-Layered 2D Perovskites $(CH_3CH_3NH_2)_4Pb_3Br_{10-x}Cl_x$. *Journal of the American Chemical Society* **139,** 11956–11963 (Aug. 2017).

26. Smith, M. D. & Karunadasa, H. I. White-Light Emission from Layered Halide Perovskites. *Accounts of Chemical Research* **51,** 619–627 (Mar. 2018).

27. Brivio, F., Butler, K. T., Walsh, A. & van Schilfgaarde, M. Relativistic quasiparticle self-consistent electronic structure of hybrid halide perovskite photovoltaic absorbers. *Physical Review B* **89,** 155204 (Apr. 2014).

28. Ravi, V. K., Markad, G. B. & Nag, A. Band Edge Energies and Excitonic Transition Probabilities of Colloidal $CsPbX_3$ (X = Cl, Br, I) Perovskite Nanocrystals. *ACS Energy Letters* **1,** 665–671 (Oct. 2016).

29. Niesner, D., Hauck, M., Shrestha, S., Levchuk, I., Matt, G. J., Osvet, A., Batentschuk, M., Brabec, C., Weber, H. B. & Fauster, T. Structural fluctuations cause spin-split states in tetragonal $(CH_3NH_3)PbI_3$ as evidenced by the circular photogalvanic effect. *Proceedings of the National Academy of Sciences of the United States of America* **115,** 9509–9514 (Sept. 2018).

30. Zhai, Y., Baniya, S., Zhang, C., Li, J., Haney, P., Sheng, C.-X., Ehrenfreund, E. & Vardeny, Z. V. Giant Rashba splitting in 2D organic-inorganic halide perovskites measured by transient spectroscopies. *Science Advances* **3,** e1700704 (July 2017).

31. Isarov, M., Tan, L. Z., Bodnarchuk, M. I., Kovalenko, M. V., Rappe, A. M. & Lifshitz, E. Rashba Effect in a Single Colloidal $CsPbBr_3$ Perovskite Nanocrystal Detected by Magneto-Optical Measurements. *Nano Letters* **17,** 5020–5026 (Aug. 2017).

32. Kepenekian, M. & Even, J. Rashba and Dresselhaus Couplings in Halide Perovskites: Accomplishments and Opportunities for Spintronics and Spin-Orbitronics. *The Journal of Physical Chemistry Letters* **8,** 3362–3370 (July 2017).

33. Green, M. A., Ho-Baillie, A. & Snaith, H. J. The emergence of perovskite solar cells. *Nature Photonics* **8,** 506–514 (July 2014).

34. Yu, L. & Zunger, A. Identification of Potential Photovoltaic Absorbers Based on First-Principles Spectroscopic Screening of Materials. *Physical Review Letters* **108,** 068701 (Feb. 2012).

35. Yu, L., Kokenyesi, R. S., Keszler, D. A. & Zunger, A. Inverse Design of High Absorption Thin-Film Photovoltaic Materials. *Advanced Energy Materials* **3,** 43–48 (Jan. 2013).

36. Giorgi, G., Fujisawa, J.-I., Segawa, H. & Yamashita, K. Small Photocarrier Effective Masses Featuring Ambipolar Transport in Methylammonium Lead Iodide Perovskite: A Density Functional Analysis. *The Journal of Physical Chemistry Letters* **4,** 4213–4216 (Dec. 2013).

37. Shi, D., Adinolfi, V., Comin, R., Yuan, M., Alarousu, E., Buin, A., Chen, Y., Hoogland, S., Rothenberger, A., Katsiev, K., Losovyj, Y., Zhang, X., Dowben, P. A., Mohammed, O. F., Sargent, E. H. & Bakr, O. M. Solar cells. Low trap-state density and long carrier diffusion in organolead trihalide perovskite single crystals. *Science* **347,** 519–22 (Jan. 2015).

38. Stranks, S. D. & Snaith, H. J. Metal-halide perovskites for photovoltaic and light-emitting devices. *Nature Nanotechnology* **10,** 391–402 (May 2015).

39. Dong, Q., Fang, Y., Shao, Y., Mulligan, P., Qiu, J., Cao, L. & Huang, J. Solar cells. Electron-hole diffusion lengths ¿ 175 $\mu$m in solution-grown CH3NH3PbI3 single crystals. *Science* **347,** 967–70 (Feb. 2015).

40. Yin, W.-J., Shi, T. & Yan, Y. Unusual defect physics in $CH_3NH_3PbI_3$ perovskite solar cell absorber. *Applied Physics Letters* **104,** 063903 (Feb. 2014).

41. Frost, J. M., Butler, K. T., Brivio, F., Hendon, C. H., van Schilfgaarde, M. & Walsh, A. Atomistic Origins of High-Performance in Hybrid Halide Perovskite Solar Cells. *Nano Letters* **14,** 2584–2590 (May 2014).

42. Zhang, S. B., Wei, S.-H., Zunger, A. & Katayama-Yoshida, H. Defect physics of the $CuInSe_2$ chalcopyrite semiconductor. *Physical Review B* **57,** 9642–9656 (Apr. 1998).

43. Feng, W., Liu, J. & Yu, X. Efficiency enhancement of mono-Si solar cell with CdO nanotip antireflection and down-conversion layer. *RSC Adv.* **4,** 51683–51687 (Oct. 2014).

44. Nicoara, N., Lepetit, T., Arzel, L., Harel, S., Barreau, N. & Sadewasser, S. Effect of the KF post-deposition treatment on grain boundary properties in Cu(In, Ga)$Se_2$ thin films. *Scientific Reports* **7,** 41361 (Feb. 2017).

45. Grinberg, I., West, D. V., Torres, M., Gou, G., Stein, D. M., Wu, L., Chen, G., Gallo, E. M., Akbashev, A. R., Davies, P. K., Spanier, J. E. & Rappe, A. M. Perovskite oxides for visible-light-absorbing ferroelectric and photovoltaic materials. *Nature* **503,** 509–512 (Nov. 2013).

46. Zhang, S., Tang, N., Jin, W., Duan, J., He, X., Rong, X., He, C., Zhang, L., Qin, X., Dai, L., Chen, Y., Ge, W. & Shen, B. Generation of Rashba Spin-Orbit Coupling in CdSe Nanowire by Ionic Liquid Gate. *Nano Letters* **15,** 1152–1157 (Feb. 2015).

47. Di Sante, D., Barone, P., Bertacco, R. & Picozzi, S. Electric Control of the Giant Rashba Effect in Bulk GeTe. *Advanced Materials* **25,** 509–513 (Jan. 2013).

48. Mak, K. F., McGill, K. L., Park, J. & McEuen, P. L. Valleytronics. The valley Hall effect in $MoS_2$ transistors. *Science* **344,** 1489–92 (June 2014).

49. Frohna, K., Deshpande, T., Harter, J., Peng, W., Barker, B. A., Neaton, J. B., Louie, S. G., Bakr, O. M., Hsieh, D. & Bernardi, M. Inversion symmetry and bulk Rashba effect in methylammonium lead iodide perovskite single crystals. *Nature Communications* **9,** 1829 (Dec. 2018).

50. Zheng, F., Tan, L. Z., Liu, S. & Rappe, A. M. Rashba Spin-Orbit Coupling Enhanced Carrier Lifetime in CH $CH_3NH_3PbI_3$. *Nano Letters* **15,** 7794–7800 (Dec. 2015).

51. Im, J.-H., Jang, I.-H., Pellet, N., Grätzel, M. & Park, N.-G. Growth of $CH_3NH_3PbI_3$ cuboids with controlled size for high-efficiency perovskite solar cells. *Nature Nanotechnology* **9,** 927–932 (Nov. 2014).

52. Green, M. A., Hishikawa, Y., Dunlop, E. D., Levi, D. H., Hohl-Ebinger, J., Yoshita, M. & Ho-Baillie, A. W. Solar cell efficiency tables (Version 53). *Progress in Photovoltaics: Research and Applications* **27,** 3–12 (Jan. 2019).

53. Yang, M., Li, Z., Reese, M. O., Reid, O. G., Kim, D. H., Siol, S., Klein, T. R., Yan, Y., Berry, J. J., van Hest, M. F. A. M. & Zhu, K. Perovskite ink with wide processing window for scalable high-efficiency solar cells. *Nature Energy* **2,** 17038 (May 2017).

54. Tang, S., Deng, Y., Zheng, X., Bai, Y., Fang, Y., Dong, Q., Wei, H. & Huang, J. Composition Engineering in Doctor-Blading of Perovskite Solar Cells. *Advanced Energy Materials* **7,** 1700302 (Sept. 2017).

55. Kim, Y., Yassitepe, E., Voznyy, O., Comin, R., Walters, G., Gong, X., Kanjanaboos, P., Nogueira, A. F. & Sargent, E. H. Efficient Luminescence from Perovskite Quantum Dot Solids. *ACS Applied Materials & Interfaces* **7,** 25007–25013 (Nov. 2015).

56. Li, Z., Klein, T. R., Kim, D. H., Yang, M., Berry, J. J., van Hest, M. F. A. M. & Zhu, K. Scalable fabrication of perovskite solar cells. *Nature Reviews Materials* **3,** 18017 (Apr. 2018).

57. Ye, F., Chen, H., Xie, F., Tang, W., Yin, M., He, J., Bi, E., Wang, Y., Yang, X. & Han, L. Soft-cover deposition of scaling-up uniform perovskite thin films for high cost-performance solar cells. *Energy & Environmental Science* **9,** 2295–2301 (July 2016).

58. Liang, C., Li, P., Gu, H., Zhang, Y., Li, F., Song, Y., Shao, G., Mathews, N. & Xing, G. One-Step Inkjet Printed Perovskite in Air for Efficient Light Harvesting. *Solar RRL* **2,** 1700217 (Feb. 2018).

59. Bao, Z., Rogers, J. A. & Katz, H. E. Printable organic and polymeric semiconducting materials and devices. *Journal of Materials Chemistry* **9,** 1895–1904 (Jan. 1999).

60. Chen, H., Wei, Z., Zheng, X. & Yang, S. A scalable electrodeposition route to the low-cost, versatile and controllable fabrication of perovskite solar cells. *Nano Energy* **15,** 216–226 (July 2015).

61. Cui, X.-P., Jiang, K.-J., Huang, J.-H., Zhou, X.-Q., Su, M.-J., Li, S.-G., Zhang, Q.-Q., Yang, L.-M. & Song, Y.-L. Electrodeposition of PbO and its in situ conversion to $CH_3NH_3PbI_3$ for mesoscopic perovskite solar cells. *Chemical Communications* **51,** 1457–1460 (Jan. 2015).

62. Liao, H.-C., Guo, P., Hsu, C.-P., Lin, M., Wang, B., Zeng, L., Huang, W., Soe, C. M. M., Su, W.-F., Bedzyk, M. J., Wasielewski, M. R., Facchetti, A., Chang, R. P. H., Kanatzidis, M. G. & Marks, T. J. Enhanced Efficiency of Hot-Cast Large-Area Planar Perovskite Solar Cells/Modules Having Controlled Chloride Incorporation. *Advanced Energy Materials* **7,** 1601660 (Apr. 2017).

63. Lee, J.-W., Na, S.-I. & Kim, S.-S. Efficient spin-coating-free planar heterojunction perovskite solar cells fabricated with successive brush-painting. *Journal of Power Sources* **339,** 33–40 (Jan. 2017).

64. Im, J.-H., Lee, C.-R., Lee, J.-W., Park, S.-W. & Park, N.-G. 6.5% efficient perovskite quantum-dot-sensitized solar cell. *Nanoscale* **3,** 4088 (Oct. 2011).

65. Kim, H.-S., Lee, C.-R., Im, J.-H., Lee, K.-B., Moehl, T., Marchioro, A., Moon, S.-J., Humphry-Baker, R., Yum, J.-H., Moser, J. E., Grätzel, M. & Park, N.-G. Lead Iodide Perovskite Sensitized All-Solid-State Submicron Thin Film Mesoscopic Solar Cell with Efficiency Exceeding 9%. *Scientific Reports* **2,** 591 (Dec. 2012).

66. Noh, J. H., Im, S. H., Heo, J. H., Mandal, T. N. & Seok, S. I. Chemical Management for Colorful, Efficient, and Stable Inorganic-Organic Hybrid Nanostructured Solar Cells. *Nano Letters* **13,** 1764–1769 (Apr. 2013).

67. Cao, K., Cui, J., Zhang, H., Li, H., Song, J., Shen, Y., Cheng, Y. & Wang, M. Efficient mesoscopic perovskite solar cells based on the $CH_3NH_3$ $PbI_2Br$ light absorber. *Journal of Materials Chemistry A* **3,** 9116–9122 (Apr. 2015).

68. Ball, J. M., Lee, M. M., Hey, A. & Snaith, H. J. Low-temperature processed meso-superstructured to thin-film perovskite solar cells. *Energy & Environmental Science* **6,** 1739 (May 2013).

69. Zhou, H., Chen, Q., Li, G., Luo, S., Song, T.-b., Duan, H.-S., Hong, Z., You, J., Liu, Y. & Yang, Y. Photovoltaics. Interface engineering of highly efficient perovskite solar cells. *Science* **345,** 542–6 (Aug. 2014).

70. Liu, D., Yang, J. & Kelly, T. L. Compact Layer Free Perovskite Solar Cells with 13.5% Efficiency. *Journal of the American Chemical Society* **136,** 17116–17122 (Dec. 2014).

71. Yang, W. S., Noh, J. H., Jeon, N. J., Kim, Y. C., Ryu, S., Seo, J. & Seok, S. I. High-performance photovoltaic perovskite layers fabricated through intramolecular exchange. *Science* **348,** 1234–7 (June 2015).

72. Jung, E. H., Jeon, N. J., Park, E. Y., Moon, C. S., Shin, T. J., Yang, T.-Y., Noh, J. H. & Seo, J. Efficient, stable and scalable perovskite solar cells using poly(3-hexylthiophene). *Nature* **567,** 511–515 (Mar. 2019).

73. Jeon, N. J., Na, H., Jung, E. H., Yang, T.-Y., Lee, Y. G., Kim, G., Shin, H.-W., Il Seok, S., Lee, J. & Seo, J. A fluorene-terminated hole-transporting material for highly efficient and stable perovskite solar cells. *Nature Energy* **3,** 682–689 (Aug. 2018).

74. Kogo, A., Sanehira, Y., Numata, Y., Ikegami, M. & Miyasaka, T. Amorphous Metal Oxide Blocking Layers for Highly Efficient Low-Temperature Brookite $TiO_2$ -Based Perovskite Solar Cells. *ACS Applied Materials & Interfaces* **10,** 2224–2229 (Jan. 2018).

75. Protesescu, L., Yakunin, S., Bodnarchuk, M. I., Krieg, F., Caputo, R., Hendon, C. H., Yang, R. X., Walsh, A. & Kovalenko, M. V. Nanocrystals of Cesium Lead Halide Perovskites ($CsPbX_3$ , X = Cl, Br, and I): Novel Optoelectronic Materials Showing Bright Emission with Wide Color Gamut. *Nano Letters* **15,** 3692–3696 (June 2015).

76. Kumawat, N. K., Liu, X.-K., Kabra, D. & Gao, F. Blue perovskite light-emitting diodes: progress, challenges and future directions. *Nanoscale* **11,** 2109–2120 (Jan. 2019).

77. Murray, C. B., Norris, D. J. & Bawendi, M. G. Synthesis and characterization of nearly monodisperse CdE (E = sulfur, selenium, tellurium) semiconductor nanocrystallites. *Journal of the American Chemical Society* **115,** 8706–8715 (Sept. 1993).

78. Pan, A., He, B., Fan, X., Liu, Z., Urban, J. J., Alivisatos, A. P., He, L. & Liu, Y. Insight into the Ligand-Mediated Synthesis of Colloidal $CsPbBr_3$ Perovskite Nanocrystals: The Role of Organic Acid, Base, and Cesium Precursors. *ACS Nano* **10,** 7943–7954 (Aug. 2016).

79. Schmidt, L. C., Pertegás, A., González-Carrero, S., Malinkiewicz, O., Agouram, S., Mínguez Espallargas, G., Bolink, H. J., Galian, R. E. & Pérez-Prieto, J. Nontemplate Synthesis of $CH_3NH_3PbBr_3$ Perovskite Nanoparticles. *Journal of the American Chemical Society* **136,** 850–853 (Jan. 2014).

80. Luo, B., Pu, Y.-C., Yang, Y., Lindley, S. A., Abdelmageed, G., Ashry, H., Li, Y., Li, X. & Zhang, J. Z. Synthesis, Optical Properties, and Exciton Dynamics of Organolead Bromide Perovskite Nanocrystals. *The Journal of Physical Chemistry C* **119,** 26672–26682 (Nov. 2015).

81. Luo, B., Pu, Y.-C., Lindley, S. A., Yang, Y., Lu, L., Li, Y., Li, X. & Zhang, J. Z. Organolead Halide Perovskite Nanocrystals: Branched Capping Ligands Control Crystal Size and Stability. *Angewandte Chemie International Edition* **55,** 8864–8868 (July 2016).

82. Zhao, Y. S., Fu, H., Peng, A., Ma, Y., Xiao, D. & Yao, J. Low-Dimensional Nanomaterials Based on Small Organic Molecules: Preparation and Optoelectronic Properties. *Advanced Materials* **20,** 2859–2876 (Aug. 2008).

83. Zhang, F., Huang, S., Wang, P., Chen, X., Zhao, S., Dong, Y. & Zhong, H. Colloidal Synthesis of Air-Stable $CH_3NH_3PbI_3$ Quantum Dots by Gaining Chemical Insight into the Solvent Effects. *Chemistry of Materials* **29,** 3793–3799 (Apr. 2017).

84. Zhang, F., Chen, C., Kershaw, S. V., Xiao, C., Han, J., Zou, B., Wu, X., Chang, S., Dong, Y., Rogach, A. L. & Zhong, H. Ligand-Controlled Formation and Photoluminescence Properties of $CH_3NH_3PbBr_3$ Nanocubes and Nanowires. *ChemNanoMat* **3,** 303–310 (May 2017).

85. Zhang, Q. & Yin, Y. All-Inorganic Metal Halide Perovskite Nanocrystals: Opportunities and Challenges. *ACS Central Science* **4,** 668–679 (June 2018).

86. Sanehira, E. M., Marshall, A. R., Christians, J. A., Harvey, S. P., Ciesielski, P. N., Wheeler, L. M., Schulz, P., Lin, L. Y., Beard, M. C. & Luther, J. M. Enhanced mobility $CsPbI_3$ quantum dot arrays for record-efficiency, high-voltage photovoltaic cells. *Science Advances* **3,** eaao4204 (Oct. 2017).

87. Swarnkar, A., Marshall, A. R., Sanehira, E. M., Chernomordik, B. D., Moore, D. T., Christians, J. A., Chakrabarti, T. & Luther, J. M. Quantum dot-induced phase stabilization of $\alpha$-$CsPbI_3$ perovskite for high-efficiency photovoltaics. *Science* **354,** 92–95 (Oct. 2016).

88. Song, J., Li, J., Li, X., Xu, L., Dong, Y. & Zeng, H. Quantum Dot Light-Emitting Diodes Based on Inorganic Perovskite Cesium Lead Halides ($CsPbX_3$. *Advanced Materials* **27,** 7162–7167 (Nov. 2015).

89. Li, J., Xu, L., Wang, T., Song, J., Chen, J., Xue, J., Dong, Y., Cai, B., Shan, Q., Han, B. & Zeng, H. 50-Fold EQE Improvement up to 6.27% of Solution-Processed All-Inorganic Perovskite $CsPbBr_3$ QLEDs via Surface Ligand Density Control. *Advanced Materials* **29,** 1603885 (Feb. 2017).

90. Yakunin, S., Protesescu, L., Krieg, F., Bodnarchuk, M. I., Nedelcu, G., Humer, M., De Luca, G., Fiebig, M., Heiss, W. & Kovalenko, M. V. Low-threshold amplified spontaneous emission and lasing from colloidal nanocrystals of caesium lead halide perovskites. *Nature Communications* **6,** 8056 (Nov. 2015).

91. Wang, Y., Li, X., Zhao, X., Xiao, L., Zeng, H. & Sun, H. Nonlinear Absorption and Low-Threshold Multiphoton Pumped Stimulated Emission from All-Inorganic Perovskite Nanocrystals. *Nano Letters* **16,** 448–453 (Jan. 2016).

92. Gao, Y., Wang, S., Huang, C., Yi, N., Wang, K., Xiao, S. & Song, Q. Room temperature three-photon pumped $CH_3NH_3PbBr_3$ perovskite microlasers. *Scientific Reports* **7,** 45391 (June 2017).

93. Park, Y.-S., Guo, S., Makarov, N. S. & Klimov, V. I. Room Temperature Single-Photon Emission from Individual Perovskite Quantum Dots. *ACS Nano* **9,** 10386–10393 (Oct. 2015).

94. Pan, R., Li, H., Wang, J., Jin, X., Li, Q., Wu, Z., Gou, J., Jiang, Y. & Song, Y. High-Responsivity Photodetectors Based on Formamidinium Lead Halide Perovskite Quantum Dot-Graphene Hybrid. *Particle & Particle Systems Characterization* **35,** 1700304 (Apr. 2018).

95. Stoumpos, C. C., Malliakas, C. D. & Kanatzidis, M. G. Semiconducting Tin and Lead Iodide Perovskites with Organic Cations: Phase Transitions, High Mobilities, and Near-Infrared Photoluminescent Properties. *Inorganic Chemistry* **52,** 9019–9038 (Aug. 2013).

96. Chen, Z., Wang, J. J., Ren, Y., Yu, C. & Shum, K. Schottky solar cells based on $CsSnI_3$ thin-films. *Applied Physics Letters* **101,** 093901 (Aug. 2012).

97. Noel, N. K., Stranks, S. D., Abate, A., Wehrenfennig, C., Guarnera, S., Haghighirad, A.-A., Sadhanala, A., Eperon, G. E., Pathak, S. K., Johnston, M. B., Petrozza, A., Herz, L. M. & Snaith, H. J. Lead-free organic-inorganic tin halide perovskites for photovoltaic applications. *Energy Environ. Sci.* **7,** 3061–3068 (Aug. 2014).

98. Hao, F., Stoumpos, C. C., Cao, D. H., Chang, R. P. H. & Kanatzidis, M. G. Lead-free solid-state organic-inorganic halide perovskite solar cells. *Nature Photonics* **8,** 489–494 (June 2014).

99. Konstantakou, M. & Stergiopoulos, T. A critical review on tin halide perovskite solar cells. *Journal of Materials Chemistry A* **5,** 11518–11549 (June 2017).

100. Shao, S., Liu, J., Portale, G., Fang, H.-H., Blake, G. R., ten Brink, G. H., Koster, L. J. A. & Loi, M. A. Highly Reproducible Sn-Based Hybrid Perovskite Solar Cells with 9% Efficiency. *Advanced Energy Materials* **8,** 1702019 (Feb. 2018).

101. Song, T.-B., Yokoyama, T., Stoumpos, C. C., Logsdon, J., Cao, D. H., Wasielewski, M. R., Aramaki, S. & Kanatzidis, M. G. Importance of Reducing Vapor Atmosphere in the Fabrication of Tin-Based Perovskite Solar Cells. *Journal of the American Chemical Society* **139,** 836–842 (Jan. 2017).

102. Marshall, K. P., Walker, M., Walton, R. I. & Hatton, R. A. Enhanced stability and efficiency in hole-transport-layer-free $CsSnI_3$ perovskite photovoltaics. *Nature Energy* **1,** 16178 (Dec. 2016).

103. Tang, L.-C., Chang, Y.-C., Huang, J.-Y., Lee, M.-H. & Chang, C.-S. First Principles Calculations of Linear and Second-Order Optical Responses in Rhombohedrally Distorted Perovskite Ternary Halides, $CsGeX_3$ (X = Cl, Br, and I). *Japanese Journal of Applied Physics* **48,** 112402 (Nov. 2009).

104. Krishnamoorthy, T., Ding, H., Yan, C., Leong, W. L., Baikie, T., Zhang, Z., Sherburne, M., Li, S., Asta, M., Mathews, N. & Mhaisalkar, S. G. Lead-free germanium iodide perovskite materials for photovoltaic applications. *Journal of Materials Chemistry A* **3,** 23829–23832 (Nov. 2015).

105. Stoumpos, C. C., Frazer, L., Clark, D. J., Kim, Y. S., Rhim, S. H., Freeman, A. J., Ketterson, J. B., Jang, J. I. & Kanatzidis, M. G. Hybrid Germanium Iodide Perovskite Semiconductors: Active Lone Pairs, Structural Distortions, Direct and Indirect Energy Gaps, and Strong Nonlinear Optical Properties. *Journal of the American Chemical Society* **137,** 6804–6819 (June 2015).

106. Wang, J., Zhang, C., Liu, H., McLaughlin, R., Zhai, Y., Vardeny, S. R., Liu, X., McGill, S., Semenov, D., Guo, H., Tsuchikawa, R., Deshpande, V. V., Sun, D. & Vardeny, Z. V. Spin-optoelectronic devices based on hybrid organic-inorganic trihalide perovskites. *Nature Communications* **10,** 129 (Dec. 2019).

107. Odenthal, P., Talmadge, W., Gundlach, N., Wang, R., Zhang, C., Sun, D., Yu, Z.-G., Valy Vardeny, Z. & Li, Y. S. Spin-polarized exciton quantum beating in hybrid organic-inorganic perovskites. *Nature Physics* **13,** 894–899 (Sept. 2017).

108. Walter, M. G., Warren, E. L., McKone, J. R., Boettcher, S. W., Mi, Q., Santori, E. A. & Lewis, N. S. Solar Water Splitting Cells. *Chemical Reviews* **110,** 6446–6473 (Nov. 2010).

109. Luo, J., Im, J.-H., Mayer, M. T., Schreier, M., Nazeeruddin, M. K., Park, N.-G., Tilley, S. D., Fan, H. J. & Grätzel, M. Water photolysis at 12.3% efficiency via perovskite photovoltaics and Earth-abundant catalysts. *Science* **345,** 1593–6 (Sept. 2014).

110. Moniruddin, M., Ilyassov, B., Zhao, X., Smith, E., Serikov, T., Ibrayev, N., Asmatulu, R. & Nuraje, N. Recent progress on perovskite materials in photovoltaic and water splitting applications. *Materials Today Energy* **7,** 246–259 (Mar. 2018).

111. Gerrish, V. M. Characterization and Quantification of Detector Performance. *Semiconductors and Semimetals* **43,** 493–530 (Jan. 1995).

112. Sarang, S., Ishihara, H., Chen, Y.-C., Lin, O., Gopinathan, A., Tung, V. C. & Ghosh, S. Low temperature excitonic spectroscopy and dynamics as a probe of quality in hybrid perovskite thin films. *Physical Chemistry Chemical Physics* **18,** 28428–28433 (Oct. 2016).

113. *Principles of Fluorescence Spectroscopy* (ed Lakowicz, J. R.) doi:10.1007/978-0-387-46312-4. http://link.springer.com/10.1007/978-0-387-46312-4 (Springer US, Boston, MA, 2006).

114. Perkampus, H.-H. *UV-VIS Spectroscopy and Its Applications* doi:10.1007/978-3-642-77477-5. http://link.springer.com/10.1007/978-3-642-77477-5 (Springer Berlin Heidelberg, Berlin, Heidelberg, 1992).

115. Felser, C. & Fecher, G. H. *Spintronics : from materials to devices* (Springer, 2013).

116. Kutz, M. *Handbook of measurement in science and engineering* (John Wiley & Sons, 2013).

117. *Photovoltaic Solar Energy* (eds Reinders, A., Verlinden, P., van Sark, W. & Freundlich, A.) doi:10.1002/9781118927496. http://doi.wiley.com/10.1002/9781118927496 (John Wiley & Sons, Ltd, Chichester, UK, Dec. 2016).

118. Meier, F. & Zakharchenya, B. P. *Optical Orientation, Modern Problems in Condensed Matter Sciences* 536 (Elsevier Science, 1984).

119. Liang, K., Mitzi, D. B. & Prikas, M. T. Synthesis and Characterization of Organic-Inorganic Perovskite Thin Films Prepared Using a Versatile Two-Step Dipping Technique. *Chemistry of Materials.* doi:10.1021/CM970568F. https://pubs.acs.org/doi/10.1021/cm970568f (1998).

120. Chen, Q., Zhou, H., Hong, Z., Luo, S., Duan, H.-S., Wang, H.-H., Liu, Y., Li, G. & Yang, Y. Planar Heterojunction Perovskite Solar Cells via Vapor-Assisted Solution Process. *Journal of the American Chemical Society* **136,** 622–625 (Jan. 2014).

121. Hyun Kim, G., Zucker, R. V., Ye, J., Craig Carter, W. & Thompson, C. V. Quantitative analysis of anisotropic edge retraction by solid-state dewetting of thin single crystal films. *Journal of Applied Physics* **113,** 043512 (Jan. 2013).

122. Sun, S., Salim, T., Mathews, N., Duchamp, M., Boothroyd, C., Xing, G., Sum, T. C. & Lam, Y. M. The origin of high efficiency in low-temperature solution-processable bilayer organometal halide hybrid solar cells. *Energy Environ. Sci.* **7,** 399–407 (Dec. 2014).

123. Stranks, S. D., Eperon, G. E., Grancini, G., Menelaou, C., Alcocer, M. J. P., Leijtens, T., Herz, L. M., Petrozza, A. & Snaith, H. J. Electron-hole diffusion lengths exceeding 1 micrometer in an organometal trihalide perovskite absorber. *Science* **342,** 341–4 (Oct. 2013).

124. Tan, Z.-K., Moghaddam, R. S., Lai, M. L., Docampo, P., Higler, R., Deschler, F., Price, M., Sadhanala, A., Pazos, L. M., Credgington, D., Hanusch, F., Bein, T., Snaith, H. J. & Friend, R. H. Bright light-emitting diodes based on organometal halide perovskite. *Nature Nanotechnology* **9,** 687–692 (Sept. 2014).

125. McGehee, M. D. Fast-track solar cells. *Nature* **501,** 323–325 (Sept. 2013).

126. Conings, B., Baeten, L., De Dobbelaere, C., D'Haen, J., Manca, J. & Boyen, H.-G. Perovskite-Based Hybrid Solar Cells Exceeding 10% Efficiency with High Reproducibility Using a Thin Film Sandwich Approach. *Advanced Materials* **26,** 2041–2046 (Apr. 2014).

127. Wang, Q., Shao, Y., Dong, Q., Xiao, Z., Yuan, Y. & Huang, J. Large fill-factor bilayer iodine perovskite solar cells fabricated by a low-temperature solution-process. *Energy Environ. Sci.* **7,** 2359–2365 (June 2014).

128. Jeon, N. J., Noh, J. H., Kim, Y. C., Yang, W. S., Ryu, S. & Seok, S. I. Solvent engineering for high-performance inorganic-organic hybrid perovskite solar cells. *Nature Materials* **13,** 897–903 (Sept. 2014).

129. Nie, W., Tsai, H., Asadpour, R., Blancon, J.-C., Neukirch, A. J., Gupta, G., Crochet, J. J., Chhowalla, M., Tretiak, S., Alam, M. A., Wang, H.-L. & Mohite, A. D. Solar cells. High-efficiency solution-processed perovskite solar cells with millimeter-scale grains. *Science* **347,** 522–5 (Jan. 2015).

130. Chen, L.-M., Hong, Z., Kwan, W. L., Lu, C.-H., Lai, Y.-F., Lei, B., Liu, C.-P. & Yang, Y. Multi-Source/Component Spray Coating for Polymer Solar Cells. *ACS Nano* **4,** 4744–4752 (Aug. 2010).

131. Mei, A., Li, X., Liu, L., Ku, Z., Liu, T., Rong, Y., Xu, M., Hu, M., Chen, J., Yang, Y., Grätzel, M. & Han, H. A hole-conductor-free, fully printable mesoscopic perovskite solar cell with high stability. *Science* **345,** 295–8 (July 2014).

132. Barrows, A. T., Pearson, A. J., Kwak, C. K., Dunbar, A. D. F., Buckley, A. R. & Lidzey, D. G. Efficient planar heterojunction mixed-halide perovskite solar cells deposited via spray-deposition. *Energy Environ. Sci.* **7,** 2944–2950 (Aug. 2014).

133. Deegan, R. D., Bakajin, O., Dupont, T. F., Huber, G., Nagel, S. R. & Witten, T. A. Capillary flow as the cause of ring stains from dried liquid drops. *Nature* **389,** 827–829 (Oct. 1997).

134. Huang, J., Kim, F., Tao, A. R., Connor, S. & Yang, P. Spontaneous formation of nanoparticle stripe patterns through dewetting. *Nature Materials* **4,** 896–900 (Dec. 2005).

135. Xiao, Z., Bi, C., Shao, Y., Dong, Q., Wang, Q., Yuan, Y., Wang, C., Gao, Y. & Huang, J. Efficient, high yield perovskite photovoltaic devices grown by interdiffusion of solution-processed precursor stacking layers. *Energy Environ. Sci.* **7,** 2619–2623 (July 2014).

136. Kim, D., Giermann, A. L. & Thompson, C. V. Solid-state dewetting of patterned thin films. *Applied Physics Letters* **95,** 251903 (Dec. 2009).

137. Ye, Y., Dai, Y., Dai, L., Shi, Z., Liu, N., Wang, F., Fu, L., Peng, R., Wen, X., Chen, Z., Liu, Z. & Qin, G. High-Performance Single CdS Nanowire (Nanobelt) Schottky Junction Solar Cells with Au/Graphene Schottky Electrodes. *ACS Applied Materials & Interfaces* **2,** 3406–3410 (Dec. 2010).

138. Kovalenko, O., Greer, J. & Rabkin, E. Solid-state dewetting of thin iron films on sapphire substrates controlled by grain boundary diffusion. *Acta Materialia* **61,** 3148–3156 (May 2013).

139. Kosinova, A., Klinger, L., Kovalenko, O. & Rabkin, E. The role of grain boundary sliding in solid-state dewetting of thin polycrystalline films. *Scripta Materialia* **82,** 33–36 (July 2014).

140. Ye, J. Investigation of the mechanism of solid-state dewetting of silver thin films using spatial correlation analysis of hole patterns. *Applied Physics Express* **7,** 085601 (Aug. 2014).

141. Yarin, A. L. & Weiss, D. A. Impact of drops on solid surfaces: self-similar capillary waves, and splashing as a new type of kinematic discontinuity. *Journal of Fluid Mechanics* **283,** 141–173 (Jan. 1995).

142. Jaworek, A. & Sobczyk, A. Electrospraying route to nanotechnology: An overview. *Journal of Electrostatics* **66,** 197–219 (Mar. 2008).

143. D'Arcy, J. M., Tran, H. D., Tung, V. C., Tucker-Schwartz, A. K., Wong, R. P., Yang, Y. & Kaner, R. B. Versatile solution for growing thin films of conducting polymers. *Proceedings of the National Academy of Sciences of the United States of America* **107,** 19673–8 (Nov. 2010).

144. Kaltenbrunner, M., Adam, G., Głowacki, E. D., Drack, M., Schwödiauer, R., Leonat, L., Apaydin, D. H., Groiss, H., Scharber, M. C., White, M. S., Sariciftci, N. S. & Bauer, S. Flexible high power-per-weight perovskite solar cells with chromium oxide-metal contacts for improved stability in air. *Nature Materials* **14,** 1032–1039 (Oct. 2015).

145. Li, G., Shrotriya, V., Huang, J., Yao, Y., Moriarty, T., Emery, K. & Yang, Y. High-efficiency solution processable polymer photovoltaic cells by self-organization of polymer blends. *Nature Materials* **4,** 864–868 (Nov. 2005).

146. Mansfield, E., Ross, E. E., D'Ambruoso, G. D., Keogh, J. P., Huang, Y. & Aspinwall, C. A. Fabrication and Characterization of Spatially Defined, Multiple Component, Chemically Functionalized Domains in Enclosed Silica Channels Using Cross-Linked Phospholipid Membranes. *Langmuir* **23,** 11326–11333 (Oct. 2007).

147. Tidhar, Y., Edri, E., Weissman, H., Zohar, D., Hodes, G., Cahen, D., Rybtchinski, B. & Kirmayer, S. Crystallization of Methyl Ammonium Lead Halide Perovskites: Implications for Photovoltaic Applications. *Journal of the American Chemical Society* **136,** 13249–13256 (Sept. 2014).

148. DeQuilettes, D. W., Vorpahl, S. M., Stranks, S. D., Nagaoka, H., Eperon, G. E., Ziffer, M. E., Snaith, H. J. & Ginger, D. S. Solar cells. Impact of microstructure on local carrier lifetime in perovskite solar cells. *Science* **348,** 683–6 (May 2015).

149. Xie, F. X., Zhang, D., Su, H., Ren, X., Wong, K. S., Grätzel, M. & Choy, W. C. H. Vacuum-Assisted Thermal Annealing of $CH_3NH_3PbI_3$ for Highly Stable and Efficient Perovskite Solar Cells. *ACS Nano* **9,** 639–646 (Jan. 2015).

150. Zhou, J., Liu, Q., Feng, W., Sun, Y. & Li, F. Upconversion Luminescent Materials: Advances and Applications. *Chemical Reviews* **115,** 395–465 (Jan. 2015).

151. Kim, H.-S., Mora-Sero, I., Gonzalez-Pedro, V., Fabregat-Santiago, F., Juarez-Perez, E. J., Park, N.-G. & Bisquert, J. Mechanism of carrier accumulation in perovskite thin-absorber solar cells. *Nature Communications* **4,** 2242 (Oct. 2013).

152. Wehrenfennig, C., Eperon, G. E., Johnston, M. B., Snaith, H. J. & Herz, L. M. High Charge Carrier Mobilities and Lifetimes in Organolead Trihalide Perovskites. *Advanced Materials* **26,** 1584–1589 (Mar. 2014).

153. Ponseca, C. S., Savenije, T. J., Abdellah, M., Zheng, K., Yartsev, A., Pascher, T., Harlang, T., Chabera, P., Pullerits, T., Stepanov, A., Wolf, J.-P. & Sundström, V. Organometal Halide Perovskite Solar Cell Materials Rationalized: Ultrafast Charge Generation, High and Microsecond-Long Balanced Mobilities, and Slow Recombination. *Journal of the American Chemical Society* **136,** 5189–5192 (Apr. 2014).

154. Dar, M. I., Arora, N., Gao, P., Ahmad, S., Grätzel, M. & Nazeeruddin, M. K. Investigation Regarding the Role of Chloride in Organic-Inorganic Halide Perovskites Obtained from Chloride Containing Precursors. *Nano Letters* **14,** 6991–6996 (Dec. 2014).

155. Snaith, H. & Schmidt-Mende, L. Preface: Special Topic on Perovskite Solar Cells. *APL Materials* **2,** 081201 (Aug. 2014).

156. Abate, A., Saliba, M., Hollman, D. J., Stranks, S. D., Wojciechowski, K., Avolio, R., Grancini, G., Petrozza, A. & Snaith, H. J. Supramolecular Halogen Bond Passivation of Organic-Inorganic Halide Perovskite Solar Cells. *Nano Letters* **14,** 3247–3254 (June 2014).

157. Troughton, J., Charbonneau, C., Carnie, M. J., Davies, M. L., Worsley, D. A. & Watson, T. M. Rapid processing of perovskite solar cells in under 2.5 seconds. *Journal of Materials Chemistry A* **3,** 9123–9127 (Apr. 2015).

158. Yamada, Y., Nakamura, T., Endo, M., Wakamiya, A. & Kanemitsu, Y. Photocarrier Recombination Dynamics in Perovskite $CH_3NH_3PbI_3$ for Solar Cell Applications. *Journal of the American Chemical Society* **136,** 11610–11613 (Aug. 2014).

159. Deschler, F., Price, M., Pathak, S., Klintberg, L. E., Jarausch, D.-D., Higler, R., Hüttner, S., Leijtens, T., Stranks, S. D., Snaith, H. J., Atatüre, M., Phillips, R. T. & Friend, R. H. High Photoluminescence Efficiency and Optically Pumped Lasing in Solution-Processed Mixed Halide Perovskite Semiconductors. *The Journal of Physical Chemistry Letters* **5,** 1421–1426 (Apr. 2014).

160. Wehrenfennig, C., Liu, M., Snaith, H. J., Johnston, M. B. & Herz, L. M. Charge carrier recombination channels in the low-temperature phase of organic-inorganic lead halide perovskite thin films. *APL Materials* **2,** 081513 (Aug. 2014).

161. Hsiao, Y.-C., Wu, T., Li, M., Liu, Q., Qin, W. & Hu, B. Fundamental physics behind high-efficiency organo-metal halide perovskite solar cells. *Journal of Materials Chemistry A* **3,** 15372–15385 (July 2015).

162. Kong, W., Ye, Z., Qi, Z., Zhang, B., Wang, M., Rahimi-Iman, A. & Wu, H. Characterization of an abnormal photoluminescence behavior upon crystal-phase transition of perovskite $CH_3NH_3PbI_3$. *Physical Chemistry Chemical Physics* **17,** 16405–16411 (June 2015).

163. Wehrenfennig, C., Liu, M., Snaith, H. J., Johnston, M. B. & Herz, L. M. Charge carrier recombination channels in the low-temperature phase of organic-inorganic lead halide perovskite thin films. *APL Materials* **2,** 081513 (Aug. 2014).

164. Wu, K., Bera, A., Ma, C., Du, Y., Yang, Y., Li, L. & Wu, T. Temperature-dependent excitonic photoluminescence of hybrid organometal halide perovskite films. *Phys. Chem. Chem. Phys.* **16,** 22476–22481 (Sept. 2014).

165. Li, Y., Yan, W., Li, Y., Wang, S., Wang, W., Bian, Z., Xiao, L. & Gong, Q. Direct Observation of Long Electron-Hole Diffusion Distance in $CH_3NH_3PbI_3$ Perovskite Thin Film. *Scientific Reports* **5,** 14485 (Nov. 2015).

166. D'Innocenzo, V., Grancini, G., Alcocer, M. J. P., Kandada, A. R. S., Stranks, S. D., Lee, M. M., Lanzani, G., Snaith, H. J. & Petrozza, A. Excitons versus free charges in organo-lead tri-halide perovskites. *Nature Communications* **5,** 3586 (May 2014).

167. Miyata, A., Mitioglu, A., Plochocka, P., Portugall, O., Wang, J. T.-W., Stranks, S. D., Snaith, H. J. & Nicholas, R. J. Direct measurement of the exciton binding energy and effective masses for charge carriers in organicfffdfffdfffdinorganic tri-halide perovskites. *Nature Physics* **11,** 582–587 (July 2015).

168. Ishihara, H., Chen, W., Chen, Y.-C., Sarang, S., De Marco, N., Lin, O., Ghosh, S. & Tung, V. Electrohydrodynamically Assisted Deposition of Efficient Perovskite Photovoltaics. *Advanced Materials Interfaces* **3,** 1500762 (May 2016).

169. Yamada, Y., Yasuda, H., Tayagaki, T. & Kanemitsu, Y. Temperature Dependence of Photoluminescence Spectra of Nondoped and Electron-Doped $SrTiO_3$ : Crossover from Auger Recombination to Single-Carrier Trapping. *Physical Review Letters* **102,** 247401 (June 2009).

170. Ehm, L., Borkowski, L. A., Parise, J. B., Ghose, S. & Chen, Z. Evidence of tetragonal nanodomains in the high-pressure polymorph of BaTiO3. *Applied Physics Letters* **98,** 021901 (Jan. 2011).

171. Chang, S.-Z., Chang, T.-C., Shen, J.-L., Lee, S.-C. & Chen, Y.-F. Material and electrical properties of highly mismatched $In_xGa_{1-x}As$ on GaAs by molecularfffdfffdfffdbeam epitaxy. *Journal of Applied Physics* **74,** 6912–6918 (Dec. 1993).

172. Benia, H.-M., Myrach, P., Gonchar, A., Risse, T., Nilius, N. & Freund, H.-J. Electron trapping in misfit dislocations of MgO thin films. *Physical Review B* **81,** 241415 (June 2010).

173. Lunz, M., Bradley, A. L., Gerard, V. A., Byrne, S. J., Gun'ko, Y. K., Lesnyak, V. & Gaponik, N. Concentration dependence of Förster resonant energy transfer between donor and acceptor nanocrystal quantum dot layers: Effect of donor-donor interactions. *Physical Review B* **83,** 115423 (Mar. 2011).

174. Cingolani, R., Calcagnile, L., Colí, G., Rinaldi, R., Lomoscolo, M., DiDio, M., Franciosi, A., Vanzetti, L., LaRocca, G. C. & Campi, D. Radiative recombination processes in wide-band-gap II-VI quantum wells: the interplay between excitons and free carriers. *Journal of the Optical Society of America B* **13,** 1268 (June 1996).

175. Saha, M. N. On a Physical Theory of Stellar Spectra. *Proceedings of the Royal Society A: Mathematical, Physical and Engineering Sciences* **99,** 135–153 (May 1921).

176. Atkins, P. W., Julio, D. P. & Keeler, J. *Atkins' Physical chemistry* 11th ed., 1040 (2018).

177. Ergen, O., Gilbert, S., Pham, T., Turner, S., Tan, M., Worsley, M. & Zettl, A. Graded bandgap perovskite solar cells. *Nature Materials* **16,** 522–525 (Nov. 2016).

178. Shi, Z., Li, Y., Zhang, Y., Chen, Y., Li, X., Wu, D., Xu, T., Shan, C. & Du, G. High-Efficiency and Air-Stable Perovskite Quantum Dots Light-Emitting Diodes with an All-Inorganic Heterostructure. *Nano Letters* **17,** 313–321 (Jan. 2017).

179. Huang, H., Zhao, F., Liu, L., Zhang, F., Wu, X. G., Shi, L., Zou, B., Pei, Q. & Zhong, H. Emulsion Synthesis of Size-Tunable $CH_3NH_3PbBr_3$ Quantum Dots: An Alternative Route toward Efficient Light-Emitting Diodes. *ACS Applied Materials and Interfaces* **7,** 28128–28133 (2015).

180. Zhu, H., Fu, Y., Meng, F., Wu, X., Gong, Z., Ding, Q., Gustafsson, M. V., Trinh, M. T., Jin, S. & Zhu, X.-Y. Lead halide perovskite nanowire lasers with low lasing thresholds and high quality factors. *Nature Materials* **14,** 636–642 (June 2015).

181. Berhe, T. A., Su, W.-N., Chen, C.-H., Pan, C.-J., Cheng, J.-H., Chen, H.-M., Tsai, M.-C., Chen, L.-Y., Dubale, A. A. & Hwang, B.-J. Organometal halide perovskite solar cells: degradation and stability. *Energy & Environmental Science* **9,** 323–356 (Feb. 2016).

182. Sutherland, B. R. & Sargent, E. H. Perovskite photonic sources. *Nature Photonics* **10,** 295–302 (May 2016).

183. Nikolaidou, K., Sarang, S., Hoffman, C., Mendewala, B., Ishihara, H., Lu, J. Q., Ilan, B., Tung, V. & Ghosh, S. Hybrid Perovskite Thin Films as Highly Efficient Luminescent Solar Concentrators. *Advanced Optical Materials* **4,** 2126–2132 (Dec. 2016).

184. Zhao, H., Zhou, Y., Benetti, D., Ma, D. & Rosei, F. Perovskite quantum dots integrated in large-area luminescent solar concentrators. *Nano Energy* **37,** 214–223 (July 2017).

185. Boles, M. A., Ling, D., Hyeon, T. & Talapin, D. V. The surface science of nanocrystals. *Nature Materials* **15,** 141–153 (Feb. 2016).

186. Sheng, R., Ho-Baillie, A., Huang, S., Chen, S., Wen, X., Hao, X. & Green, M. A. Methylammonium Lead Bromide Perovskite-Based Solar Cells by Vapor-Assisted Deposition. *The Journal of Physical Chemistry C* **119,** 3545–3549 (Feb. 2015).

187. Zheng, X., Wu, C., Jha, S. K., Li, Z., Zhu, K. & Priya, S. Improved Phase Stability of Formamidinium Lead Triiodide Perovskite by Strain Relaxation. *ACS Energy Letters* **1,** 1014–1020 (Nov. 2016).

188. Ye, T., Ma, S., Jiang, X., Wei, L., Vijila, C. & Ramakrishna, S. Performance Enhancement of Tri-Cation and Dual-Anion Mixed Perovskite Solar Cells by Au@$SiO_2$ Nanoparticles. *Advanced Functional Materials* **27,** 1–9 (2017).

189. Liang, Z., Zhao, S., Xu, Z., Qiao, B., Song, P., Gao, D. & Xu, X. Shape-Controlled Synthesis of All-Inorganic $CsPbBr_3$ Perovskite Nanocrystals with Bright Blue Emission. *ACS Applied Materials & Interfaces* **8,** 28824–28830 (Oct. 2016).

190. Sichert, J. A., Tong, Y., Mutz, N., Vollmer, M., Fischer, S., Milowska, K. Z., García Cortadella, R., Nickel, B., Cardenas-Daw, C., Stolarczyk, J. K., Urban, A. S. & Feldmann, J. Quantum Size Effect in Organometal Halide Perovskite Nanoplatelets. *Nano Letters* **15,** 6521–6527 (Oct. 2015).

191. Wright, A. D., Verdi, C., Milot, R. L., Eperon, G. E., Pérez-Osorio, M. A., Snaith, H. J., Giustino, F., Johnston, M. B. & Herz, L. M. Electron-phonon coupling in hybrid lead halide perovskites. *Nature Communications* **7,** 11755 (Sept. 2016).

192. Dai, J., Zheng, H., Zhu, C., Lu, J. & Xu, C. Comparative Investigation on The Temperature-Dependent Photoluminescence of $CH_3NH_3PbBr_x$ and $CH_3(NH_2)_2PbBr_3$ microstructures. *J. Mater. Chem. C* **4,** 4408–4413 (2016).

193. McHale, J. M., Navrotsky, A. & Perrotta, A. J. Effects of Increased Surface Area and Chemisorbed $H_2O$ on the Relative Stability of Nanocrystalline $\gamma - Al_2O_3$ and $\alpha - Al_2O_3$. *The Journal of Physical Chemistry B* **101,** 603–613 (1997).

194. Wang, F., Han, Y., Lim, C. S., Lu, Y., Wang, J., Xu, J., Chen, H., Zhang, C., Hong, M. & Liu, X. Simultaneous phase and size control of upconversion nanocrystals through lanthanide doping. *Nature* **463,** 1061–1065 (Feb. 2010).

195. Zhang, Y., Liu, J., Wang, Z., Xue, Y., Ou, Q., Polavarapu, L., Zheng, J., Qi, X. & Bao, Q. Synthesis, properties, and optical applications of low-dimensional perovskites. *Chemical Communications* **52,** 13637–13655 (Nov. 2016).

196. Ledinský, M., Löper, P., Niesen, B., Holovský, J., Moon, S.-J., Yum, J.-H., De Wolf, S., Fejfar, A. & Ballif, C. Raman Spectroscopy of Organic-Inorganic Halide Perovskites. *The Journal of Physical Chemistry Letters* **6,** 401–406 (Feb. 2015).

197. Matsuishi, K., Ishihara, T., Onari, S., Chang, Y. H. & Park, C. H. Optical properties and structural phase transitions of lead-halide based inorganic-organic 3D and 2D perovskite semiconductors under high pressure. *physica status solidi (b)* **241,** 3328–3333 (Nov. 2004).

198. Lee, K. B., Siegel, J., Webb, S., Lévêque-Fort, S., Cole, M., Jones, R., Dowling, K., Lever, M. & French, P. Application of the Stretched Exponential Function to Fluorescence Lifetime Imaging. *Biophysical Journal* **81,** 1265–1274 (Sept. 2001).

199. Li, J., Yuan, X., Jing, P., Li, J., Wei, M., Hua, J., Zhao, J. & Tian, L. Temperature-dependent photoluminescence of inorganic perovskite nanocrystal films. *RSC Adv.* **6,** 78311–78316 (2016).

200. Luckert, F., Yakushev, M. V., Faugeras, C., Karotki, A. V., Mudryi, A. V. & Martin, R. W. Excitation power and temperature dependence of excitons in $CuInSe_2$. *Journal of Applied Physics* **111,** 093507 (May 2012).

201. He, H., Yu, Q., Li, H., Li, J., Si, J., Jin, Y., Wang, N., Wang, J., He, J., Wang, X., Zhang, Y. & Ye, Z. Exciton localization in solution-processed organolead trihalide perovskites. *Nature Communications* **7,** 10896 (Apr. 2016).

202. Wang, K., Li, G., Wang, S., Liu, S., Sun, W., Huang, C., Wang, Y., Song, Q. & Xiao, S. Dark-Field Sensors based on Organometallic Halide Perovskite Microlasers. *Advanced Materials* **30,** 1801481 (Aug. 2018).

203. Zhang, M., Zhang, F., Wang, Y., Zhu, L., Hu, Y., Lou, Z., Hou, Y. & Teng, F. High-Performance Photodiode-Type Photodetectors Based on Polycrystalline Formamidinium Lead Iodide Perovskite Thin Films. *Scientific Reports* **8,** 11157 (Dec. 2018).

204. Etienne, T., Mosconi, E. & De Angelis, F. Dynamical Origin of the Rashba Effect in Organohalide Lead Perovskites: A Key to Suppressed Carrier Recombination in Perovskite Solar Cells? *The Journal of Physical Chemistry Letters* **7,** 1638–1645 (May 2016).

205. Epstein, R. J., Fuchs, D. T., Schoenfeld, W. V., Petroff, P. M. & Awschalom, D. D. Hanle effect measurements of spin lifetimes in InAs self-assembled quantum dots. *Applied Physics Letters* **78,** 733–735 (Feb. 2001).

206. Maksimov, O., Zhou, X., Tamargo, M. & Samarth, N. Hanle effect measurements of spin relaxation in self-assembled CdSe quantum dots. *Physica E: Low-dimensional Systems and Nanostructures* **32,** 399–402 (May 2006).

207. Wu, X., Trinh, M. T., Niesner, D., Zhu, H., Norman, Z., Owen, J. S., Yaffe, O., Kudisch, B. J. & Zhu, X.-Y. Trap States in Lead Iodide Perovskites. *Journal of the American Chemical Society* **137,** 2089–2096 (Feb. 2015).

208. Dar, M. I., Jacopin, G., Meloni, S., Mattoni, A., Arora, N., Boziki, A., Zakeeruddin, S. M., Rothlisberger, U. & Grätzel, M. Origin of unusual bandgap shift and dual emission in organic-inorganic lead halide perovskites. *Science Advances* **2,** e1601156 (Oct. 2016).

209. Sarang, S., Bonabi Naghadeh, S., Luo, B., Kumar, P., Betady, E., Tung, V., Scheibner, M., Zhang, J. Z. & Ghosh, S. Stabilization of the Cubic Crystalline Phase in Organometal Halide Perovskite Quantum Dots via Surface Energy Manipulation. *The Journal of Physical Chemistry Letters* **8,** 5378–5384 (Nov. 2017).

210. Onsager, L. Crystal Statistics. I. A Two-Dimensional Model with an Order-Disorder Transition. *Physical Review* **65,** 117–149 (Feb. 1944).

211. Gurung, T., Mackowski, S., Jackson, H. E., Smith, L. M., Heiss, W., Kossut, J. & Karczewski, G. Optical studies of zero-field magnetization of CdMnTe quantum dots: Influence of average size and composition of quantum dots. *Journal of Applied Physics* **96,** 7407–7413 (Dec. 2004).

212. Goryca, M., Kazimierczuk, T., Nawrocki, M., Golnik, A., Gaj, J. A., Kossacki, P., Wojnar, P. & Karczewski, G. Optical Manipulation of a Single Mn Spin in a CdTe-Based Quantum Dot. *Physical Review Letters* **103,** 087401 (Aug. 2009).

213. Balanta, M. A. G., Brasil, M. J. S. P., Iikawa, F., Mendes, U. C., Brum, J. A., Danilov, Y. A., Dorokhin, M. V., Vikhrova, O. V. & Zvonkov, B. N. Optically controlled spin-polarization memory effect on Mn delta-doped heterostructures. *Scientific Reports* **6,** 24537 (Apr. 2016).

214. Viswanatha, R., Pietryga, J. M., Klimov, V. I. & Crooker, S. A. Spin-Polarized $Mn^{2+}$ Emission from Mn-Doped Colloidal Nanocrystals. *Physical Review Letters* **107,** 067402 (Aug. 2011).

215. Chernenko, A., Dorozhkin, P., Kulakovskii, V., Brichkin, A., Ivanov, S. & Toropov, A. Auger recombination of excitons in semimagnetic quantum dot structure in a magnetic field. *Physical Review B* **72,** 045302 (July 2005).

216. Chernenko, A. V., Brichkin, A. S., Sobolev, N. A. & Carmo, M. C. Mechanisms of manganese-assisted non-radiative recombination in Cd(Mn)Se/Zn(Mn)Se quantum dots. *Journal of Physics: Condensed Matter* **22,** 355306 (Sept. 2010).

217. Nawrocki, M., Rubo, Y. G., Lascaray, J. P. & Coquillat, D. Suppression of the Auger recombination due to spin polarization of excess carriers and $Mn^{2+}$ ions in the semimagnetic semiconductor $Cd_{0.95}Mn_{0.05}S$. *Physical Review B* **52,** R2241–R2244 (July 1995).

218. Léger, Y., Besombes, L., Maingault, L. & Mariette, H. Valence-band mixing in neutral, charged, and Mn-doped self-assembled quantum dots. *Physical Review B* **76,** 045331 (July 2007).

219. Le Gall, C., Besombes, L., Boukari, H., Kolodka, R., Cibert, J. & Mariette, H. Optical Spin Orientation of a Single Manganese Atom in a Semiconductor Quantum Dot Using Quasiresonant Photoexcitation. *Physical Review Letters* **102,** 127402 (Mar. 2009).

220. Baryshnikov, K. A., Langer, L., Akimov, I. A., Korenev, V. L., Kusrayev, Y. G., Averkiev, N. S., Yakovlev, D. R. & Bayer, M. Resonant optical alignment and orientation of $Mn^{2+}$ spins in CdMnTe crystals. *Physical Review B* **92,** 205202 (Nov. 2015).